Development of sensors for individual barium ion identification in the context of the NEXT experiment

PhD Thesis
Pablo Herrero Gómez

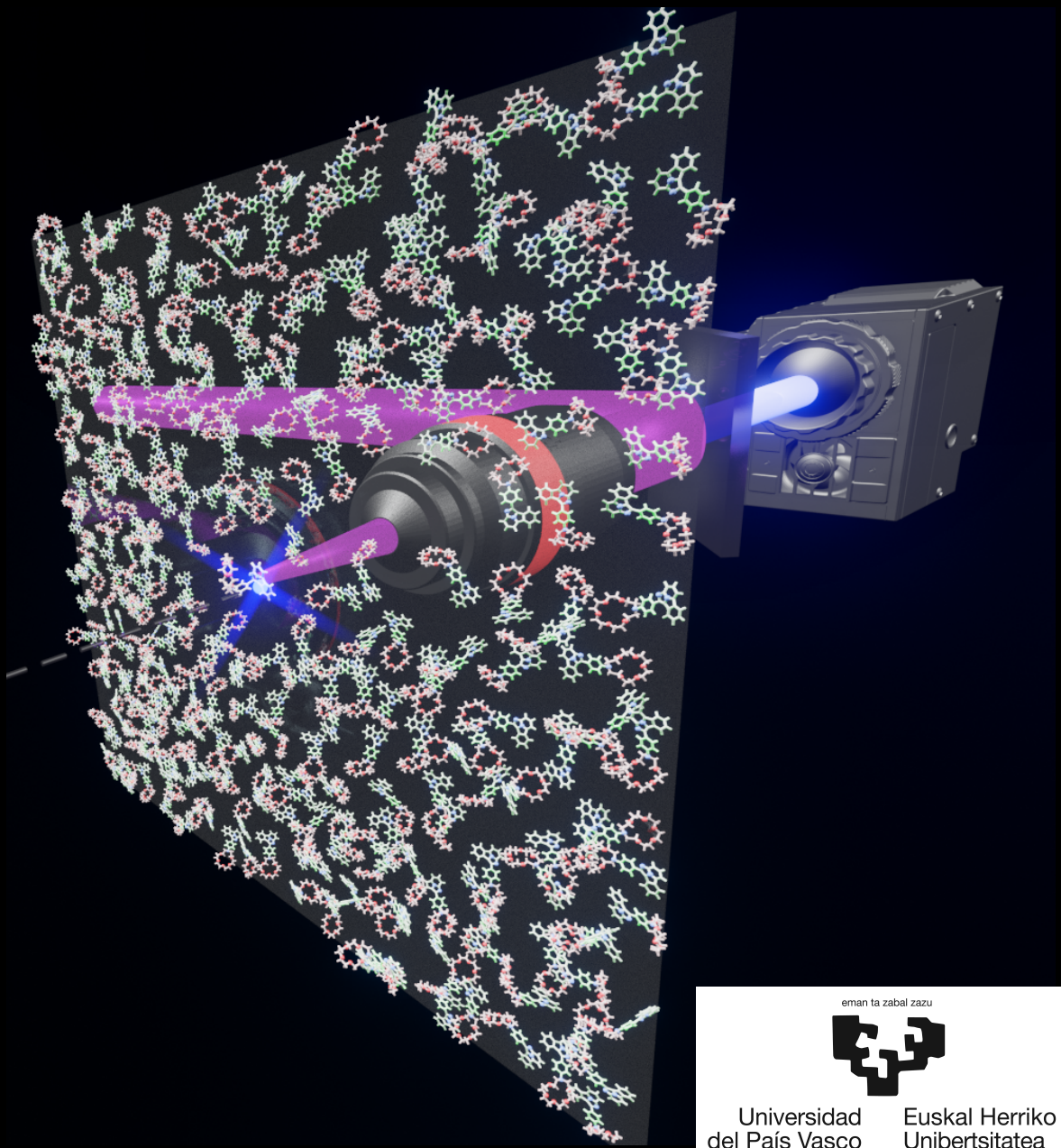

eman ta zabal zazu
Universidad del País Vasco
Euskal Herriko Unibertsitatea

eman ta zabal zazu

Universidad del País Vasco
Euskal Herriko Unibertsitatea

Development of sensors for individual barium ion identification in the context of the NEXT experiment

Pablo Herrero Gómez

Supervised by:
Dr. Celia Rogero and **Dr. Francesc Monrabal**

June 2023

(cc)2023 PABLO HERRERO GOMEZ (cc by 4.0)

Agradecimientos

Quiero agradecerles a mis codirectores Celia y Francesc todo el apoyo y los consejos que han hecho posible esta tesis. A Celia por acogerme en Donosti desde el primer día y ayudarme a formar parte de esta hermosa comunidad. Por la constante guía durante estos años y por su cercanía como persona. Por enseñarme a empezar los correos diplomáticamente con "tengo unas preguntillas". También por tantas comidas y cenas en la sociedad y por los viajes a Canfranc y a Basovizza, por haber compartido ella una deliciosa Ljubljanska. Por muchos cafés, por muchas charlas ¡y por muchas más por venir!

A Francesc por toda la ayuda con el microscopio, los shifts de NEW, por revisar muchos resúmenes, charlas y textos y por su infinita paciencia. Por acercarme a la colaboración, por aquella visita a la Universidad de Chicago y la cerveza en la torre John Hancock. Por muchas cenas discutiendo órdenes de magnitud al vuelo. Ya puestos, le agradezco mi primer contacto no sólo con NEXT sino con la física de investigación antes incluso de entrar en la universidad. Esos tres días me ayudaron a decidir mi carrera.

A JJ tanto por los incansables ánimos como los toques de atención. Por su confianza al encargarme responsabilidades, por su pasión y su curiosidad mucho más allá de la ciencia. Por quedarse con nosotros en el laboratorio remoto hasta tarde unos días y por echarme de allí el día que tocaba hacer surf o entrenar de Jiu Jitsu. Por ponerme a prueba pero siempre con optimismo.

A todas las personas que me han instruido y formado durante estos años. A todos los colaboradores y colaboradoras de BOLD, por su duro trabajo y por su cercanía. Gracias por hacer de Donosti el lugar donde me he sentido más apreciado. A Max, Carmen y Marina por ayudarme a aprender, por cientos de miles de transferencias y por disculpar el cementerio de muestras de cobre que hay en la cámara. A Samuel, David y Jed por recoger el testigo y por muchas risas en el laboratorio. A Martina, Dimas y su equipo Apolo: Alejandro, Patrick, Tao, James y Paula. Me ayudaron a dar mis primeros pasos en ciencia de superficies desde el día en que invadí una esquina de vuestro laboratorio con mi ALI hasta que sacamos las fotos que más he enseñado en charlas. A Patrick por su humor, su generosidad, su hospitalidad y su cocina. A mi maño Alejandro quiero agradecerle mucho, ya que ha sido el mejor

compañero de viaje dentro y fuera del laboratorio. Es una fuente de ideas (complejas pero sabe explicarlas a cualquier persona) y toda una inspiración como persona.

A los esbirros del neutrino: Iván y Zoraida. Han sido muchas aventuras echando bario a todo lo que nos encontrábamos a ver si algo cambiaba de color. Por su ayuda continua, por sus traducciones de "orgánico" a castellano y hacerme entender lo que me parecía ciencia de la magia con intuición. Por muchas risas y por su amabilidad. A Fernando Cossío por compartir su extensa experiencia y por la conversación en su coche a la vuelta del meeting de RITA en Canfranc. A los esclavos de los esbirros: Borja, Fernando II, Juan y todos los demás químicos (hay tantos como generaciones de FBIs). Por muchas cervezas, cafés y alguna sidrería. A Borja, la B de FBI, el químico de moda, que lo mismo de cocina una esferificación, que te fabrica su propia cerveza, que se saca un selfie profesional con todo este tinglado. No sólo hemos compartido viaje: gracias a él el barco se mantuvo siempre a flote.

A mis compañeros de óptica. A Gabriel, Miguel, Martín e Iker por tenderme una mano, porque sin ellos los primeros días en ese laboratorio a oscuras hubiera sido como ciego sin bastón ni perro. Para construir el microscopio nos faltaba más de un tornillo, tanto literal como figuradamente. A Jon por hacerme recordar lo bonita que es la física teórica. A todos los que vinieron después por vuestra amabilidad, por el fantástico ambiente y por los desayunos: Miriam, Rubén el bueno, Rubén el malo, que el apodo no engañe a nadie, tengo que agradecerle mucho en varios frentes: desde la ayuda con el ALI, el viaje a ALBA, la ayuda con el diseño del microscopio... Los sorbetes en la sociedad, el libro de Jerusalén y muchas, muchas risas. A Sergio lo mismo, nos quedamos hasta tarde en el laboratorio (mil gracias a Marc también) y nos desesperamos en alguna ocasión, pero gracias a su carácter siempre mantuvimos una sonrisa (y la cordura). A Alexey y Mikel, por continuar donde lo dejamos, por ser the best human being y por todo su entusiasmo.

A todos los estudiantes de prácticas, grado, máster: Afia, Borja, Leire, Lucie, Lander, Mikel, Pablo, Ade y Alfonso. Por acompañarme, ayudarme y enseñarme en las distintas etapas del camino. Por contagiarme vuestra motivación.

A los NEXTers: Alberto por ser el mejor compañero de habitación

y de bigote. Por hacerme sentir como en casa en Fermilab. Helena por muchas charlas, por la compañía durante la pandemia y por hablar hasta con las farolas. Paola por su caluroso apoyo, por su contagiosa energía, por la inspiración con los idiomas y con el ajedrez. Andrew por enseñarme lo que es nadar de verdad. Josh y José María por ser unos pianistas de la terminal, por mi primer shift y por compartir conmigo hasta el template de esta tesis. A Javi y Carmen por estar ahí, en el despacho y en Marboré. A Bea y Ander por salvarme de muchos, muchos marrones y por ser clementes cuando no pudieron hacerlo. A Michel y Gonzalo (y Alberto y Josh de nuevo) por la carrera hasta Candanchú y Somport. A Michel, Pau, Justo y Neus y todos los demás (me acuerdo de todos, nadie queda como et al.) por muchas palabras amables y por hacer que Valencia siga siendo mi segunda casa.

En Donosti he tenido muchas casas, pero sin duda la que he podido llamar mi casa ha sido la que he compartido con Raúl y Toni. Costó ponernos de acuerdo, pero este ha sido mi año más feliz gracias a ellos. También han estado ahí en los momentos más duros, pero en perspectiva se hacen más llevaderos gracias a su compañía. Toni por seguir recordándome que el gimnasio también sigue abriendo a las 7:30, ¡por el fútbol!, por el viaje a Medievales y por enriquecer inmensamente todas nuestras discusiones. Raúl porque es un hermano más. Desde el día que nos tomamos algo en el Altxerri hemos congeniado y nos hemos apoyado en todo momento. Por muchas noches de peli y pizza (casera), por descubrirme Blender y Murakami, por la natación. Por el viaje a Burdeos y a Formigal. Te quiero mucho, Raúl.

A Sebastián Bergeret por abrirme las puertas de su casa y por descubrirme a Jim Jarmusch, a Emmanuel Carrère, the Melvins... Coincidimos poco en tiempo pero mucho en intereses. En cada cena aprendía un par de cosas nuevas.

También puedo decir que viví en el Kampamento Krusty, aunque fuera por dos semanas. Gracias a Matteo (Dr. Sanvo) que me acogieron ese verano. Ese piso fue durante mucho tiempo nuestra base de operaciones (y en pandemia, nuestro calabozo). Agradezco a todos los que han pasado por allí por formar parte de nuestra comunidad, y lo que podía haber sido una asociación de estudiantes: Alejandro, Andrea, Minh, Valerio y hay que contar a Carmelo, claro. Matteo por su filosofía, sus poemas, su magia, sus cazzate… y su AFM. To Minh because it's not Mihn it's Minh, because bromance, AoT, because he is

the best cook of Paella and random things. Andrea porque sin él me habría perdido muchas noches en lo viejo o en el Doka, por el trash italiano, por las lasañas y las pizzas de pepperoni. A Davide por ser el mejor locutor de publicidad en el mundo hispano-hablante además de una capra montesa. A Claridad, porque el propio nombre lo indica, por ser un ejemplo y por a veces entenderme sin que le explique nada (también la llaman Clarividencia). A Carmelo por ser un buen amigoo, aiutoo, por su barco velero y por los zumitos. A Jose por el baile con la Roomba y por no perderse una illo, ya sea en Korea o en Teruel. A Luis y Dani el industrioso por el 5G y la caja de pandora dada la vuelta.

No me olvido de otros compañeros de piso: José Carlos y Daniel. Por mantenerme en contacto con la realidad, por el viaje a Biarritz. A Sara y Daniel, por todas la botana con salsa valentina que me han comprado en el Día. A Jacob por muchas tartas y cafés, por bajar el ritmo con la bicicleta y por contagiarme su fascinación por esta ciudad. A Lizzie por ser una fuente incombustible de buen rollo y por subir Igeldo de resaca. Me dejo a muchos, pero quiero mencionar a ESN-Donosti (y Bilbao, pero menos) por unos messes geniales y por una PR o NR, ¿LN?... hay demasiadas siglas; y a Gracie Barra Antiguo, por mi salud mental y por no cerrar nunca la puerta.

Ya me quedan menos. A los que están lejos pero siguen ahí: Pau, Héctor, Víctor y Alex Fontana. Porque me dan perspectiva y por esforzarse por mantener la amistad estos años. A mis amigos de Teruel, por todos los ánimos y la alegría que me dan desde la época grunge.

A mi familia: Mar, Irene, Marina, Héctor, Diego, Alex, Sofía, Blanquita y Nico. Isabel, Florián, Juanjo, Pilar, Lola, Cuña, Aure, Eva, Carlos, Toni y Vicky. Por darme energía sólo con veros a todos juntos. A Jesús y Jorge, porque los dos podríais defender esta tesis mejor que yo. Incluso le daríais la perspectiva social, humana y filosófica que la ciencia necesita. Y porque en el fondo esto siguen siendo ninoninos. A papá y mamá, porque sois mis pilares. Porque gracias a vosotros (y a la furgo) mi casa está en cualquier lugar.

A mis abuelos. A Lucía y Ángel por el estoicismo, por el humor y por las raíces. A Cari por apretarme la mano y leerme la mente. A Aurelio por haber empezado todo.

Resumen

Esta tesis recoge los resultados obtenidos durante los primeros pasos en el desarrollo de un quemo-sensor de bario dicatión para el experimento NEXT. Los quemo-sensores son dispositivos en miniatura ampliamente utilizados para obtener información sobre la presencia de compuestos específicos o iones en entornos complejos. Su funcionamiento se basa en convertir propiedades químicas del analito en una señal detectable, como una señal eléctrica u óptica. Las señales de fluorescencia en particular presentan propiedades muy relevantes para detectar iones específicos mediante moléculas inmobilizadas sobre una superficie. El enlace que se produce entre estas moléculas y el ión produce cambios en la intensidad, la longitud de onda o la vida media de la emisión fluorescente. Al detectar estos cambios se puede cuantificar la concentración del ión en la muestra. Este tipo de dispositivos tienen distintas ventajas como una alta sensibilidad y facilidad de uso. Además, se pueden diseñar para ser muy selectivas al ión de interés y para funcionar en entornos particulares.

Recientemente se ha explorado el uso de quemo-sensores fluorescentes como herramienta potencialmente única en el campo de la física de neutrinos. Si el neutrino es su propia antipartícula, entonces puede existir la reacción de desintegración *doble beta sin neutrinos* ($0\nu\beta\beta$). Esta insólita reacción $(Z, A) \rightarrow (Z + 2, A) + 2\ e^-$ sólo se puede dar si los neutrinos son partículas de Majorana, es decir, idénticas a su antipartícula. Si se detectase la reacción $0\nu\beta\beta$, se probaría que los neutrinos son partículas de Majorana. Este descubrimiento ayudaría a extender el modelo estándar de partículas, ya que esta teoría todavía no incluye la naturaleza ni la masa del neutrino. Además, establecer si el neutrino es su propia antipartícula ayudaría a responder al problema de la asimetría bariónica en cosmología: en el Big-Bang se debió crear tanta materia como antimateria, sin embargo, sólo observamos materia hoy en día. Si el neutrino es su propia antipartícula, podría ser el responsable de romper esta simetría.

El experimento NEXT busca detectar la reacción $0\nu\beta\beta$ del isótopo ^{136}Xe. En esta desintegración se producen dos electrones y un dicatión $^{136}Ba^{2+}$. Si el ión Ba^{2+} se detectase en coincidencia con los electrones, el experimento NEXT funcionaría sin background. Para identificar el ión Ba^{2+} se ha propuesto utilizar quemo-sensores fluorescentes. El uso

de esta técnica en el campo de física de partículas es completamente novedoso y requiere adaptar estos sensores al entorno extremadamente seco de una cámara de xenon gaseoso a alta presión. Este es el objetivo final del trabajo que hemos llevado a cabo en esta tesis.

El trabajo de esta tesis ha tenido lugar en el contexto de la colaboración NEXT y con el apoyo del proyecto Synergy "BOLD". El principal objetivo de esta tesis es la demostración y el estudio a nivel atómico de la interacción entre moléculas fluorescentes e iones de Ba. Este trabajo es esencial como primer paso en la fabricación de un sensor de bario con la mayor sensibilidad posible.

El sensor debe ser extremadamente sensible ya que la reacción $0\nu\beta\beta$ es sumamente elusiva y sólo producirá unos pocos iones Ba^{2+} al año. En el capítulo 2 explico esta reacción y las consecuencias que tendría su descubrimiento. También describo el experimento NEXT y cómo se planea implementar el sensor de bario. A continuación, en el capítulo 3 describo tres familias de moléculas fluorescentes que podrían utilizarse para fabricar este sensor. Las moléculas que principalmente uso en esta tesis son los Indicadores Fluorescentes Bicolores (FBI por sus siglas en inglés). La detección de Ba^{2+} con estas moléculas se basa en el cambio de color que se produce en en enlace con el ión (quelación).

La fabricación del sensor requiere inmobilizar las moléculas en una superficie que preserve la sensibilidad de la señal fluorescente. Además, el sensor se instalará en una cámara de gas xenon, por tanto no puede contener disolventes. Este enfoque requiere el uso de técnicas de deposición molecular y caracterización en superficies con precisión atómica. En el apéndice A1 resumo estas técnicas de crecimiento (sublimación molecular) y caracterización (XPS, STM/STS).

En el capítulo 5 presento los resultados obtenidos con las técnicas de ciencia de superficies. Los resultados demuestran que las moléculas FBI capturan Ba^{2+} en condiciones de ultra alto vacío, repicando las condiciones del experimento real. En el capítulo 6 muestro los correspondientes resultados con dos nuevas generaciones de moléculas FBI, demostrando que estas dos moléculas también atrapan bario y otros iones.

El capítulo 7 presento el diseño inicial y la construcción de un microscopio de fluorescencia como el que se utilizará en el experimento NEXT-BOLD. También muestro resultados preliminares obtenidos con

el microscopio para caracterizar las propiedades fotoquímicas de las moléculas FBI. Finalmente, en el capítulo 8 resumo las principales conclusiones obtenidas en esta investigación y los siguientes pasos que se tomarán en el experimento BOLD.

Contents

List of Figures

List of Tables

1 Introduction

Chemical sensors are miniaturized devices widely used to get instant information on the presence of specific compounds or ions even in complex environments. They work by converting the chemical properties of a target analyte into a measurable signal, such as an electrical or optical signal. Chemical sensors are commonly used in various fields, including environmental monitoring, food quality control, medical diagnostics, and industrial process control, among others. Among them, optical chemical sensors employ optical transduction techniques to yield analyte information [1]. Due to the outstanding characteristics of both fluorescence and phosphorescence signals, they are widely applied to the construction of chemical sensors where susceptible fluorescence molecules are immobilized on a surface [2].

Fluorescence chemosensors work by exploiting the changes in fluorescence properties of a fluorescent molecule or probe upon binding to a specific target ion or molecule. The binding event can lead to changes in the intensity, wavelength, or lifetime of the fluorescence emission, which can be measured and used to quantify the concentration of the target ion or molecule in a sample. They have several advantages for ion detection compared to traditional analytical techniques, such as their high sensitivity, selectivity, and ease of use. Additionally, they can be designed to be highly specific for a particular ion or molecule, and can be tailored to work in specific environments or under specific conditions. They have been used for the detection metal ions, anions, and cations, in both aqueous and non-aqueous environments. They have applications in a variety of fields, including environmental monitoring, biomedical research, and industrial process control.

Recently fluorescence chemosensors are under exploration as potentially unique tools in the field of neutrino particle physics. If neu-

trinos are their own antiparticles, the otherwise-forbidden nuclear reaction known as neutrinoless double beta decay can occur [3]. The rare neutrinoless double beta ($0\nu\beta\beta$) decay, $(Z, A) \rightarrow (Z+2, A) + 2\,e^{-}$, can occur if and only if neutrinos are Majorana particles [4], e.g., identical to their antiparticles. An unambiguous observation of such decay would have deep implications in particle physics and cosmology[5–9]. It has been proposed that identifying ("tagging") the Ba^{2+} dication produced in the double beta decay of ^{136}Xe isotope in a high pressure gas experiment, could lead to a virtually background free experiment [10]. Detection based on chemical sensors have been proposed in a high pressure xenon TPC[10–14]. These sensors would deliver real time and online information to indicate the presence of specific compounds or ions even in complex samples.

However, despite the fact that complex experimental programs have been conducted over more than fifty years, the extremely rare reaction is still making its detection almost impossible. Hence, the application of such chemosensors to the field of particle physics is totally novel and requires experimental demonstration of their suitability in the ultra-dry environment of a xenon gas chamber. This is the final aim of the work we have started in this thesis.

In the context of the NEXT Experimental Collaboration and under the umbrella of a Synergy Project, BOLD, this thesis has focused on the demonstration at atomic level of the interaction of the molecules with the Ba^{2+} ions. This work is essential as a first step toward the final fabrication of the Ba sensor with the highest possible sensitivity.

The requirement of extremely high sensitivity is mandatory due to the rare nature of the $0\nu\beta\beta$ decay. Chapter 2 I will explain this decay and the implications that the demonstration would have in our understanding of the universe. Next, in Chapter 3 I will introduce the development of the Ba sensor in the context of the NEXT Experimental Collaboration. The initial works proposed commercial chemosensors for the trapping of Ba ions [15, 16]. Since then, the research has evolved to the design and synthesis of new functional and specific molecules for the Ba trapping [13, 14], particularly the fluorescent bicolor indicators (FBI) molecular family. A brief introduction to the properties of these molecules and an initial proof-of-concept experiment are discussed in 3.

To develop a final chemosensor for neutrino detection, it is nec-

essary to immobilize the molecules on a surface while maintaining their ion sensitivity. This all must be done in the absence of any solvent, because the detector will be installed in a high-pressure gas xenon chamber. An atomically precise sensor fabrication is the best approach for further increasing the sensitivity of chemical sensors. This approach involves using atomic-scale precision growth techniques, such as molecular sublimation, to fabricate sensors with well-defined and uniform surface properties. This can lead to enhanced analyte-sensor interactions and improved signal-to-noise ratios, resulting in higher sensitivity and selectivity. Moreover, in order to prove that the chemosensor is behaving as it should at atomic level, a combination of highly surface sensitive techniques, such as X-ray photoemission spectroscopy (XPS) and scanning tunneling microscopy and spectroscopy (STM/STS), is required. A brief summary of the experimental techniques used for the research is included in A1.

Chapter 5 contains the results of the surface science, which prove that FBIs can capture barium under ultra-high vacuum conditions replicating the dry conditions of a real experiment. In chapter 6 two new generations of FBI molecules are introduced. The corresponding surface science experiments prove that these new generations can also capture barium and other ions. In chapter 7 I introduce the initial design and assembly of a fluorescence microscope which will be implemented in the final NEXT-BOLD detector. In this chapter fluorescence microscopy experiments and some preliminary results are discussed, with the aim of characterizing the photochemical properties of FBIs. Finally, in chapter 8 I will list the next steps that will be carried out in the context of the BOLD experiment and the main conclusions from my research.

2 NEXT and the Nature of Massive Neutrinos

2.1 Majorana Neutrinos and the Missing Antimatter

Cosmological inflation models predict equal amounts of matter and antimatter at the beginning of the universe, since any possible initial asymmetry would be diluted by inflation [17]. However, we now observe no traces of cosmological antimatter; the observable universe today and all its structures –stars, galaxies, clusters– are made of matter. This is the so-called baryon asymmetry and its origin is yet unknown. One can visualise the problem by imagining all the matter in the universe placed on one plate of a cosmic balance scale and all antimatter placed on the other plate. All creation and annihilation operators preserve matter-antimatter symmetry, since no particle can be created without creating its antiparticle. The same is true for annihilation processes. However, the fact that the universe contains matter and not antimatter means that some mechanism favoured ever so slightly the side of the balance that we call "matter". This tenuous imbalance could have enabled other reactions that prevented some portion of matter from eventually being annihilated with its antimatter counterparts. The initial asymmetry may have been tiny, as well as the surviving portion of matter, but in the cosmic scale it would mean the whole universe as we know it today.

Baryon asymmetry is quantified from observations of the Cosmic Microwave Background (CMB) and Big Bang Nucleosynthesis (BBN) [18]. Had the initial universe been perfectly symmetric, the baryons and antibaryons would have annihilated into photons, leaving the current universe almost depleted of matter. The baryon asymmetry implies that only $\sim 10^{-9}$ early baryons survived and did not annihilate with their antimatter pairs into photons. Therefore, the asymmetry

between baryons and antibaryons must have developed in the early universe through processes known as *baryogenesis*.

Leptogenesis is a family of baryogenesis theories which attribute the initial asymmetry between matter and antimatter to neutrinos. The nature of neutrinos is an open question in particle physics (see section 1.2), and they are the only fundamental particle that could break the matter-antimatter symmetry. For this to be true, neutrinos would have to be *their own antiparticles*, i.e. Majorana particles. If neutrinos are equivalently matter and antimatter, a small fluctuation toward the side of matter could have been the cause of the tilt in the cosmic balance. However, both the neutrino's nature and its mass are still under investigation.

The neutrino was originally considered a massless particle in the Standard Model (SM). However, different experiments have demonstrated that neutrinos oscillate between flavours (ν_e, ν_μ and ν_τ) [19–24], which implies that they must be massive. Therefore, the SM must be extended to include the mass of neutrinos. Experimentally, the neutrino mass can be directly measured using the β-decay, inverse β-decay [25–27] or double beta decays of some isotopes. Important information on the neutrino mass can also come from cosmological observations, since neutrinos must have had an impact on the rate of expansion of the universe and the growth of perturbations [28]. A combination of Cosmic Microwave Background (CMB) data and Baryon Acoustic Oscillations (BAO) measurements sets a limit of [29] $m_{\text{light}} \approx \sum m_\nu/3 \leq 0.07$ eV at 95% confidence level (CL) in the quasi-degenerate regime of neutrino masses. This means that there is at least 6 orders of magnitude of difference between the neutrino masses and the charged lepton and quark masses. Such difference suggests that there must be a new fundamental mass scale in particle physics beyond the Standard Model.

2.2 Dirac vs. Majorana Neutrinos

An even more interesting question is how do neutrinos get their mass. The SM considers only neutrinos with left-handed chirality ν_L, but if neutrinos are massive right-handed neutrinos ν_R can also exist. However, they are not observed experimentally. Then the question is:

where are they, and why do they exist? To answer these questions, two kinds of neutrinos are considered: Dirac and Majorana neutrinos. If neutrinos are Dirac particles, they can be distinguished from their antineutrino counterparts. The mass term for Dirac neutrinos in the SM Lagrangian is directly analogous to the mass term for quarks and charged leptons: the neutrino fields couple to the Higgs field via Yukawa coupling. However, the resulting neutrino Yukawa coupling must be 6 orders of magnitude smaller than the electron Yukawa coupling, which is seen as unsatisfactory in the community [30, 31].

If they turn out to be Majorana particles, it would pave the way to answer two more questions: the baryon asymmetry (see section 2.1) and the difference between the mass scale of neutrinos and that of the rest of the fundamental particles in the SM.

The second way to add the neutrino mass to SM Lagrangian was carried out by Ettore Majorana. He proposed the condition [3]:

$$\nu^C = \nu, \tag{2.1}$$

where ν^C is the charge-conjugate of ν. This condition implies that both neutrino and antineutrino states are described with a single field. In other words, the Majorana neutrino is identical to the antineutrino.

If neutrinos are Majorana particles, the difference of at least 6 orders of magnitude between the neutrino masses and the charged fermions can be explained by the so-called *see-saw mechanism* [32–34]. This theory in addition predicts the existence of two neutrino states with inversely proportional masses. The relationship between a very light and a very heavy neutrino inspires the name *"see-saw"*. The only direct way to prove that neutrinos are Majorana particles is by detecting a neutrinoless double beta decay ($0\nu\beta\beta$). This extremely elusive decay can only occur if neutrinos act as their own antiparticle.

2.3 Double Beta Decays

The double beta ($\beta\beta$) decay is a second-order weak process in which a nucleus with Z protons decays into another with Z+2 protons and the same mass number A (i.e. its isobar). The Feynman diagram of the $2\nu\beta\beta$ decay modes in its simplest form is shown in Fig. 2.1b where the two simultaneous β-decays are plotted. Maria Goeppert-Mayer

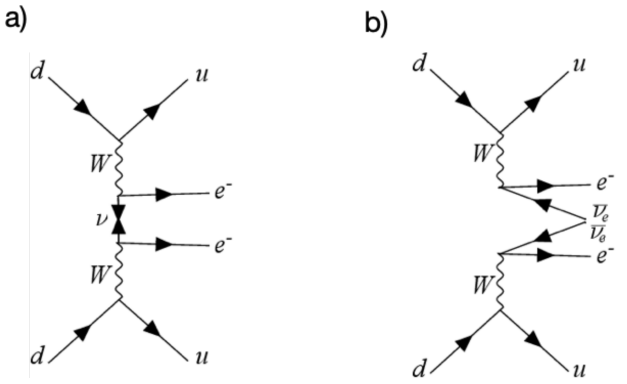

Figure 2.1. Feynman diagrams for the (a) $0\nu\beta\beta$ and (b) $2\nu\beta\beta$ decay modes.

proposed the ordinary $\beta\beta$ mode in 1935 [35]. This mode consists on two simultaneous beta decays ($2\nu\beta\beta$):

$$(Z, A) \rightarrow (Z + 2, A) + 2e^- + 2\overline{\nu}_e \tag{2.2}$$

Geochemical evidence of this process was discovered in 1950 using the isotope ^{130}Te [36]. A direct observation of the process occurred in 1987, when a time projection chamber showed the $2\nu\beta\beta$ decay of ^{82}Se [37]. This discovery led the way for observations in several other nuclides, such as ^{136}Xe, with half-lives in the order of 10^{18} - 10^{21} years [38–40].

Since $2\nu\beta\beta$ lifetimes are so long, the single β-decays of most nuclides become an intense source of background for its detection. Therefore, only when single β-decay is forbidden or highly suppressed does $2\nu\beta\beta$ detection become feasible. There are 35 isotopes in nature which fulfil this condition, being one of them the ^{136}Xe, isotope used in the NEXT experiment.

While the $2\nu\beta\beta$ decay is a very rare event, it is allowed in the Standard Model. However, the neutrinoless mode $0\nu\beta\beta$ (Feynman diagram shown in Fig. 2.1a),

$$(Z, A) \rightarrow (Z + 2, A) + 2e^-, \tag{2.3}$$

would violate total lepton number conservation, and is therefore forbidden in the Standard Model. Wendell H. Furry proposed this mode in 1939 [41] as a method to test the Majorana nature of neutrinos [3].

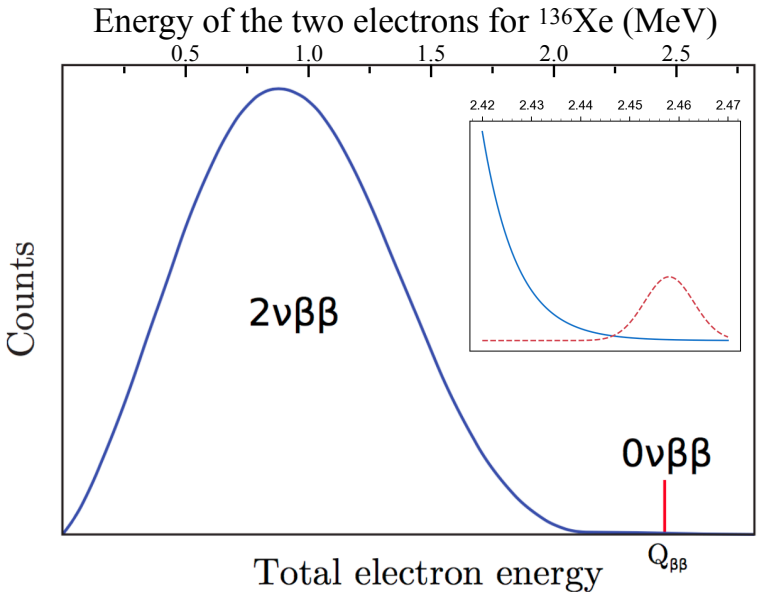

Figure 2.2. Conceptual spectra for the sum of the kinetic energies of the two emitted electrons for the $2\nu\beta\beta$ (blue) and the $0\nu\beta\beta$ (red) modes. The amplitudes are arbitrary. The energy position of the $0\nu\beta\beta$ ($Q_{\beta\beta}$) is perfectly defined by theory and is characteristic of each isotope. On the top scale the energy for the case of ^{136}Xeis displayed. Inset: Zoom on region of interest around $Q_{\beta\beta}$ showing the overlap of both populations due to finite detector energy resolution.

Therefore, it is a critical reaction to establish the nature of neutrinos and the mechanism by which they get their mass.

In both decay modes the nuclear recoil is negligible, so the emitted leptons carry almost all the available energy. Therefore, in the two-neutrino mode ($2\nu\beta\beta$), the total energy is distributed between four particles, so if we sum the kinetic energy of the two emitted electrons, we obtain a continuous spectrum. On the other hand, in the neutrinoless mode ($0\nu\beta\beta$) all the energy goes to the two electrons, so the signal is monochromatic and located exactly at $Q_{\beta\beta}$, which is defined as the mass difference between the parent and daughter nuclides:

$$Q_{\beta\beta} \equiv M(A,Z) - M(A,Z+2) \tag{2.4}$$

A scheme of these two distributions is shown in figure 2.2. These

distributions show that $0\nu\beta\beta$ can be detected simply by *measuring the energy of the two electrons*. It is worth noting that the relative intensities between the $2\nu\beta\beta$ and $0\nu\beta\beta$ distributions in Fig. 2.2 are not necessarily at scale. Since the lifetime of $2\nu\beta\beta$ is around $10^{19} - 10^{21}$ years and that of $0\nu\beta\beta$ is at least over 10^{26} years (and expected to be around $10^{27} - 10^{28}$ years), the expected number of counts for the $2\nu\beta\beta$ mode in a particular experiment is severals orders of magnitude larger than that of the $0\nu\beta\beta$ mode. Furthermore, depending on the precise shape of the $2\nu\beta\beta$ mode distribution, its high energy tail overlaps more or less with that of the $0\nu\beta\beta$ mode. Therefore, an excellent energy resolution is crucial for any experiment attempting to detect $0\nu\beta\beta$ decays to distinguish it from the $2\nu\beta\beta$ mode.

The amplitude of a $0\nu\beta\beta$ decay (fig. 2.1a) would be proportional to the effective neutrino Majorana mass, $m_{\beta\beta} \equiv \left|\sum_{i=1}^{3} U_{ei}^2 \cdot m_i\right|$, where U_{ei}^2 are elements of the flavour mixing matrix and m_i are the three light neutrino masses. In practice, what this means is that the lifetime of the $0\nu\beta\beta$ decay is inversely proportional to $m_{\beta\beta}^2$ [42]:

$$\left(T_{1/2}^{0\nu}\right)^{-1} \propto \left(\frac{m_{\beta\beta}}{m_e}\right)^2 . \tag{2.5}$$

A measurement of the $0\nu\beta\beta$-rate would yield the value of the effective Majorana mass $m_{\beta\beta}$, which in turn would provide direct information on the absolute neutrino mass scale. On the other hand, if a given experiment does not observe the $0\nu\beta\beta$ process, they can place an upper bound on the effective Majorana mass $m_{\beta\beta}$. Currently, the most stringent bound on $m_{\beta\beta}$ was set by the KamLAND-Zen experiment as $m_{\beta\beta} < 65$ meV. The aim of next-generation, ton-scale experiments is to reach the range of $m_{\beta\beta} < 10$ meV. However, the value may be in the range of $m_{\beta\beta} \approx 1$ meV or even less. Notice that the smaller the effective neutrino mass, the fainter the $0\nu\beta\beta$ signal. Therefore, building ton-scale detectors may not be enough to ascertain the nature of neutrinos. If the effective neutrino mass is in the range of 1 meV, the experiments will need to run free of background to detect the $0\nu\beta\beta$ signal in a reasonable timescale (around 10 years of livetime).

The search for neutrinoless double beta decay is a very active field in particle physics, with constant upgrades and improvements. The goal of next generation experiments is to cover the inverted ordering.

Several international collaborations are trying to detect $0\nu\beta\beta$ decay, all of them using different approaches to exploit some properties of the target isotope. Some materials act as source and detector, like germanium, which contains the $\beta\beta$-emitting isotope ^{76}Ge. The GERDA and Majorana experiments have used germanium crystals as target material. Other experiments like SNO+ use liquid scintillators loaded with tellurium, containing a $\beta\beta$-source ^{130}Te. Tellurium oxide is also used as a crystal bolometer, as the case of CUORE. Lastly, xenon is widely used in $0\nu\beta\beta$ searches, for several reasons: as a gas it can be enriched in its $\beta\beta$-isotope ^{136}Xe; it can be diluted in liquid scintillators (KamLAND-Zen), or used directly as both source and detector by exploiting its scintillation properties; and it can be deployed in liquid (EXO) and gas phase (NEXT). Using liquid xenon allows to amass more material in a smaller volume, but the intrinsic energy resolution is lower than in gas phase. The NEXT detector provides the main context for this thesis, so it will be described in detail in the following section.

2.4 The NEXT experiment

The Neutrino Experiment with a Xenon TPC (NEXT) is an experiment dedicated to $0\nu\beta\beta$ decay searches and located at the Laboratorio Subterráneo de Canfranc (LSC), under the Spanish Pyrenees [43]. NEXT is an international collaboration led by Spanish and US groups. Currently, more than 100 people -from more than 20 institutions- are involved in the experiment.

The goal of the experiment is to search for neutrinoless double beta decay of ^{136}Xeusing a high pressure xenon gas TPC with the detector. Gaseous xenon offers some appealing advantages such as scalability, excellent energy resolution and topological signature for background discrimination. When excited by an incoming particle, noble gases emitting scintillation photons proportionally to the deposited energy, thereby enabling its measurement. Xenon is used in TPCs for $0\nu\beta\beta$ decay searches as the isotope 136 has a natural abundance of 9% and it can be enriched by centrifugation. Other advantages are the absence of other long-lived radioactive isotopes and its high $Q_{\beta\beta}$ (2458 keV), at which point most natural radioactive background is suppressed.

The two-neutrino mode of ^{136}Xe is relatively slow, with $T^{2\nu}_{1/2}(^{136}\text{Xe}) = 2.2 \times 10^{22}$ yr [22, 44, 45] , which relaxes the requirement for energy resolution. However, in gaseous phase, xenon can provide energy resolution better than 0.5% FWHM at the $Q_{\beta\beta}$ of ^{136}Xe[46], which is a crucial requirement for an experiment to distinguish the $0\nu\beta\beta$ mode from the $2\nu\beta\beta$ mode.

The working principle of the NEXT TPC is illustrated in figure 2.3. The gaseous xenon is contained in a cylindrical pressure vessel and its internal walls are covered with PTFE, which acts as a reflector to improve the light collection efficiency. The radiation traversing the vessel ionise the medium leaving free electrons and ions along its trajectory. This first ionisation signal is detected by the Photo Multiplier Tubes (PMTs) and sets the *start-of-event prompt*. A uniform electric field drifts the electrons toward the electroluminescence (EL) amplification region. There, the EL light is read by the tracking plane, composed of Silicon Photomultipliers (SiPMs) with 2D spatial segmentation. The SiPMs record the amplitude and transverse position of the ionisation electrons, while the longitudinal coordinate is calculated from the arrival time of the signals with respect to the *start-of-event* t_0. Therefore, the TPC provides a measurement of the energy deposition pattern ($\mathrm{d}E/\mathrm{d}x$) and a full three-dimensional reconstruction of the trajectory of a charged particle. The latter is known as *topological signal* and is used to distinguish signal from $\beta\beta$ decays (two-electron tracks) from background (single-electron tracks). Some examples of topological signal of single and double electron tracks can be seen in figure 2.4. A well-resolved topological signature has another use beyond background rejection: the barycentre of the double-electron track sets the X-Y position of the decay origin where the Ba^{2+} ion is expected to be found on the cathode. Forecasting these coordinates can simplify significantly the design of the Ba-tagging device.

The project has spanned for more than 10 years and is planned to continue for over 10 or 15 more. An overview of the NEXT program and its phases can be seen in Fig. 2.5. The first phase of the project (2009-2014) consisted in constructing, commissioning and operating two prototypes for R&D: NEXT-DBDM and NEXT-DEMO, with isotope masses around 1 kg. During the second phase, from October 2016 until July 2021, the collaboration operated NEXT-White (NEW) at LSC.

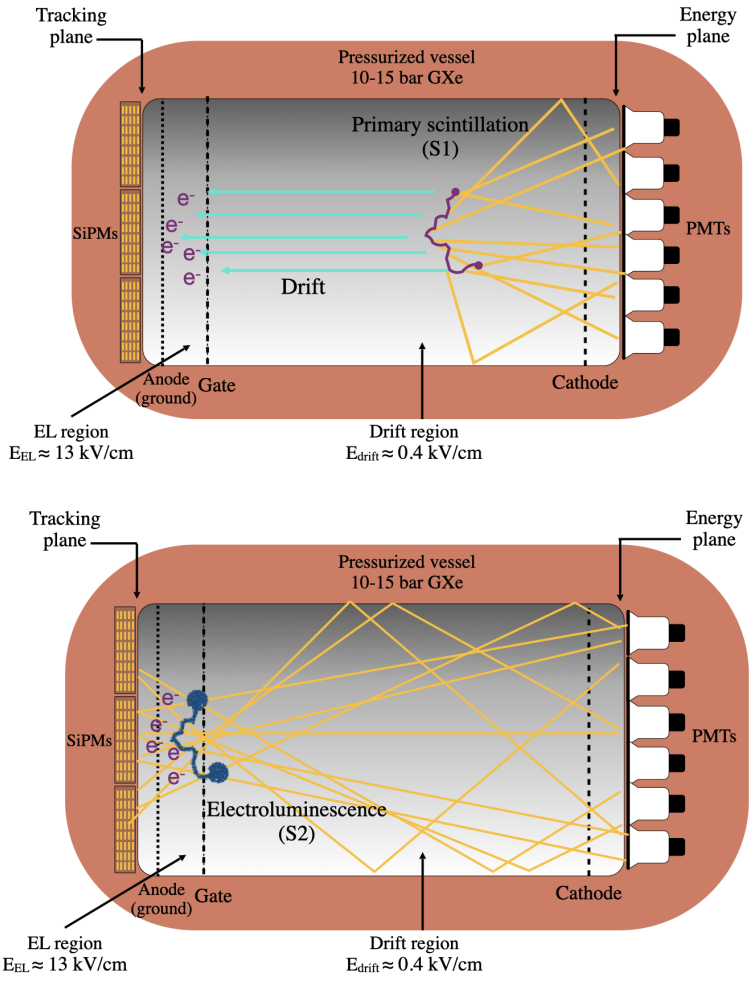

Figure 2.3. Working principle of the TPC in NEXT. (Top): The ionising radiation produces a first scintillation signal (S1), which is detected by the PMTs in the energy plane. This event sets the start-of-event t0 for the reconstruction of the position in longitudinal axis. Then the electric field drifts the ionised electrons toward the EL region. (Bottom): The secondary scintillation (S2) generated at the EL region is measured by the tracking plane of SiPMs placed behind the anode. This light is also detected by the PMTs placed behind the transparent cathode for precise energy measurement.

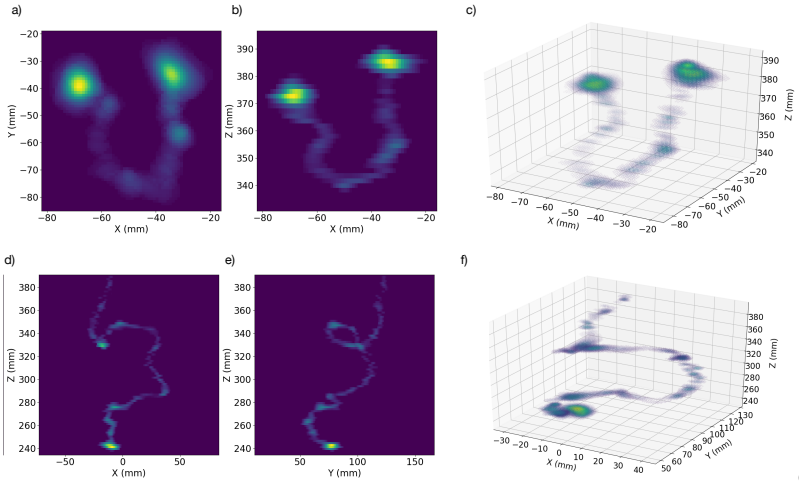

9

Figure 2.4. Topological signal in NEXT. (a-c) Examples of two-electron events in the X-Y (a) and X-Z (b), and in 3-D projections. (d-f) Examples of a single-electron track in the X-Z (e), Y-Z (e) and in 3-D projections.

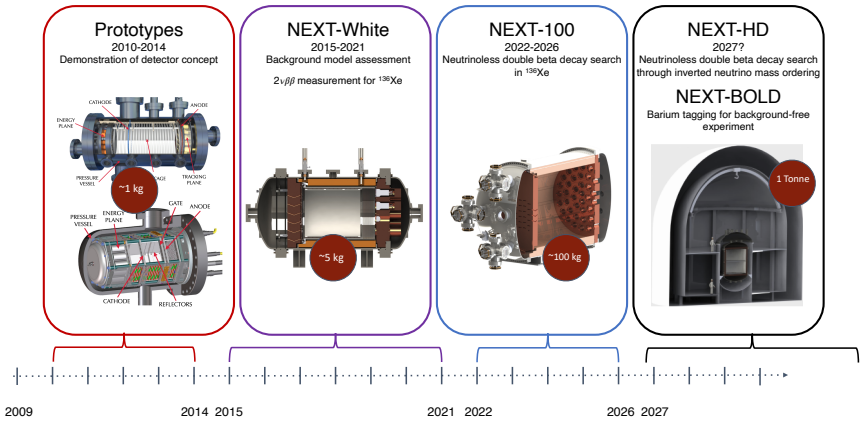

Figure 2.5. Summary of the NEXT program and its phases.

NEXT-White is a medium size detector containing 5 kg of xenon and its main physics goal is to measure the $2\nu\beta\beta$-decay half-life of ^{136}Xe. A $2\nu\beta\beta$ half-life of $T^{2\nu}_{1/2} = 2.34^{0.80}_{-0.46}(\text{stat})^{0.30}_{-0.17}(\text{sys}) \times 10^{21}$ yr was measured [47]. This result is consistent with the two previous measurements in Refs. [44] and [22]. This was achieved by comparing

two sets of data: one with the detector filled with xenon *enriched* in ^{136}Xe and the other *depleted* of ^{136}Xe. The resulting $2\nu\beta\beta$ energy spectrum is shown in figure 2.6. The ^{136}Xe-depleted data was also used to understand the different sources of background. The background model included 4 isotopes (^{60}Co, ^{40}K, ^{214}Bi and ^{208}Tl), which come from natural radioactivity since traces of thorium and uranium are present in most detector components. The only way to minimize this backgrounds is to carefully select radioupure materials [48–50]. Knowing the (trace) amount and types of potential contaminants in the volume is crucial in the design of a Ba tagging device. When characterizing the selectivity of the sensor, special attention must be given to the presence of these trace contaminants.

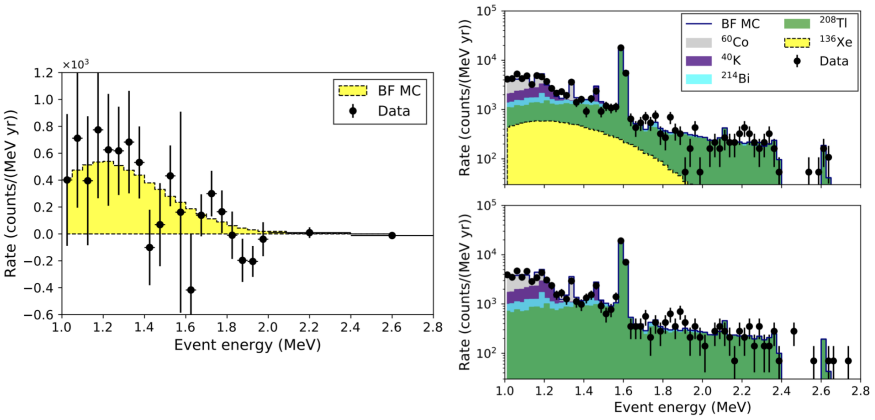

Figure 2.6. Left: Background-subtraction $2\nu\beta\beta$ fit. The best-fit MC (yellow histogram) is superimposed to the data (black dots) with error bars corresponding to the statistical errors. Right: Background-model-dependent $2\nu\beta\beta$ fit. Run V with enriched xenon corresponds to the top spectrum and run IV with depleted xenon correspond to the bottom spectrum. In both cases the event rates (black dots) are superimposed to the best-fit MC, accounting for ^{60}Co, ^{40}K, ^{214}Bi and ^{208}Tl background contributions. Taken from [47].

NEXT-100 constitutes the third phase of the program. Currently under construction, this detector is essentially a 2:1 scaled-up version of NEXT-White, with a total isotope mass of 97 kg at 15 bar and aims to measure the $0\nu\beta\beta$-decay of ^{136}Xe. NEXT-100 intends to accumulate an

exposure of 500 kg yr, thereby reaching a sensitivity of 10^{26} yr in $T^{0\nu}_{1/2}$. It will also serve as a large-scale demonstrator of the NEXT technology for detector masses in the ton-scale.

Scanning the whole inverted ordering parameter space will require tonne-scale scale detectors sensitive to $0\nu\beta\beta$ half-lives above 10^{27} years. Therefore, the fourth phase of the program scales up the detector to the tonne scale, and it is programmed to start in 2029. It will consist of two substages: first, the NEXT-HD detector will deploy about 5 times the mass of NEXT-100 while reducing the background by at least one order of magnitude with minimal changes. In a second step, the NEXT-BOLD detector will implement Ba^{2+}-tagging based on Single Molecule Fluorescence Imaging (SMFI). Barium tagging could provide a handle for NEXT to reach the background-free regime, as no radioactive reaction produces barium in that environment. In that case, the only signal that would mimic the $0\nu\beta\beta$ signal is the $2\nu\beta\beta$ reaction. Assuming 100% barium tagging efficiency and an energy resolution lower than 2%, the signal efficiency in NEXT would increase from 27% to 56%. Furthermore, a global background rejection factor of 10^{-10} for the $2\nu\beta\beta$-mode signal could be attainable, and the background would contribute with around 2×10^{-4} counts after 10 years of exposure [51]. This means a background-free experiment in practice. For 5 years of exposure, a sensitivity of 3.21×10^{27} yr would be reached, corresponding to an upper limit on the Majorana neutrino mass of 10-20 meV. If the ordering of neutrino masses turns out to be normal (i.e. $m_1 < m_2 < m_3$), then the effective neutrino mass might be around 1 meV. In that case, barium tagging could be crucial for any ^{136}Xe-based $0\nu\beta\beta$ experiment. Possible designs of NEXT-BOLD and implementation of SMFI will be further discussed in the following section.

2.5 Designs of NEXT-BOLD detector implementation

In 2015 the scheme on how to collect the Ba ion in a HPXe EL TPC was proposed by David Nygren [52]. The idea was to use a monolayer of molecular sensors covering a dielectric surface. This sensor will be mounted in the cathode plane. The key point here is that the position of the ion arrival at the cathode can be anticipated by reconstructing the locus of the $\beta\beta$-decay (the barycentre of the two electron track).

Since the electrons drift much faster than the ion, the S1 signal would mark the start time t_0 of the event and trigger the barium tagging device to switch on. If the measured energy of the event were found in the region of interest of the $0\nu\beta\beta$ spectrum, a gating grid would be switched off for around 1 ms, letting the incoming ion pass through and arrive to the cathode. The S2 signal would be detected in the anode as well, yielding the topological signal and in particular the barycentre of the track. The combination of a positive single Ba^{2+} signal in delayed coincidence with the two-electron signal would eliminate potential accidental detection of other ions like Ra^{2+} or Sr^{2+}. The scanner system consists of a laser that illuminates the monolayer and a camera or PMT that captures the fluorescence response.

Still today different solutions are being under consideration for the final sensor implementation. One possibility is to cover the whole cathode plane with the molecular receptor and then use a mobile microscope objective to image the fluorophore at the position indicated by the electron track barycenter. A second scheme is to fabricate a small sensor of $\sim$1 cm^2 that would be moved by a robotic arm to the expected position for the ion to arrive. Then, this small detector returns to a fixed position for optical detection. These two designs are illustrated in figure 2.7.

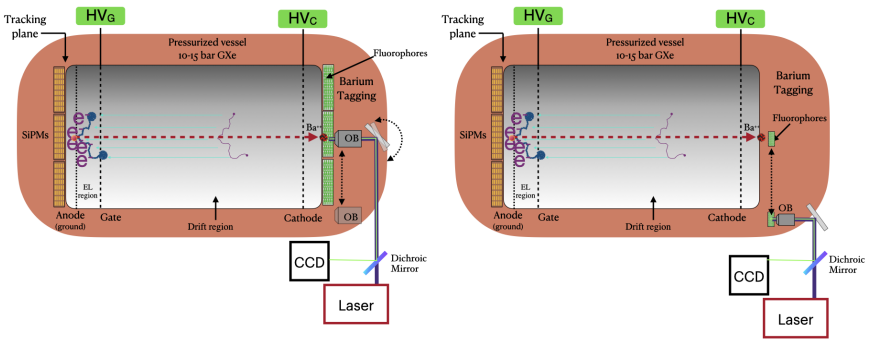

Figure 2.7. Some designs of barium tagging implementation in NEXT without RF carpets. Left: the full cathode is covered with fluorophores and some parts of the optical system (a microscope objective and an aligning mirror) move along the plane. Right: a small sensor moves along the plane, catches the ion and returns to the position of the fixed optical detection system.

Alternatively, a third line involves drifting the ions to the cathode and then guiding them transversely to a small $\sim$1 mm^2 sensor by RF carpets. The system is modularised and composed by several RF carpet sub-units. A plane of $\sim$2 m diameter would be fully covered with seven 30 cm diameter RF carpets. Therefore, the ion must travel 15 cm to the centre of each sub unit. The ions would be focused in these regions by field shaping electrodes. When the ion arrives, a local field of less intensity is switched on in the sweep region. This push field of $\sim$20 V/cm is required for the stable operation of the RF carpets. The switching of this gate would be activated by the expected arrival time of the ion, with the S1 prompt setting the start time as discussed above. The operation of RF carpets in xenon gas is feasible at atmospheric pressure, as the breakdown voltage is much higher than in helium [53]. Moreover, the mass of the ion is enhanced by the formation of ion complex in xenon, so the RF transport is more stable [54]. However, at high pressure the operation of RF carpets becomes much more challenging. Transporting ions for at least 15 cm requires voltages close to the breakdown threshold and micrometric pitches of $\sim$15 μm for large areas. PCB manufacture can achieve down to 50 μm pitches, and even finer meshes have been manufactured for CMOS production. However, producing RF carpets with fine pitches and 30 cm diameter has not yet been realized and poses a remarkable challenge.

Regardless of the final implementation design, the sensor will require to functionalize a surface with fluorescent molecules capable of trapping Ba^{2+} ions with extremely high selectivity and efficiency. This is precisely the objective of this thesis.

3 Barium Tagging in NEXT

3.1 Previous work toward barium tagging

Detecting the $^{136}Ba^{++}$ daughter would provide a way to eliminate all reducible background in a GXe TPC, like NEXT. This asset comes with its due cost: the daunting challenge of identifying one single ion produced in a volume containing a tonne of mother xenon atoms.

A $^{136}Ba^{++}$ dication produced in the $0\nu\beta\beta$ decay, although often in the proccess one or more electrons from the shell are ejected leaving the barium in a double or higher state of ionisation [55]. The ion would then strip electrons for recombination from the surrounding neutral xenon atoms. However, the second ionisation potential of barium is 10 eV and the first ionisation potential of xenon is 12 eV, so the ion would remain as a dication $^{136}Ba^{++}$ in xenon gas. Liquid xenon is more dense so recombination is more likely to happen and lead to a distribution over charge states [56].

M. K. Moe was the first to propose in 1991 barium tagging for background rejection in $0\nu\beta\beta$ searches [57]. Based on his idea, Danilov et al. envisioned a detection method to implement in a gaseous xenon TPC [58]. The monocation Ba^+ is fluorescent: an electron can be excited from its ground state $6^2S_{1/2}$ to $6^2P_{1/2}$ by absorbing a 493 nm blue-green photon. A red fluorescence photon is emitted at 650 nm as the electron relaxes into the metastable $5^4D_{3/2}$ state. The ion would be excited by a laser and its fluorescence detected in-flight, as its drift velocity in high-pressure gas xenon is small. However, the metastable D-state quenches in high-pressure gas or liquid, preventing the spectroscopic features. Furthermore, recombination in the gas phase is minimal ($\sim$ 1.5% [59]) so a transfer gas like TMA ($(CH_3)_3N$) or TEA ($(C_2H_5)_3N$) would be needed to neutralize Ba^{2+} into Ba^+ [60]. Unfortunately, these

gasses quench the scintillation signal S1, preventing reconstruction of the longitudinal position. Lastly, detection in-flight of the fluorescence was assumed to take place where the $0\nu\beta\beta$ decay occurs, but accurately finding this position and steering the excitation lasers toward that point would be a formidable challenge.

Another possibility in liquid xenon is to freeze the Ba^+ ion on a cryoprobe and perform the laser spectroscopy on it [61, 62]. This method was used for detection of single barium atoms [63]. However, it has not been demonstrated to remove atoms from an active experiment.

Single Molecule Fluorescence Imaging (SMFI) was proposed by Dave Nygren in 2015 [52] as a new in-situ Ba^{2+}-detection technique for barium in a high-pressure xenon gas TPC. Detection of single molecules requires a high signal-to-noise ratio (SNR) and a reduced illumination volume. This can be done either by selecting the emission from the molecules on the focal plane by confocal microscopy or by selectively exciting molecules on the focal plane by total-internal reflection (TIRF) microscopy. Repeated interrogation of the field of view can provide a precise localisation of the molecule of interest below the Abbe diffraction limit, to the level of a few nm^2.

For the practical application of this procedure in the final NEXT experiment the molecular sensor has to be immobilized on a surface in a monolayer regime. Moreover, the molecular indicator has to preserve their binding properties once immobilized on the surface. This requires being able to form a complex with the Ba ion in the absence of any solvent. Last but not least, the photochemical properties can not be quenched or attenuated due to the substrate where they are physically or chemically bonded.

3.2 Molecular sensors for Ba trapping

SMFI can be applied to characterise luminescent ion-indicator molecules. The response of these molecules depends on whether they have captured a specific ion or not. Several molecules have been designed in the field of supramolecular chemistry to turn on their fluorescence by binding with specific ions. This binding, also called chelation, constitutes the capture of the ion. Chelation takes place when the molecule or a specific moiety of it forms a coordinated bond with the ion. The

photochemical properties of the molecule-ion coordinated complex are different from those of the free species. Three main photochemical properties of the molecule may change upon chelation: the emission intensity, the wavelength and the relaxation time.

The first molecule proposed in the context of NEXT experiment for the detection of Ba was Fluo-3, a commercially available fluorophore that becomes 60-100 times more fluorescent upon chelation with dications. It is a well known fluorophore in neurology, since it works as a neurotransmitter channel. Detection of single Ca^{2+} ions has been demonstrated in aqueous environments [63] and inside living cells [64]. Since Ca^{2+} and Ba^{2+} are alkaline elements, similar effects for both ions were expected when forming supramolecular complexes. However, the maximum achieved upon chelation with Ba^{2+} was at best 17.4 times more intense than the unchelated species [15, 65]. This value is well below the requirement for NEXT detection (estimated as 10^6 brighter than the free molecule).

Fluo-3 only exploits one of the three main photochemical properties of the molecule that may change upon chelation: the emission intensity. However, two other properties can be used to distinguish chelated from unchelated molecules: the emission wavelength and the relaxation time. There is an intense program in the NEXT collaboration to design molecules which exploit one or more of the aforementioned properties to detect the Ba ions. A scheme of the molecules under study is sketched in figure 3.1, as well as the possible detection mechanisms according to the variation of these properties.

On the left panel (Fig. 3.1a, a napthalimide derivative acts as an off-on indicator or fluorescent monocolour indicator [14]. In these hydrocarbon or heterocyclic scaffolds, an electron-donating group close to the fluorophore (for instance, an amino group of the aza-crown ether) can promote a photoinduced electron transfer (PET) that quenches the fluorescence in the absence of a binding cation. By contrast, sensor–cation complexation results in an off–on enhancement of the photoemission intensity ($\Delta I \neq 0$) [66] with $\Delta\lambda \approx 0$.

Figure 3.1b illustrates the bicolor indicators and their change in emission upon binding to Ba^{2+} ions. A convenient way to generate this kind of sensor consists of generating an intramolecular photo-induced charge transfer (ICT) by modifying the interaction of an electron-donating group with the rest of the fluorophore [67]. Upon

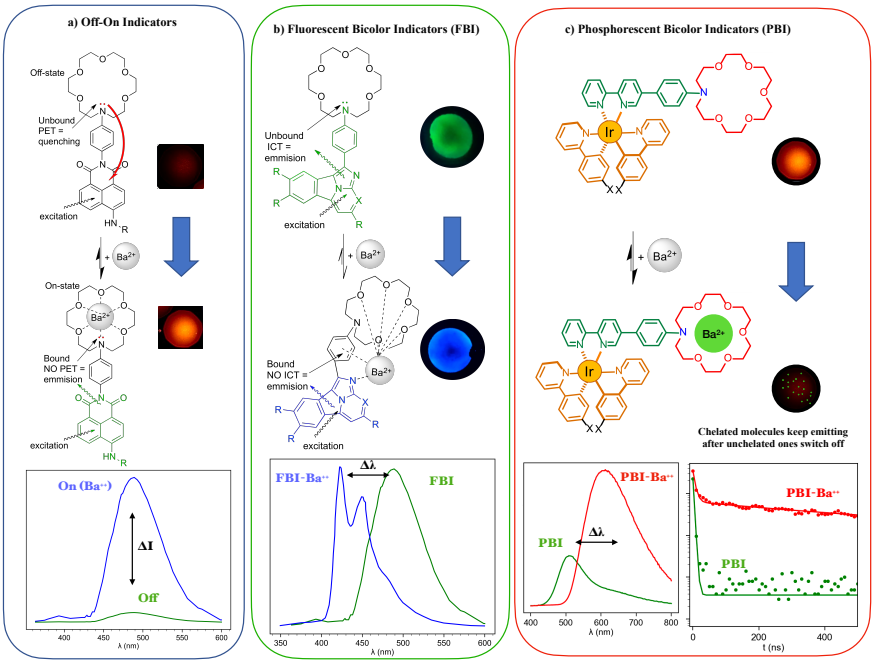

Figure 3.1. Design of a family of molecular indicators. a) Model of a napthalimide derivative and its use as fluorescent monocolour indicator. PET: photoinduced electron transfer; b) Components of an FBI analogue, showing the coupling–decoupling between the fluorophore and the metal-binding group. c) Model of a Phosphorescent Bicolor Indicator (PBI) and the temporal response of the free (PBI) and chelated molecule (PBI-Ba^{2+}) (lower right panel). The respective fluorescent emission spectra are also shown. The blue and green lines in the graphs represent the emission spectra in chelated and unchelated indicators, respectively. In c) the free and chelated species are represented in green and red, which correspond to the peak of each emission. The different behaviour of the two types of fluorescent indicator is shown: in a monocolour indicator, the increase in emission intensity after cation complexation (ΔI) is produced at the same wavelength as the unchelated fluorophore ($\Delta\lambda \approx 0$), whereas in the case of an FBI, the difference ΔI is produced at a different wavelength ($\Delta\lambda \neq 0$). The possible participation of nitrogen heteroatoms and the rotation of one aryl group are also highlighted.

coordination with the cation, the change in the dipole moment of the supramolecular entity can generate a Stokes shift. The design and chemical synthesis of efficient FBIs with large enough emission shift

values still constitutes an important challenge.

Another handle to distinguish the signal of chelated from non-chelated molecules is the relaxation time of the light emission. An example of such molecule is shown in Figure 3.1c). Chelation with Ba^{2+} induces changes in the molecule so that its emission becomes long-lived (phosphorescent). At the same time, color shift can also be induced by chelation, as the case of FBIs. The color spectrum and time response graph are shown in the lower panel. These molecules will be further discussed in chapter 8, whereas we will focus on FBIs for the rest of this thesis. These Phosphorescent Bicolor Indicators (PBI) were synthesized by the group of Prof. Zoraida Freixa from the Department of Applied Chemistry, Faculty of Chemistry in UPV/EHU. More details on the design and synthesis of PBIs can be found in [68].

3.3 Fluorescence Bicolor Indicator, FBI

The characterization of all the FBI molecules along this thesis resulted in the collaboration with the group of Prof. Fernando P. Cossío, from the Department of Organic Chemistry I, University of the Basque Country (UPV/EHU). The synthesis of these compounds is thoroughly reviewed in [69]. This doctoral thesis provides a comprehensive overview of the various methods used to synthesize and characterize the sensors, including recent developments and challenges.

The molecular design and synthesis was carried out with three mandatory requirements that the indicators should fulfill:

1. The chelating group binds the cation with a high binding constant.

2. The indicator response in a dry medium is preserved and preferably enhanced with respect to the response in solution.

3. The fluorophore exhibits a distinct response in the visible region for the chelated and unchelated states (thus the term “bicolour indicator”).

To that end, the synthesis of FBI compounds incorporates a custom-designed fluorophore with two aromatic components, the fluorophore (green or blue regions in Figure 3.1b) and the nitrogen-containing

crown ether group, connected by a free-rotating phenyl group. The main fluorophore component consists of a aromatic polyheterocycle [70–73] that can bind the Ba^{2+} cation, thus modifying its electronic structure and decoupling this moiety from the second aromatic compound, which in turn can generate a π-cation interaction [74]. The expected shift in response to the coordination should provide a strong signature of a bound indicator, exhibiting a blue shift over a background of unbound species.

3.3.1 *Electronic structures*

Electronic structure calculations, performed using DFT (calculations performed by Prof. David Casanova and Dr. Claire Tonnelé and explained in detail in Ref. [75]) confirms the strong binding affinity of FBI to coordinate Ba^{2+}. The optimized FBI-Ba^{2+} structure exhibits a large molecular torsion of the binding group with respect to the free FBI molecule (see the dihedral angle ω in Fig. 3.2b) so that a molecular cavity appears, with the metal cation forming a π-complex between the Ba^{2+} metallic centre and the phenyl group. The oxygen atoms of the aza-crown ether occupy five coordination positions with O–Ba contacts within the range of the sum of the van der Waals radii (2.8–3.0 Å) [76]. Interestingly, the phenyl ring attached to the crown ether is oriented towards the centre of the cavity coordinating Ba^{2+} through the π-electrons. The frontier molecular orbitals of FBI are delocalized over the entire fluorophore moiety, with virtually no participation of the binding-group electrons (Fig. 3.2c).

The lowest bright state of the unbound FBI molecule can be mainly characterized as the electronic transition between the highest occupied molecular orbitals (HOMO) and the lowest unoccupied molecular orbitals (LUMO). Molecular distortion upon metal coordination in FBI-Ba^{2+} has an important impact on the electronic structure. In particular, the torsion of the phenyl group allowing π-coordination breaks the planarity with the rest of the fluorophore, modifying the HOMO and LUMO energy levels. The decrease of the effective conjugation with respect to FBI increases the symmetry allowed $\pi \rightarrow \pi^*$ gap, thus resulting in the blue shift of the fluorescent emission (Fig. 3.2c). Therefore, these results support the viability of FBI as an efficient Ba^{2+} indicator in both wet and dry conditions.

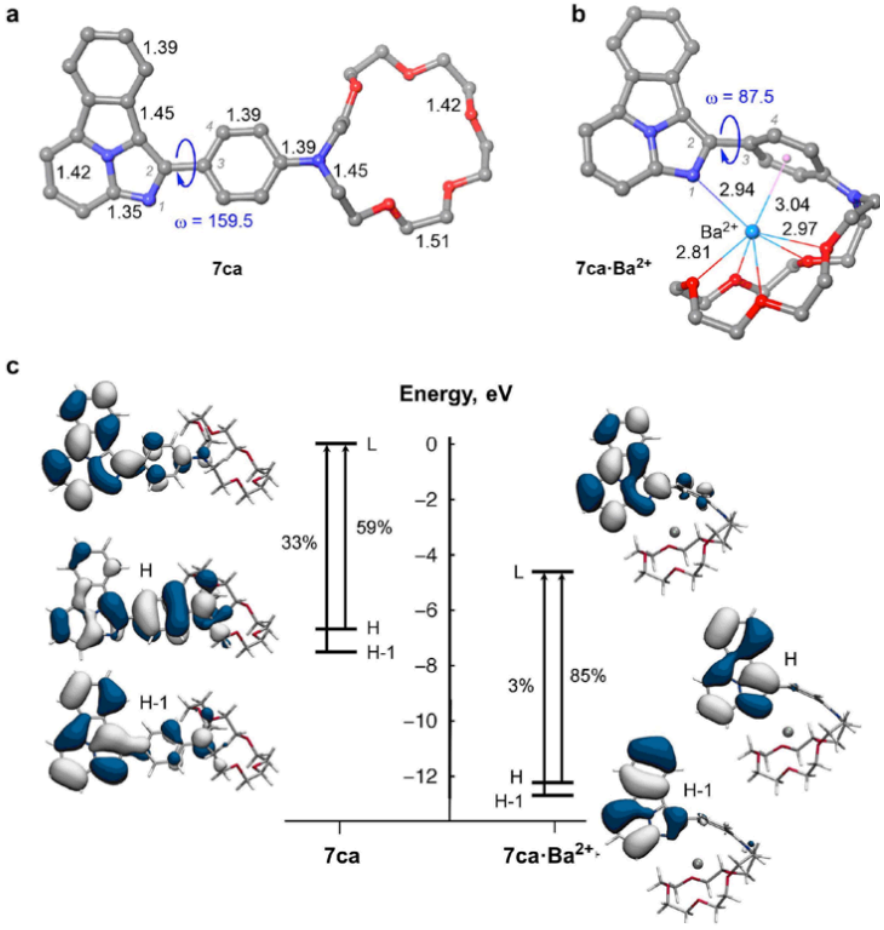

Figure 3.2. Theoretical predictions. **a,b** DFT-derived gas-phase structures of FBI (**a**) and FBIBa^{2+} (**b**). Bond distances are given in Å. Dihedral angles ω formed by covalently bonded atoms 1–4 are given in degrees and in absolute values. **c**, Frontier molecular orbital energy diagram of FBI (left) and FBIBa^{2+} (right). Vertical arrows indicate the main contributions to the electronic transition to the lowest bright state.

3.3.2 *Generations of FBI molecules*

After the promising results obtained for the FBI molecule shown in figure 3.2, different generations of molecules were proposed and synthesized. The objective was to maximize the affinity for Ba^{2+}-chelation

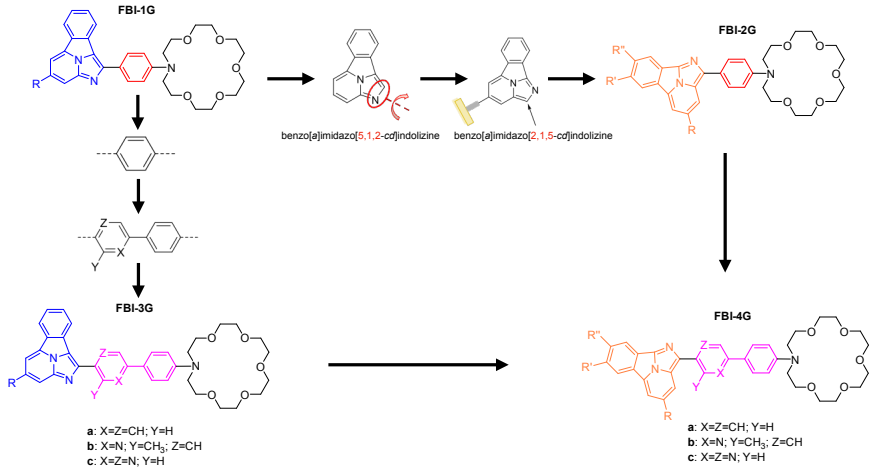

Figure 3.3. Schematic design of new generations of FBI molecules FBI-G2, G3 and G4 starting from G1 (**a**). The permutation of the nitrogen and carbon atom in the benzo[*a*]imidazo[5,1,2-*cd*]indolizine (**b**) results in FBI-G2 (**c**). The addition of an extra phenyl ring (**d**) results in FBI-G3 (**e**) with different varieties depending on the functional group in X, Y and Z. The combination of the two design concepts results in FBI-G4 (**f**). R, R′ and R″ denote possible positions to include anchoring groups such as a carboxylic acid.

and the color shift thus induced. Fig. 3.3 illustrates some of the modifications introduced in the FBI molecules, from now FBI-G1, to obtain the next generations of bicolor sensors. The first modification is a permutation between the nitrogen atom and the carbon atom in the benzoimidazoindolizine moiety on which the phenyl ring is bonded (figure 3.3b). This permutation preserves the capacity of the structure to undergo torsion when the barium is chelated (see section 3.3.1, figure 3.2). Therefore, the fluorophore moiety of FBI-G1, benzo[*a*]imidazo[5,1,2-*cd*]indolizine becomes benzo[*a*]imidazo[2,1,5-*cd*]indolizine and the phenyl ring stays bonded to the carbon atom for FBI-G2 (figure 3.3c). In addition, the structure of FBI-G2 facilitates the inclusion of anchoring groups (R, R′ and R″ in figure 3.3c) with respect to the synthesis of FBI-G1. Adding functional group such as a carboxylic acid would allow to anchor the molecule to a surface by forming covalent bonds (peptide bond) with hydroxy groups on the surface. The design and synthesis of FBI-G2 is further detailed in [69].

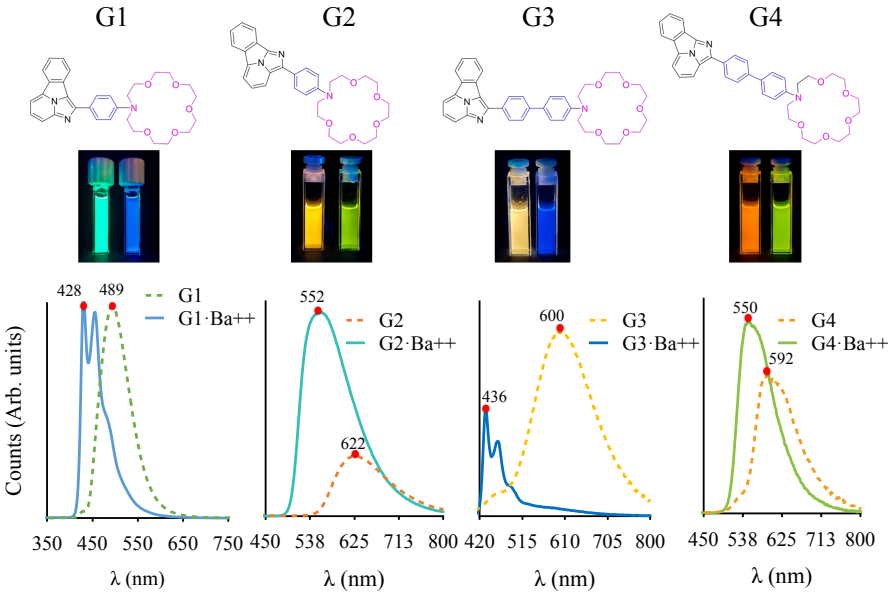

Figure 3.4. Fluorescence spectra of FBI-G1 (**a**), G2 (**b**), G3 (**c**) and G4 (**d**), both free (dashed lines) and coordinated with Ba^{2+}. The positions of the maxima is indicated in every spectrum with a red dot. All spectra were recorded for acetonitrile solutions with a concentration 10^{-5} M. For the Ba^{2+}-chelated species 1 equivalent by mass of $Ba(ClO_4)_2$was used. Images of the different species in solution are included and show the emission color under a UV torch.

The second idea to extend the FBI family is to add another phenyl ring between the benzoimidazoindolizine and the crown-ether (figure 3.3d). This results in FBI-G3 (figure 3.3e). The new ring would add extra degrees of freedom, i.e. the molecular structure can undergo more torsion and/or more bending upon capture of the ion. The Ba^{2+} ion interacted with the nitrogen atom in the benzoimidazoindolizine group in FBI-G1 (and G2). By contrast, the extra phenyl ring in FBI-G3 increases the distance between the crown-ether and the benzoimidazoindolizine, so this interaction with the nitrogen atom is not expected to take place. However, the phenyl group itself does interact with the ion, via π-complex, so the extra recognition point is preserved for G3. Furthermore, the new phenyl ring allows to include different alternatives for functional groups in the X, Y and Z positions which

could enhance the interaction with the ion. The design and synthesis of FBI-G3 is thoroughly reviewed in the doctoral thesis [68].

By combining the two design concepts described above for FBI-G2 and G3, a fourth generation can be synthesized: FBI-G4 (figure 3.3f). This molecule uses the scaffold of G2 with the permuted nitrogen and carbon atoms (benzo[*a*]imidazo[2,1,5-*cd*]indolizine) and the extra phenyl ring of G3. Therefore, FBI-G4 was expected to perform the best, as it combines the best of both worlds. However, this was not the case. The photophysical characterization of these compounds in solution favoured G2 over the rest, and G4 turned out to perform the worst of them. The results of the photophysical characterization are gathered in Figure 3.4.

3.3.3 Barium selectivity

During the design process special attention was given to the selectivity for barium capture over other cation species as a crucial property of the candidate chemosensor. In order to assess this selectivity, FBI-G1 molecules were chelated with other elements. Fig. 3.5 shows the fluorescence spectra of one of the FBI molecules, FBI-G1 (shown in Figure 3.1b)) before and after chelation with all the alkaline earth dications. To this end, solutions (5×10^{-5} M) of FBI-G1 where prepared and mixed with $Ca(OH)_2$, $K(ClO_4)$, $Na(ClO_4)$, $Mg(ClO_4)_2$, $Sr(ClO_4)_2$ and $Ba(ClO_4)_2$ with CH_3CN as the solvent. Our indicator does not present substantial changes to the emission wavelength in the presence of light alkaline earth dications. Only in the presence of Sr^{2+}, FBI-G1 exhibited an emission spectrum similar to that observed for Ba^{2+}. These results show that although FBI-G1 is able to chelate all dications, only the heaviest of them (Sr^{2+} and Ba^{2+}) induce a blue shift. This is very relevant for the selectivity in the final application.

3.4 Surface Anchoring

An important development in molecular design was the addition of a moiety capable of anchoring to a suitable substrate. This is crucial for the development of the microscope, because it must be adapted to fluorescence detection from a field as narrow as a monolayer. Therefore, the anchoring procedure must be controlled to assure that the

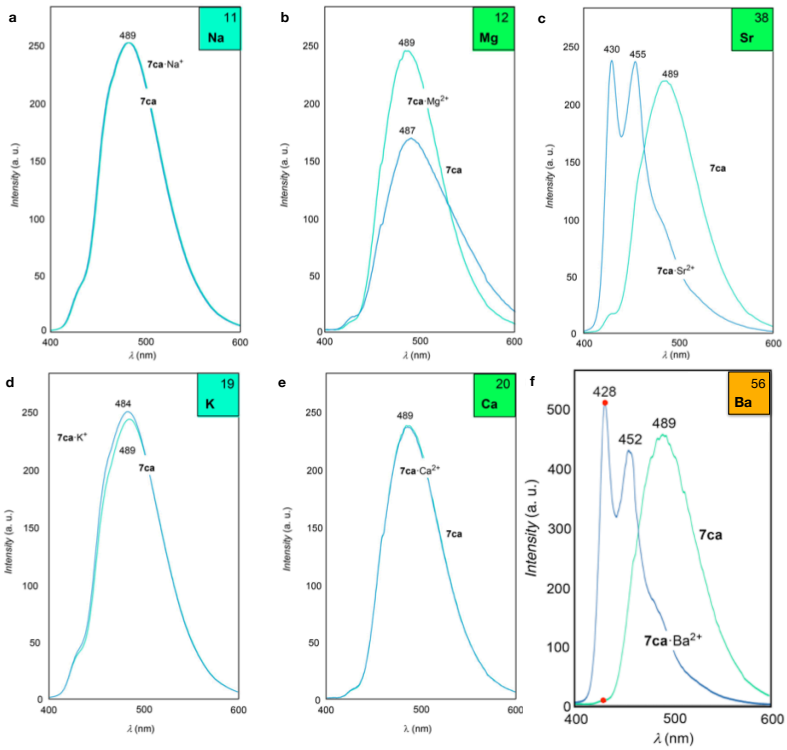

Figure 3.5. Interaction of FBI-G1 with other elements (1:1 equiv.). **a-e**, Blue lines represent FBI + Na+ (**a**), FBI + K^+ (**b**), FBI + Mg^{2+} (**c**), FBI + Ca^{2+} (**d**) and FBI + Sr^{2+} (**e**), and the cyan lines show the corresponding unchelated indicators. In **a-d**, the spectra show that the FBI is not chelated with the ion, whereas in **e** the response is similar to that observed for barium, showing the formation of a supramolecular complex. All excitation spectra were taken at 250 nm.

fluorophores will remain covalently bonded on the surface for its detection.

The final Ba-tagging device will require a monolayer highly ordered and possibly densely pack to maximize the probability of capturing the incoming Ba^{2+} ion. Self-assembled monolayers (SAM) can provide such an orderly packing of the surface. Anchoring the molecule in a "standing position" (i.e. bonded by the fluorophore and with the crown ether heading outwards) can prevent it from interacting with

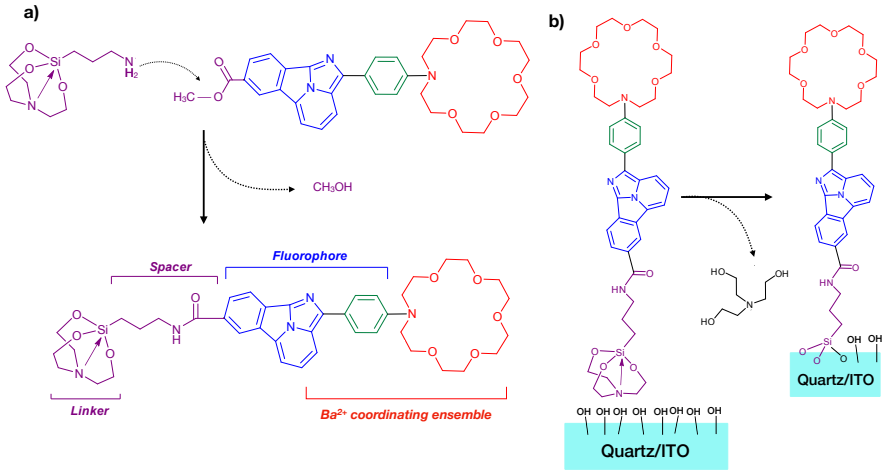

Figure 3.6. Scheme of the immobilization process for G2 on quartz or ITO. **a**) The molecule G2 is adapted to surface linking by synthesizing it with an amide as functional group (top) which reacts with the amine group of the linker molecule by aminolysis. The resulting molecule keeps the fluorophore and Ba^{2+}-coordinating groups of G2 and can bond covalently to a hydroxylated surface via the linker group APS. **b**) Anchoring the G2-silatrane molecule to a hydroxylated surface such as quartz or ITO. The reaction of the silatrane group with the surface is well known [78, 79]. The byproduct $N(OH)_3$ can be cleaned off with water.

the surface. These interactions may be weak, but can jeopardize the structure rearrangement that the molecule needs to undergo in order for its fluorescence emission to shift. In addition, by controlling the mechanism of anchoring to the surface we can tune the packing in order to optimize the chelation efficiency. This could also allow us to design the structure of the layer at will by nanopatterning procedures [77].

The choice of substrate is crucial, since the composition of its surface will determine the sort of covalent anchoring that we can produce. Two basic requirements for substrates are presenting a highly uniform and smooth surface and high optical transparency. The latter requirement can be circumvented if the optical detection is achieved in reflection in the final device. However, it is convenient to have a transparent substrate suitable for transmission microscopy for the R&D

stages. In any case, even if the material is not transparent, it must not introduce any fluorescent background at the excitation wavelengths of the molecule. Lastly, the substrate must be an insulator or a semiconductor because highly conducting materials quench the fluorescence signal due to the imaginary part of the refractive index n [80, 81]. If this imaginary part of n is close to zero, the signal is not completely extinguished and could be compensated for with higher excitation power. A slightly conducting surface entails an extra advantage: it can be biased positively to repel incoming positively-charged contaminants and negatively to attract the Ba^{2+} ion when it is expected to arrive.

Taking the considerations mentioned above, two promising substrates are quartz and Indium Tin Oxide (ITO). Quartz is an insulating, highly flat substrate with excellent optical transmission ($\gtrsim$90%). It can be manufactured industrially (fused silica), although in this case the material does not present any crystalline structure. ITO is a transparent conducting oxide widely used in polymer-based electronics, photovoltaics and as coating for displays (LCDs, OLED, etc.) among other applications. Thin ITO films can be deposited by physical vapor deposition on top of surfaces like quartz, preserving its smoothness. The imaginary part of its refractive index is three orders of magnitude below that of metals and semiconductors [81]. Therefore, a thin layer of ITO ($\approx$ 10-20 nm) is expected to quench mildly the fluorescence of an emitter located at distances of 1-10 nm from the surface. As mentioned above, this reduction of the quantum yield can be compensated with high excitation power.

The composition of quartz and ITO are SiO_2 and $In_2O_3{\cdot}SnO_2$, respectively. ITO is a solid solution of indium (III) oxide and tin (IV) oxide, so their relative proportion varies; a typical composition is 55% O, 41% In and 4% Sn. Both quartz and SiO_2 are metal oxide so their surfaces present hydroxy groups (OH) as spontaneous defects. The abundance of these groups can also be enhanced by plasma oxidation [82, 83]. This type of functional group can be used to form covalent bonds with silane molecules, which in turn bind with each other in a process known as *silanization*.

As the time of writing, the most promising approach to anchor FBI molecules to quartz or ITO is through silanization with 1-(3-aminopropyl)-silatrane (APS) as shown in Figure 3.6. FBI molecules (in

this case G2) must be decorated accordingly for this purpose by adding an ester group to the fluorophore (Fig. 3.6a, top). This way the APS can react with the ester via aminolysis and form a compound suitable for surface immobilization (Fig. 3.6a bottom). The anchoring to the surface is carried out by silanization (Fig. 3.6b). Initially, the reverse procedure was attempted, i.e. first covering the substrate with APS via silanization and then anchoring FBI-G2 on the APS-functionalized surface via aminolysis. However, this yielded worse results in terms of surface homogeneity and a high concentration of unreacted molecules was found after extracting the substrate.

Being able to anchor FBI molecules on a surface takes the sensor to a further step, as a monolayer with a controlled density of covalently bonded molecules can potentially be produced. Chelation efficiency can be studied as a variable of coverage, packing and type of bond. The substrate cleaning and immobilization procedure must be optimized in order to mitigate potential backgrounds from contamination or alteration of the substrate properties. The optical properties of the substrate and indicator-functionalized surface must be characterized to assess the overall efficiency of the sensor. A dedicated optical microscopy setup was assembled for this purpose and will be discussed in chapter 7.

Adapting the synthesis of FBIs to include the functional group with which to anchor them to surfaces required extensive research. The early stages of this research can be found in [69].

3.5 Fluorescence Single Molecule Detection in NEXT-BOLD

As a a proof-of-concept for individual Ba^{2+} ion detection, a collaborating group in the NEXT collaboration used the well-established method of photobleaching [65]. They studied samples of Fluo-3 immobilised in polyvinyl alcohol (PVA) saturated with barium perchlorate ($(Ba(ClO_4)_2$). The samples were illuminated by through-objective total-internal reflection (TIR), which allows to excite with an evanescent field typically less than 100 nm in thickness.

Figure 3.7 shows a selection of results obtained by McDonald et al. The top left panel shows an example of image obtained with the EM-CCD and several bright spots corresponding to the location of

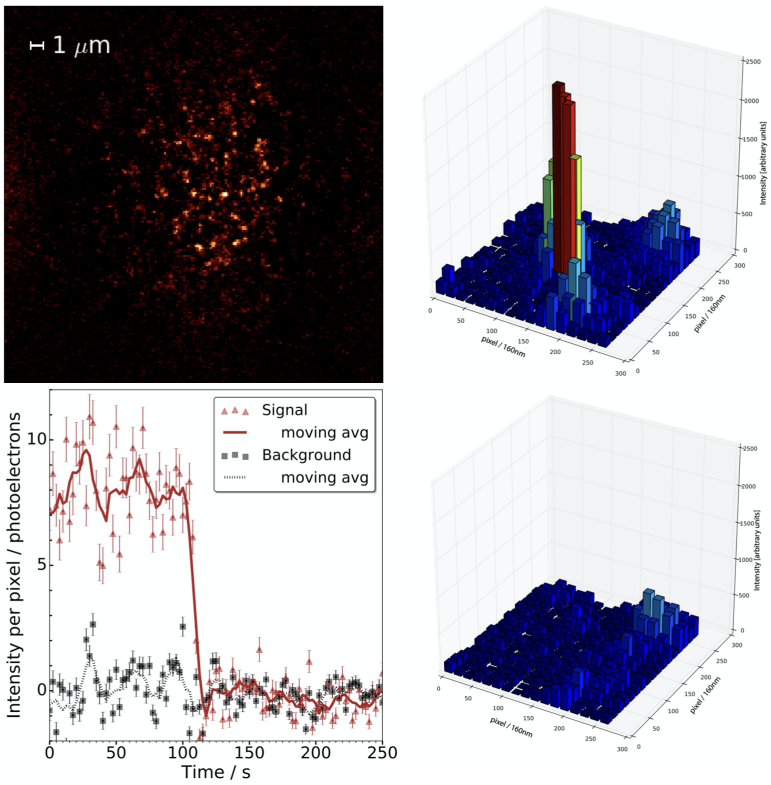

Figure 3.7. (Top left) Field of view of a barium-spiked sample with single molecule candidates. (Bottom left) Fluorescence trajectory of a single molecule event. A single photo-bleaching step is observed. (Right column): a single molecule 0.5 s before and after photo-bleaching. Taken from [65].

single molecule candidates. If the sample was homogeneous the spots would correspond to a cluster of molecules. However, the fluorescence trajectory shown in panel bottom left proves that a single molecule undergoes photo-bleaching in this region. A discrete photo-bleaching transition is the fingerprint o single molecule fluorescence [84]. This transition consists in the extinction of the fluorescence light emitted by a molecule, usually by interaction of the fluorophore with a reactive oxygen species [85]. This sudden switch-off results in the step in the intensity per pixel as visible in figure 3.7. The total scan time is 375 s (up to 250 s is shown in the figure), much longer than the typical

photobleaching time of Fluo-3 at this laser power [85]. This implies that if more than one molecule were to undergo photobleaching during this scanning time, several steps would be seen in the fluorescence trajectory (as many as photobleaching molecules). Therefore, this single step represents the detection of a single-molecule switch-off. The right column of figure 3.7 shows a fixed region of the CCD camera centered on a single-molecule candidate 0.5 s before (top) and after (bottom) the photo-bleaching transition.

This proof of concept shows that TIRF microscopy can be used to resolve SMFI of individual Ba^{2+} ions with 12.9 σ statistical significance above a background of free residual ions. However, the final sensor must differ in a few ways to be implemented in NEXT. First, the fluorophores must be anchored to a surface and in a monolayer regime, instead of embedded in a thick sample and immobilised by a polymer. Second, by removing the polymer, the environment becomes a dry one as the monolayer is exposed to high pressure xenon gas. This may modify the chelation and fluorescence properties of the fluorophore significantly. In addition TIR is generated at the solid-liquid interface to occur, which will not be the case in the final dry scenario. Third, photobleaching may not occur in this clean, ultra-dry environment. Even in the case that it does occur, this implies that the detection of Ba^{2+} ions is achieved in a single attempt, given the irreversibility of photobleaching. We will further address some of these issues in the following chapters.

Alternatively, during this thesis we worked on developing a non-destructive method to detect the fluorescence of Ba^{2+}-chelated indicators. We first used a microscope exploiting Two-Photon Absorption in collaboration with the group of Prof. Juan M. Bueno in the University of Murcia. This yielded the results which will be presented in chapter 5, section 5.1. Building on the experience gained from those tests, we developed our own fluorescence microscope. This setup was tailored with the purpose of detecting the fluorescence of FBI samples prepared specifically for research on barium tagging. Moreover, it will be the basis for the optical detection component of the final sensor in NEXT. This microscope and some results obtained with it will be discussed in chapter 7.

3.6 Conclusions

We are working to define the ideal molecular sensors for Ba tagging in NEXT. In this chapter I have introduced three alternatives of detection mechanisms and different molecules useful for each of them. I have focused on the FBI family, which could be the basis for a barium-tagging sensor in a future gas-xenon-based experiment searching for $0\nu\beta\beta$ decays. FBIs show a bicolor behaviour in solution when they trap Ba but not when other alkaline earths are chelated.

Moreover, I have introduced different light detection methods which are under exploration. I have discussed the method of photobleaching for single Ba^{2+} ion detecion and its limitations. To overcome this drawbacks and optimize the detection of FBIs, we have been developing a microscope which is described in detail in chapter 7.

4 Molecular deposition by Atomic Layer Injection

As we discussed in the previous chapter the capability of FBI molecules to capture Ba^{2+} in solution was established by fluorescence experiments [75]. However, the final implementation of a Ba-tagging device in NEXT will require the detection of the fluorescence signal from the molecular sensors immobilized on a surface. Furthermore, the sensor must be operated in conditions of Ultra-High Vacuum (UHV) to maintain its purity. In order to do that in a controlled way, i.e. dosing the Ba^{2+} ions on the immobilized sensors in UHV, we use Atomic Layer Injection (ALI), which was a novel technique when we started this thesis. This technique is relevant because it allows to introduce liquids in UHV. Some large molecules can lose their structure and properties when heated or dried. This implies that ordinary thermal sublimation is not suitable to grow molecular layers in UHV and that alternative techniques, like ALI, must be used. Thus, this thesis started by exploring the deposition of the molecules from solution under UHV conditions. Moreover, the injection of droplets containing barium onto FBI molecules can be used to simulate the arrival of the Ba^{2+} ions to the sensor. The solvent evaporates during the injection, so the chelation of Ba^{2+} takes place in dry conditions.

Since the ALI deposition technique was novel, we started by assessing its performance. Thus, I explain the characterization of the ALI system in this chapter. After this explanation, I present some results obtained for deposition and chelation of $Ba(ClO_4)_2$ molecules by FBI-G1 absorbed on a silica pellet. Then I evaluate the possibility of using ALI to deposit FBIs directly on a substrate in UHV.

Finally, I would like to remark that the performance characterization carried out here in the context of NEXT experiments is useful for other disciplines and molecules. As an example, we used ALI to

deposit another large macromolecule: starphene. Although starphene is not related to barium tagging, the experiment is relevant because this molecule cannot be deposited in UHV by conventional methods; the large size of the molecule caused it to break before sublimating intactly. We include a summary of this experiment here to prove the relevance of developing the ALI method beyond the context of barium tagging.

4.1 Atomic Layer Injection

Atomic Layer Injection (ALI) is considered a technique within the field of surface science. In this field, the properties and phenomena of systems like solids and molecules are studied in the interface between solid and liquid or gas phases at the nanoscale. The techniques encompassed in surface science are constrained to scrutinize the topmost few nanometers of a surface and atomic resolution is often attainable. Individual molecules can be studied on surfaces under different conditions, which is of utmost importance for the development of a barium-tagging sensor.

The quest to study molecular materials and most importantly, solution-based organic materials synthesized by different bio(chemical) routes, using enhanced surface science technique in UHV is at the heart of nanotechnology [86]. By definition UHV systems are not designed to operate with liquids since the introduction of these solutions leads to a rise in the pressure inside the UHV chamber. Thus, introducing solutions in UHV required the use of novel injection systems. Most preferably, these would help to overcome the UHV challenge and keep the integrity of our sample during and after the deposition period. Although there are other commercially available solutions to deal with the deposition of molecules from solution in UHV, such as Metal Organic Chemical Vapor deposition Method (MOCVD) or Liquid Source Chemical Vapor Deposition (LSCVD), we will focus on ALI. This method allows to leak a minimal amount of solution in a UHV chamber via a pulse valve, causing a sudden increase in the chamber pressure that is rapidly recovered by the pumping system. In this manner, a highly volatile solvent is efficiently pumped, while the solute falls following a ballistic trajectory and making use of the

pressure gradient [87].

The ALI system we used was one of the prototypes commercialized by the Spin-off company Bihurcrystal when this thesis started [88]. They followed the original idea of J.M Sobrado and J.A. Martin Gago [89]. We worked closely with the company and provided them with feedback on characterizing the performance of their device, analyzing the response for different solvents, different solutions concentration and different pressure regimes. Some of these studies are summarized after the setup description.

Setup description

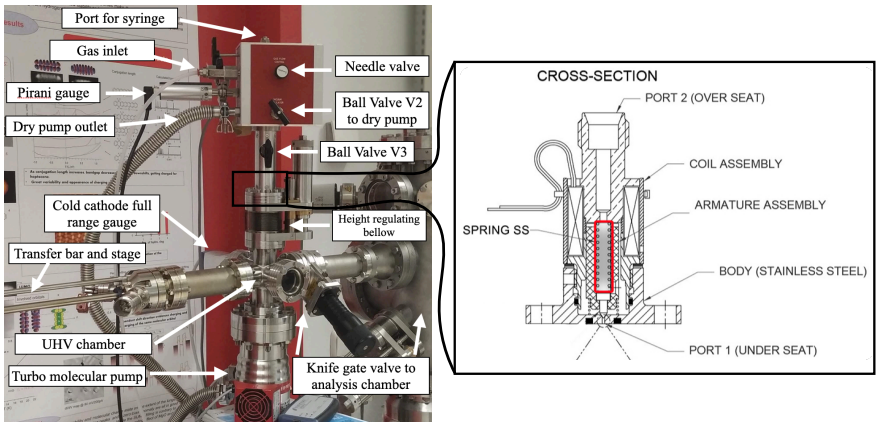

Figure 4.1. (Left) elements of the ALI setup used for this work. (Right) Pulse valve cross-section structure, adapted from [90]

Figure 4.1a shows the main elements composing the atomic layer injection setup. They can be divided into two major groups according to the two pressure stages involved in the process: the pre-injection system, where the solution is prepared for the injection at ambient pressure; and the UHV system. The latter is achieved at a stainless steel T-shaped chamber via a turbo molecular pump (TMP). The substrate to receive the droplets from the injection is installed in a stage at a transfer bar. This way, once prepared, the sample can be transported to a connected analysis chamber.

The solution is first introduced in the pre-injection system via a leak-tight glass syringe through a 20-cm stainless steel needle. The

needle is designed to reach the liquid reservoir at the overseat port of the pulse valve. Once the solution is placed at the reservoir, the ball valve labeled “V3" is closed to isolate it from the rest of the pre-injection piping system. A carrier gas (usually nitrogen or argon) is flushed through this piping circuit to purify when exposing it to the atmosphere. Then the pressure at the pre-injection chamber is regulated by means of the needle valve and the dry pump. Before the injection the valve “V3" is opened to communicate the carrier gas and the liquid reservoir. The pressure from carrier gas and the vapor pressure of the solution is read by a Pirani gauge and can affect the injection in several ways [87].

The injection or pulse valve is the main element of the ALI system. It consists on a small orifice connecting the reservoir of the liquid solution with the UHV chamber. The orifice is sealed by a teflon (PTFE) poppet as shown in figure 4.1b. A plunger cylinder connected to the poppet is displaced upwards when the coil is activated, letting the liquid flow into the chamber. The system can produced highly reproducible pulses of down to 1 ms and has a leakage rate of 10^{-7} mbar·l/s.

4.2 Pressure curve analysis

Several parameters of the injection can be tuned to optimize the amount and purity of the depositions: the concentration of the solution, the opening time of the pulsed valve, the threshold pressure to close it, the minimum base pressure required and the backing gas pressure. However, the main parameter to characterize the injection is the pressure in the UHV chamber and its time evolution. This time profile of the chamber pressure can be used to differentiate between injections of solvent, gas or dissolved molecules. Therefore, in this section I describe how the pressure time profile (or pressure curves) is recorded and analyzed.

When the pulse valve is activated, a small amount of liquid is let into the vacuum chamber, producing a spike in the chamber pressure and being rapidly pumped out. This behaviour, very much alike a virtual leak, is reflected in the vacuum chamber pressure curve, which is recorded by the full range cold cathode gauge. Figure 4.2 shows two

examples of cycles of 6 consecutive pulses. The solutions used for this example were a 1 μM solution of FBI-G1 in acetonitrile (left) and the pure acetonitrile solvent (right).

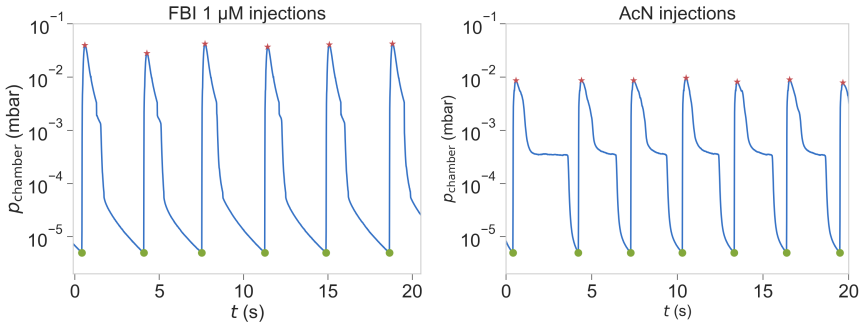

Figure 4.2. Pressure curves recorded by ALI. (Left) molecular injection of FBI solution in acetonitrile (AcN) 1 μM. (Right) injection of acetonitrile solvent only. Both sets of injections were carried out at an argon pressure of 400 mbar and with a pulse duration of 10 ms. The peak pressure of each pulse is indicated by red stars and the end of each pulse is indicated by green dots.

Several features are recognisable from these curves.

1. The injections are highly reproducible, with the pressure keeping a similar profile for as long as hundred pulses in the case of acetonitrile. The latter is a highly volatile solvent and the reservoir maximum load (0.3 mL) gets depleted in approximately 200 pulses, although this depends greatly on the injection conditions.

2. There are two possible conditions to launch a new pulse: either reaching a specified actuation pressure (1 and 5 mbar for figures 4.2 (left) and (right), respectively) or setting a minimum wait time between pulses. In the latter case, during this wait time the chamber can be pumped below the actuation pressure, as can be seen for some of the pulses in figure 4.2. The end of each pulse and the beginning of the next is indicated in the figure by a green dot.

3. The presence of a solute immediately affects the shape of the curves. The solvent is efficiently pumped yielding a steep pressure decrease. When the solution is as diluted as of 1 micromolar,

the pressure drop is slower at the beginning, then decreases suddenly in a similar fashion as in the previous case. This first slower stage can be related to the time it takes for the molecule to land on the substrate and be dried off. Thus, this behavior should depend as well on the distance between the substrate and the pulse valve outlet.

We can overlay these pulses and compute the average profile over several injections within the same run. This can give us some insight on the overall physics taking place during the injections. The overlaying of some pulses of the 1 μM FBI-G1 solution are shown in figure 4.3 (left) and the resulting average profile in Figure 4.3 (right). The shaded regions indicate the 1-sigma confidence interval of this average profile. The average profile of the solvent injections is also displayed for comparison.

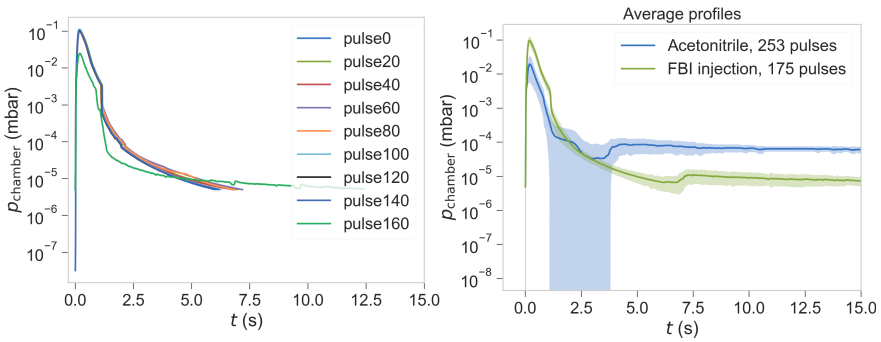

Figure 4.3. (Left) overlaying of pulses for averaging. (Right) resulting average curve for FBI-G1 1 μM solution (blue) and pure acetonitrile (green).

It is easy to notice that the maximum pressure reached at the UHV differs by about an order of magnitude between both experiments, despite being injected with the same carrier gas pressure. This is to expect, since the solute is a solid contribution that cannot be as efficiently pumped as the solvent. A longer recovery time reflects the presence of solute as well. For the acetonitrile injections, most of the peaks take around to 2.5 s (see also Fig. 4.3), so the 1-σ confidence interval is broader in that band. Some acetonitrile peaks can last for up to 15 s, so the average curve reaches that time period (although

with much less variation). Hence, two representative features of each experiment might be the maximum pressure reached and the time it takes to recover a certain pressure level. Figure 4.4 gathers these features in a scatter plot. Both the maximum pressure and the recovery time have been plotted together on their own y-scale to show the correlation between them.

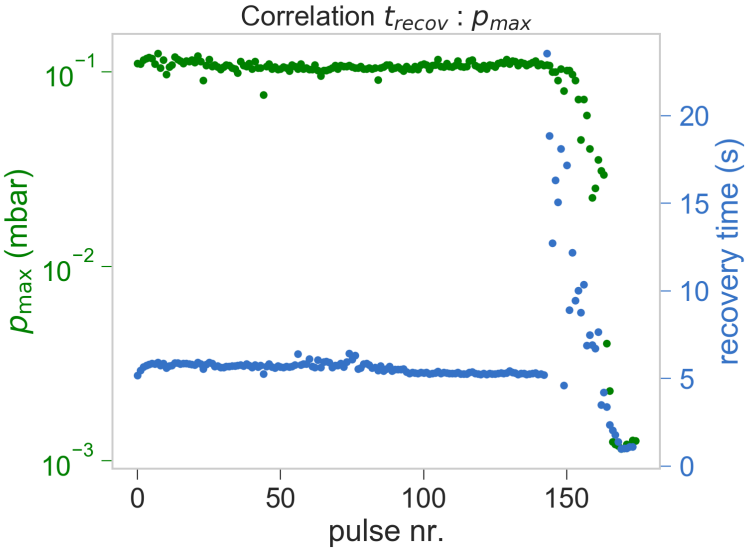

Figure 4.4. Maximum pressure reached and recovery time for FBI-G1 1μM solution

Notice that the peak pressure and the recovery times are almost constant up to the first 150 pulses. This proves that the injections are highly reproducible. However, both parameters start fluctuating for the last 50 points. This difference is precisely what allows to distinguish clean injection pulses from irregular ones.

The last few points in figure 4.4 suggest the solution is being depleted: around pulse number 140 the liquid reservoir is starting to get empty and more and more vapor is being injected in its stead. Since gas is easier to pump than liquid, both the recovery time and the maximum pressure start to drop quickly when all the liquid has been injected. This should be reflected as a noticeable difference in the

pressure profile between the last pulses and the rest.

We then consider two types of pulses:

- **Wet pulses**: the ones reaching a maximum pressure close to the average along the run.
- **Dry pulses**: those deviating by more than a standard deviation from the average.

Figure 4.5 shows this classification. We now plot separately the average shape of dry and wet pulses and perform the same operation with the pure solvent data. By comparing these profiles as in figure 4.5, we see that while the pulses classified as 'dry' are quite similar for both the solvent and solution runs, this does not hold for the 'wet' ones. This suggests that dry pulses correspond to injections of gas, either argon or acetonitrile in vapor form. In other words, dry pulses are produced with the reservoir mostly depleted of liquid. Thus, these injections reach a lower peak pressure than wet pulses, which consist of liquid injections (either of solution or pure solvent).

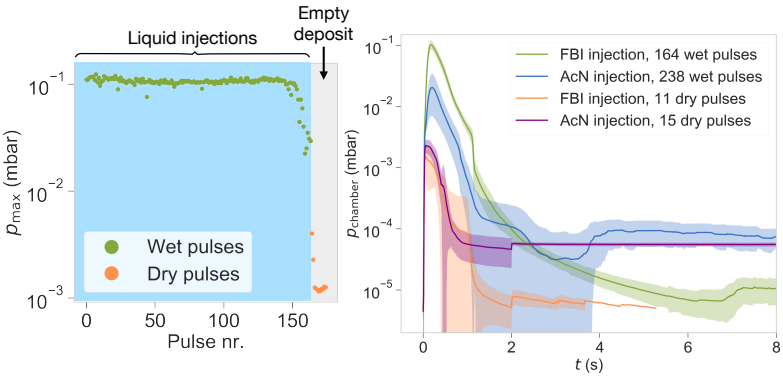

Figure 4.5. (Left) pulse classification by maximum reached pressure. (Right) Average curve profiles of the resulting classification.

Magnitude	Total load	Per pulse	Per wet pulse
V [mL]	0.3	1.7×10^{-3}	1.8×10^{-3}
N [# molecs]	1.8×10^{14}	1.03×10^{12}	1.10×10^{12}
m [g]	1.59×10^{-7}	9.07×10^{-10}	9.6×10^{-10}

Table 4.1. Amount of solute injected for FBI-G1 deposition.

4.3 Estimation of injected number of molecules

An important magnitude to characterize the deposition is an estimation of the number of molecules injected per pulse and over the whole run. Here, I will discuss two approaches to this estimation.

a) Estimation based on the initial solution volume:

The simplest approach assumes the concentration of the solution is homogeneous during the whole process. Hence, it is possible to estimate the injected volume at each pulse as the total solution volume in the reservoir divided by the number of pulses needed to deplete such volume: $V_{\text{pulse}} = V_{\text{load}}/\#_{\text{pulses}}$. Then, by multiplying by the molar concentration, c (assumming homogeneity), we infer the solute amount of molecules in each pulse: $N_{\text{pulse}} = V_{\text{pulse}} \cdot c \cdot N_A$, where $N_A = 6.023 \times 10^{23}$ is the Avogadro constant.

We can further assume that the solute is only present in the liquid contribution of the injections, i.e. only for the wet pulses any solute is really being injected. In this case, we would substitute the total number of pulses $\#_{\text{pulses}}$ (175 in the previous example for FBI injection) by the number of *wet* pulses $\#_{\text{wet}}$= 164, in the case shown above.

Table 4.1 gathers these estimations for the experiment shown in the previous section: injection of 0.3 mL, 1 μM solution of FBI-G1 in acetonitrile, with a gas carrier pressure of 400 mbar. The last row shows the mass in grams corresponding to these amount of molecules by dividing over using the molecular weight of FBI-G1, m_u = 529 Da.

b) Estimation based on pulse shape analysis:

An alternative approach is based on computing the total leak rate of each pulse. The instantaneous leak rate $q_L(t)$ is defined as

$$q_L(t) = \frac{\Delta(p \cdot V)}{\Delta t} = \frac{\Delta V}{\Delta t} \cdot p + \frac{\Delta p}{\Delta t} \cdot V = S_{\text{eff}} \cdot p(t) + \dot{p}V, \qquad (4.1)$$

where S_{eff} is the effective pumping speed of the system, p is the UHV chamber pressure and V its volume. Consider both terms on the r.h.s. of equation 4.1. The first one dominates in a steady pressure scenario, as $\dot{p} \approx 0$. This is the scenario assumed in [87, 89, 91]; however, I will show that this term is subdominant as the pressure rises in a very short time, so this scenario does not provide an accurate representation of the injection.

In the computation of both terms, only the stage of pressure raise is considered, as it is at this stage when the liquid evaporation contributes to the pressure in the chamber. During the pressure drop, different pumping systems act and outgassing blurs the injection contribution. Figure 4.6a illustrates this rise stage as filled area under the pressure curve for different pulses. The correlation of the integrated area with the maximum reached pressure is depicted in figure 4.6b.

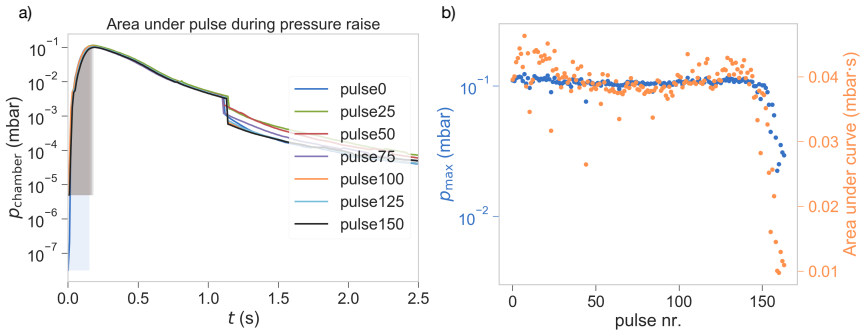

Figure 4.6. (a) Pressure rise stage from pulsed injection. (b) Correlation between area under curve and maximum reached pressure.

Call the two terms of equation 4.1 steady leak rate, $q_{\text{ste}}(t) = S_{\text{eff}} \cdot p(t)$; and dynamic leak $q_{\text{dyn}}(t) = \dot{p}V$. We estimate the chamber volume to be $V = 4.7$ L and the effective pumping speed $S_{\text{eff}} = 0.26$

L/s. The latter accounts for the conductance at the output of the TMP, where its efficiency is limited by the diameter of the exhaust tube. Since we are interested in the total leak rate during the stage of pressure rise, we integrate these instantaneous values from the start until the culprit of the injection. In practice, we compute numerically the area under the pressure curve (shown in figure 4.6) and its derivative. Averaging over the 167 'wet' pulses, we obtain leak rates of $q_{\text{ste}} = (2.0 \pm 6) \times 10^{-3}$ mbar·L/s and $q_{\text{dyn}} = (4.5 \pm 1.4) \times 10^{-3}$ mbar·L/s. As expected, the dynamic contribution is greater than the steady one by a factor 2.5.

Then, the number of molecules injected is estimated by assuming an ideal gas causing the pressure raise. Then, from equation 4.1, we obtain:

$$Q_L = \frac{\Delta(p \cdot V)}{\Delta t} = R \cdot T \cdot \frac{\Delta n}{\Delta t}, \tag{4.2}$$

$$\Delta n = \frac{Q_L \cdot \Delta t}{R \cdot T}, \tag{4.3}$$

where, T is the temperature (room temperature in our experiments), R is the ideal gas constant ($R = 0.082$ mbar $\cdot$l/(mol·K)), and Δt is the total time the pressure rise lasts (around 0.1 s in the current example). Here capital Q_L refers to the total leak rate, resulting of integrating the instantaneous one defined in equation 4.1.

This computation yields an estimation of the total amount of molecules entering the chamber, $\Delta N = N_A \cdot \Delta n = 2.0 \times 10^{16}$ molecs. The fraction of solute (FBI) to solvent (AcN) is given by:

$$x_{\text{sol}} = \frac{\Delta N_{\text{FBI}}}{\Delta N_{\text{AcN}}} = \frac{M_{\text{AcN}}/\rho_{\text{AcN}}}{1/c - M_{\text{FBI}}/\rho_{\text{FBI}}} = 1.9 \times 10^{-5}, \tag{4.4}$$

where $c = 1$ μM is the solution concentration, ρ_{AcN} = 783 g/L and M_{AcN} = 41 g/mol denote the mass density and molar weight of the solvent (acetonitrile). Similarly for the solute (FBI molecule) ρ_{FBI} = 5038 g/L and M_{FBI} = 529 g/mol. Thus, equation 4.4 yields $\Delta N_{\text{FBI}} = 3.8 \times 10^{11}$ molecules per pulse.

This result differs by a factor 3 from that on table 4.1, where $N_{\text{FBI}}^{\text{max}} = 1.10 \times 10^{12}$ molecs. per pulse. However, this latter is actually an upper boundary: the maximum molecules that could enter the UHV chamber.

Several assumptions underlie this estimation: homogeneous concentration in the whole reservoir and that no molecule precipitates, sticks to the pulse valve or evaporates when exposing the liquid in the reservoir to the carrier gas. This last assumption is not accurate taking into account the high volatility of acetonitrile, with a vapor pressure of 130 mbar. The second estimation is independent from the distribution of solute in the pre-injection reservoir as it relies on the data from the pressure rise when the liquid enters the UHV chamber. However, it still assumes that the concentration is homogeneous and that the solute does not fall preferentially by gravity but is spreaded throughout the whole chamber.

From our experience, the second method provides a more accurate estimation on the actual number of molecules being injected in the chamber.

4.4 Chelation of FBIs with $Ba(ClO_4)_2$ deposited by ALI

The first studies of the photophysics of FBI-G1 and its response to Ba^{2+} chelation was carried out in solution. To that end, solutions of FBI-G1 (5×10^{-5} M) were chelated with $Ba(ClO_4)_2$ in a ratio 1:1 Ba^{2+} to FBI. The resulting emission spectra is shown in Fig. 3.4. A blue shift of $\Delta\lambda = -61$ nm was measured between the chelated and unchelated emissions.

However, the molecules must be deposited on the surface of a solid substrate, so we tested silica as initial solid support. Silica powder was compressed into pellets and a FBI-G1 solution was deposited onto them. The solvent evaporates in air and FBI-G1 is trapped in the pellet. Then the pellet was wet with $Ba(ClO_4)_2$ solution and let dry again. This yielded similar results as those obtained entirely in solution.

As a next step we tested whether the chelation still takes place when we greatly reduce the amount of solvent at the moment of depositing the $Ba(ClO_4)_2$. To this end we used ALI to inject $Ba(ClO_4)_2$onto FBI-G1 adsorbed on the silica pellets. In addition, this allowed to test if the chelation took place under UHV conditions.

For this test we used a silica pellet containing 2.3×10^{-8} mmol of FBI-G1 molecules per mg of silica (1.3×10^{15} molecules). Two similar pellets (SFpA and SFpB) were prepared by depositing 7.4×10^{-8}

mM of FBI-G1 indicator per milligram of silica, which is equivalent to 1.3×10^{15} molecules of FBI. One was kept as a reference for unchelated molecules (SFpA), and the the other was introduced in an UHV chamber (Fig. 4.1a) in which barium perchlorate was deposited (SFpB). The silica-FBI-G1 pellet was placed on a stage in the UHV chamber, directly under the exit of the ALI pulse valve. The separation distance was 20 cm.

Next, a 0.5 mM solution of barium perchlorate $(BaClO_4)_2$ in acetonitrile was used for the chelation. In order to maximize the amount of barium being deposited, we chose the maximum concentration recommended to avoid solute clogging the pulse valve orifice. Furthermore, the pre-injection pressure (argon) was set to its maximum of 1 bar, to minimize acetonitrile evaporated from the liquid reservoir. The opening time of the pulse valve was 50 ms, the minimimum recovery pressure was 1×10^{-6} mbar. The pulses lasted as long as necessary to recover this actuation pressure. Five consecutive loads of 0.3 mL solution were injected in the UHV chamber. After each batch was depleted, the liquid reservoir was reloaded with a fresh solution and the pre-injection chamber was purged by argon flushing.

In this experiment, of the total 963 pulses, 496 were classified as dry and 466 as wet. This implies that more than half of the pulses were likely unuseful in the deposition process. The average shape of the wet and dry pulses for this experiment is compared in figure 4.7. In this graph, we zoom on the first 1.2 s, to see the detailed shape of the peak immediately after injection. The confidence interval of each average is shown as a shaded region; in the case of the wet pulses, the fact that this region is very narrow hints that these pulses were highly reproducible.

We now estimate the amount of injected molecules as in section 4.3. This will yield an approximation of the final coverage obtained. Since the solution reservoir was filled 5 times with 0.3mL of solution, the pellet was exposed to 1.5 mL of solution (at 0.5 mM concentration) as upper boundary. This sets a maximum of $N_{\mathrm{Ba}}^{\mathrm{enter,max}}$ 4.52×10^{17} molecules deposited in the entire experiment.

This value can be compared with that obtained by computing the total leak rate using equation 4.1, as explained in Section 4.3. Thus, at every wet pulse, $Q_L = 0.808 \pm 0.008$ mbar·L/s. The values of mass density and molar weight used in equation 4.4 for the barium

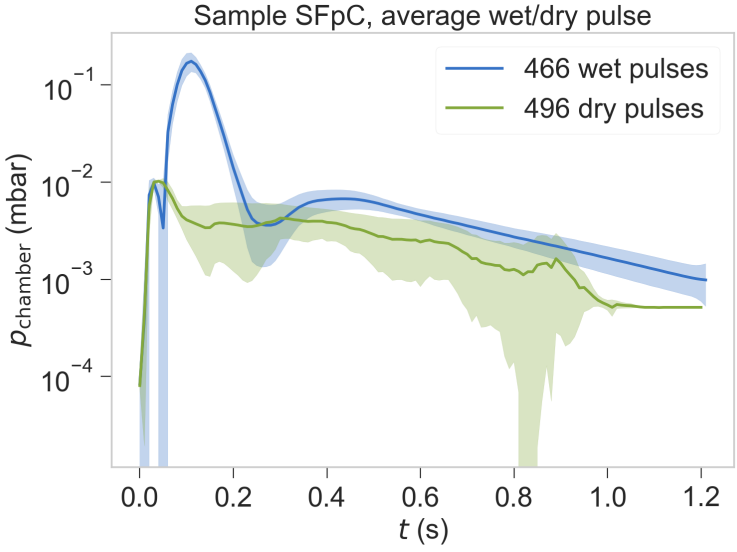

Figure 4.7. Average pressure profile comparison for dry and wet pulses in $Ba(ClO_4)_2$ injection onto SFpB.

perchlorate solute are $\rho_{BaP} = 3200$ g/L and $M_{BaP} = 336.3$ g/mol, respectively. Considering an homogeneous concentration, $c = 0.5$ mM, this yields a fraction solute/solvent of $x_{sol} = 9.6 \times 10^{-3}$. Thus, the number of barium perchlorate molecules entering the chamber would be $N_{Ba}^{enter} = (1.40 \pm 0.01) \times 10^{16}$.

However, this value would represent the upper boundary of number of molecules deposited on the sample in an ideal case, i.e in a situation where all the pulses contains exactly the same amount of molecules and all the molecules reache the surface. But reality strongly differs from ideal conditions. First, not all the molecules entering the chamber will arrive to the pellet. The pellet diameter is 2 cm and a maximum injection surface can be approximated as the chamber cross sectional area, with a diameter of 69 mm (CF63). Dividing both areas, we estimate a collection efficiency $\varepsilon = 0.026$. This factor assumes that the spray cone has a maximum angular aperture of 12°, which falls in the range measured by [89]; however this would be an overestimation if the cone were wider than that, as the molecules in that part of the

spray (arguably, mostly solvent) would then collapse with the walls of the chamber.

To test this, we studied the variation with the position of the deposited mass measured by a Quartz Microbalance (QMB). In other words: we probed the content of the spray cone in and away from the axis. For this study we kept the injection conditions fixed at $p_{\text{pre-inj}} = 1$ bar, $t_{\text{on}} = 50$ ms and $N_{\text{pulses}} = 20$. Using a linear bellow drive, we displaced the QMB from the center of the UHV chamber (the cone axis, z = 0) as far as 28 mm, in steps of 4 mm. Figure **??** schematically illustrates this procedure.

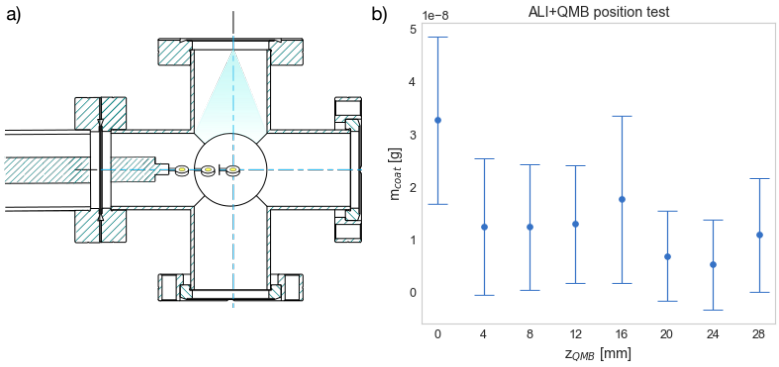

Figure 4.8. (a) Scheme of QMB position test. The yellow circle represents the quartz crystal. (b) Dependence of deposited mass with QMB z-position.

Table 4.2 gathers the total injected $Ba(ClO_4)_2$ molecules, according to both approaches, and accounting for a collection efficiency of $\varepsilon = 0.026$. The estimated number of injected $Ba(ClO_4)_2$ molecules is of the order of 10^{14} molecules.

In order to predict whether this $Ba(ClO_4)_2$ molecules chelate the molecules in the pellet, DFT calculations were perfomed. The calculations showed an exergonic nature for the binding of $Ba(ClO_4)_2$ to the FBI-G1 in absence of solvent. Importantly, the process evolves spontaneously when the system FBI-Ba^{2+} starts at distances of around 1 nm between ion and molecule. From these calculations, we can conclude that the formation of supramolecular complexes implies that FBI-G1

Magnitude	Total volume approach	Leak rate approach
N_{enter}	4.5×10^{17}	$(1.40 \pm 0.01) \times 10^{16}$
$N_{\text{arrive}} = N_{\text{enter}} \cdot \varepsilon$	1.19×10^{16}	$(3.65 \pm 0.03) \times 10^{14}$

Table 4.2. Amount of solute injected for $Ba(ClO_4)_2$ deposition on FBI-silica pellet. The error estimation is based on the standard deviation for the areas of the 496 peaks.

indicators can chelate Ba^{2+} in the absence of solvent.

In addition, the chelation of FBI-G1 in the pellet was tested experimentally. The samples were characterized in a Two-Photon absorption (2PA) microscopy setup described in section A2.1. Figure 4.9 shows the tomography images measured for SFpA and SFpB. Each visible point in the image corresponds to a (Z, X) position determined by a system of imaging mirrors. The $Z - X$ tomography image acquired on the reference FBI pellet (SFpA) using the green filter (Fig. 4.9a) reveals a region of about 20 μm in depth that corresponds to the area of the pellet where FBI molecules were immobilized. Because these are unchelated molecules, they are visible with this filter but not with the deep-blue filter (Fig. 4.9b). Instead, the sample exposed to $Ba(ClO_4)_2$ (SFpB) presents some emission in the deep-blue region of the spectrum (Fig. 4.9c). These emission can only correspond to chelated FBI molecules. Therefore, deposition of $Ba(ClO_4)_2$ by ALI produced some molecular chelation.

Thus, with this initial experiment we manage to confirm that, the Ba^{2+} ions can be trapped by the sensors even under vacuum conditions and with the FBI-G1 molecules embedded on a substrate. However, for the final application, this silica pellets can not be used. First because of its low fabrication ineffectiveness (the reproducibility of the pellet fabrication was poor).Second because the silica pellet themselves also trapped Ba^{2+}ions (although it does not produce any fluorescence). Finally because, in order to aim for the highest sensitivity, the fluorophore distribution must be highly homogeneous and the molecules cannot be buried in the bulk of the substrate. In order to overcome these issues, the next step was the deposition of FBI molecules on flat surfaces.

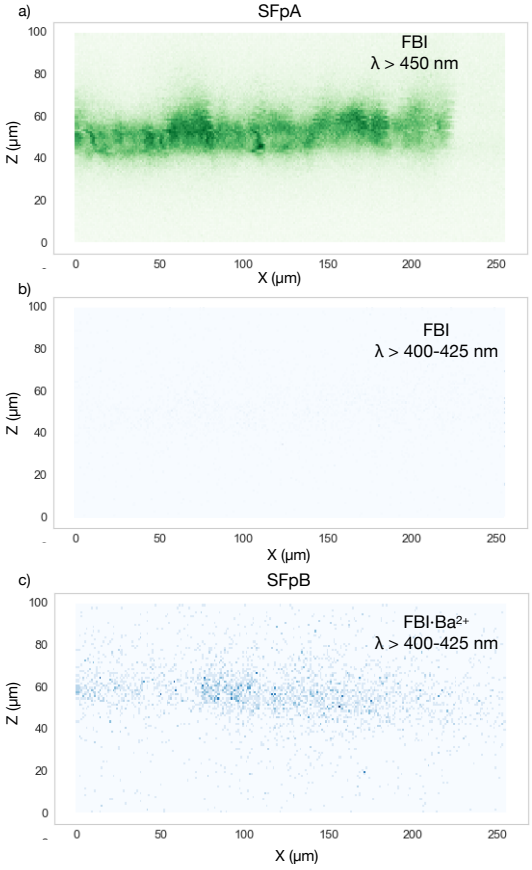

Figure 4.9. 2PA tomographies of FBI-silica pellets. (a,b) Reference SFpA pellet, with unchelated FBI filtered for green ($\gamma > 450$ nm) (a) and blue ($\gamma = 420 \pm 10$ nm) (b) emission. (c) FBI-G1 chelated with Ba^{2+} deposited with ALI (sample SFpB) filter ed for blue emission.

4.5 FBI-G1 depositions on Cu policrystal and XPS characterization

In order to deposit by ALI the FBI-G1 molecule two solutions in acetonitrile were prepared with a concentration of 1×10^{-4} M. The molecules were injected onto a clean copper policrystal with an argon backing pressure of 1 bar and an opening time of 50 ms for the pulse valve. From a total of 869 pulses, 305 were classified as wet and 564 as

Experiment	C/N	C/O	O/N
ALI, MetOH	9.6	5.1	1.9
ALI, AcN	6.5	5.1	1.9
Reference Stoichiometry	10.3	6.2	1.7

Table 4.3. Stoichiometries obtained by XPS analysis of FBI-G1 experiments deposited with different techniques.

dry pulses.

In order to analyze the deposition we use X-ray Photoelectron Spectroscopy (XPS), a highly sensitive UHV technique that provides information about the chemical composition, electronic state, and bonding of a material. XPS operates by irradiating a sample with X-rays, which causes electrons to be emitted from the surface. The energies of the emitted photoelectrons give information about the chemical composition of the surface. In the case of deposited molecules, the detection of core levels associated with the molecule is a fingerprint of the presence of the molecule on the surface. Thus, in our experiments with FBI-G1 (molecular formula $C_{31}N_3O_5H_{35}$) the detection of carbon, nitrogen and oxygen peaks will be a first indicator that the molecule has been correctly deposited. The Cu surface was cleaned by sputtering and annealing inside the UHV chamber prior to the ALI deposition.

Figure 4.10 shows the O 1*s*, N 1*s* and C 1*s* core levels of the samples after exposed to ALI deposition.

In the Figure 4.10 the spectra for two runs of ALI injections on a copper substrate with two different solvents are shown: acetonitrile (AcN) and methanol (metOH). The intensities of all peaks was normalized to the Cu 2*p* peak. The ratios between elements intensities, derived from the areas of these peaks, are shown in Table 4.3. The values for both experiments are in good agreement with the expected ratios from the molecular composition (last row). Deviations from the reference values can be attributed to small base presence of C and O on the Cu substrate. The largest deviations involve the nitrogen in the ALI sample prepared with AcN. This is a signal of passivation of the surface with AcN.

The three molecular core levels (O 1*s*, N 1*s* and C 1*s*) of the ALI-prepared samples (green, orange lines) present similar shapes to each

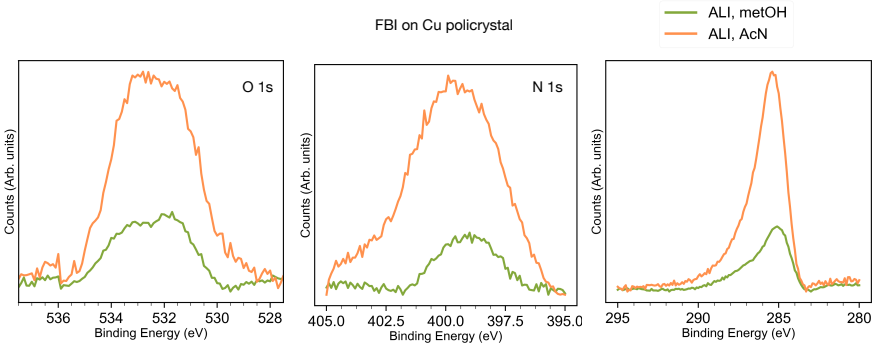

Figure 4.10. XPS of FBI on Cu and ALI injections (400 pulses in methanol, green and 400 pulses in acetonitrile, yellow). Spectra recorded in the molecular regions: O 1*s*, N 1*s* and C 1*s*.

other and different intensities. This implies that the injection of FBIs with acetonitrile solvent is more efficient that with methanol.

In the O 1*s* peak, there should be only one component centered on 533.5 eV, associated to the O in the crown ether. However, there is another component at lowe B.E., centered on 531.5 eV, associated to formation of Cu_2O [92]. This latter component, absent after cleaning the Cu substrate, indicates that during the deposition process of the oxygen in the solvent (mainly the OH group of the MetOH), or the fragments or impurities associated to the molecular synthesis oxidize the Cu substrate (the molecules were introduce without any pre-purification treatment).

The N 1*s* peak of the metOH sample has two components of similar intensities at 400 eV and 398.5 eV, respectively. The N 1*s* peak of the AcN sample is the most intense and contains three components at 400.1, 398.2 eV and 402.2 eV in order from most to least intense. The AcN sample has a larger N 1*s* peak than any other sample, which is reflected in an excess in the stoichiometric abundance of N for this sample compared to the rest. This excess hints the presence of the solvent itself on the surface, which contains nitrogen. The C 1*s* peaks contain a very intense peak at 286.7 eV and a faint one at 285 eV. The presence of excess C in ALI samples can be attribute to the presence of solvent and other impurities coming from the injection process.

The coverage estimation for the AcN and metOH samples is 1.4

and 0.6 ML, respectively. These coverages correspond to 1.4×10^{14} and 6×10^{13} molecules/cm^2, respectively. The leak rate estimation method yields a total number of 4.9×10^{14} molecules/cm^2 arriving to the substrate for the AcN experiment and 5.5×10^{14} molecules/cm^2 for the metOH experiment. This calculation then only overestimated the amount of deposited molecules by a factor 5 to 9. The procedure for the estimation was the same as in sections 4.3 and 4.4. Since the size of the Cu substrate was similar to that of the silica pellet, (2 cm diameter), the same collection efficiency $\varepsilon = 0.026$ was assumed.

4.6 Conclusions

The performance of the ALI technique was assessed in this chapter. It allows to inject pulses of molecular solutions into vacuum with high reproducibility and the amount of injected molecules can be estimated from the pressure profiles. In addition, the technique allowed to deposit $Ba(ClO_4)_2$ onto silica pellets containing FBI-G1 and chelate the indicators efficiently in UHV conditions, as demonstrated by 2PA microscopy. Lastly, the system can be used to deposit FBI-G1 directly on flat surfaces like Cu. The stoichiometry of the molecule is preserved, although some residue acetonitrile was found on the samples.

Moreover, the development of the ALI technique goes beyond the scope of barium tagging. An interesting application of injecting liquids into vacuum is the deposition of large molecules which would break when attempting to sublimate them. This was the case of starphene, a 2D polyaromatic hydrocarbon with three acene arms connected through a single benzene ring [93]. Since sublimation was not possible for these molecule, a precursor containing a carbonilated ring in each arm was used instead. The precursor was diluted in acetonitrile and injected onto an Au (111) surface in UHV using ALI. The injection consisted of 12 pulses of 50 ms at a backing pressure of 1 bar Ar. The sample was post-annealed to 150 ºC for 5 minutes to remove contaminants from the surface. This procedure allows to observe by STM individual starphene-shaped molecules on Au(111) [93], see Fig. A1.6 b,c. This is an example of on-surface synthesis which was possible to carry out thanks to the ALI technique. As the method is develop, more applications are expected to appear.

5 *On-surface* Ba^{2+} *trapping by first generation of FBI*

The FBI indicators introduced in chapter 3 could be the building bricks of a Barium-tagging device capable to eliminate all reducible background in NEXT. We have seen that the shift of the emission spectrum upon chelation with Ba^{2+} can be exploited to filter the signal of chelated indicators and distinguish them from unchelated ones. In addition, the proof-of-concept experiment described in chapter 4 demonstrated the capability of FBIs to trap Ba^{2+} when pressed into a silica pellet. However, the conditions to confirm chelation in the absence of air or solvent were still not probed. Thus, even though the trapping of the Ba^{2+} ions is occurring, the effect of solvents, air humidity or molecular aggregation in the fluorescence emission properties was not ruled out.

Furthermore, the silica pellet cannot be the substrate of choice for the definitive sensor. As discussed in 2.5, the indicators in the final design must be orderly arranged in a monolayer to assure univocal detection of a single Ba^{2+} ion. Pressing the molecules into a silica pellet does not yield a monolayer regime.

We address these issues in the present chapter. We demonstrate the chelation of FBIs with Ba^{2+} entirely in UHV. This rules out any possible influence of solvents, air molecules or spurious contaminants. To this end, we combine two highly sensitive surface techniques: X-ray Photoemission Spectroscopy (XPS) and Scanning Tunnelling Microscopy and Spectroscopy (STM/STS), to prove how different ions interact with FBI molecules deposited on suitable substrates.

5.1 Chelation on Silica pellets

After the demonstration that FBI molecules can chelate Ba^{2+} by depositing $Ba(ClO_4)_2$ with ALI, an important step towards the detection of Ba^{2+} in an HPXe is the demonstration that the ions can be chelated in the absence of solvent. This requires exposing a sample of FBI molecules to a source of Ba^{2+} ions.

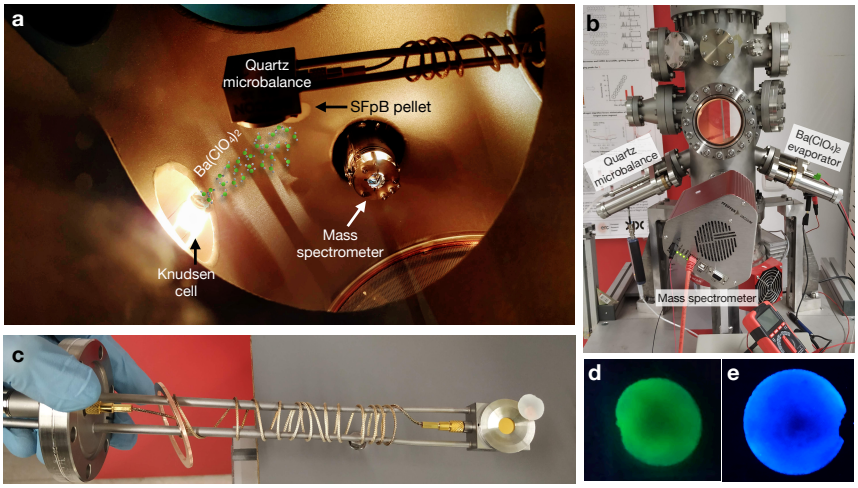

Figure 5.1. Sublimation of $Ba(ClO_4)_2$ **on the FBI**. **a**, Experimental setup. Photograph of the interior of the UHV chamber used for sublimation. The positions of the pellet, evaporator, quartz microbalance and mass spectrometer are indicated. **b**, General (exterior) view of the sublimation UHV chamber. **c**, Photograph of the quartz microbalance with SFpB pellet attached before being inserted in the UHV chamber. **d, e**, Photographs of the pellet before (**d**) and after (**e**) the sublimation. In both cases, the excitation light is 365 nm. We note the characteristic green colour of unchelated FBI before the sublimation and the blue shift after the sublimation, which shows a large density of chelated molecules.

As a starting point we designed a sublimation experiment as follows. We introduce one of the silica pellets containing FBI-G1 molecules (Fig. 3.3), as we did for the ALI deposition, in a UHV chamber (Fig. 5.1a, b). In there, barium perchlorate was sublimated using a Knudsen cell at a temperature of around 700 K. The evaporation rate was continuously monitored *in-situ* with a microbalance. The pel-

lets were attached to the microbalance during the exposure to barium perchlorate, as shown in Fig. 5.1c. The total thickness of deposited $Ba(ClO_4)_2$ was 10 Å, equivalent to a layer of 7.6×10^{14} molecules.

Figures 5.1d, e show images of the pellet before and after sublimation under an excitation light of 365 nm. The blue shift after sublimation is clearly visible even to the naked eye, showing that a large number of indicators on the pellet's surface were chelated. As we did for the chelation by ALI deposition, the sample was measured by 2PA microscopy [94] (see section A2.1). The results, summarized in Fig. 5.2, are similar to those obtained for chelation after ALI deposition of $Ba(ClO_4)_2$. On the $Z - X$ tomography on the unchelated-FBI pellet the region of about 20 μm where FBI molecules were immobilized is visible for the green filter (Fig. 5.2c) but not for the blue one (Fig. 5.2b). By contrast the deep-blue tomography (Fig. 5.2d) shows emission points from chelated molecules in the sample exposed to $Ba(ClO_4)_2$. Therefore, this demonstrates that the sublimation deposited the Ba^{2+} uniformly, resulting in a layer of chelated molecules. Finally, Fig. 5.2f shows green and deep-blue 3D tomography images confirming that the spatial distribution of the chelated molecules follows that of the unchelated indicators.

5.1.1 *Sensitivity to single chelated molecule in a dense monolayer*

In order to distinguish the signal of a single complexed indicator from the background of unchelated surrounding molecules a discrimination factor is calculated. Following ref. [95], we take the overall light collection efficiency of the system to be $\varepsilon_c = 10\%$. We consider a 2PA microscopy system similar to the one used here, but with optimized parameters, for example, an 800-nm pulsed laser, with a repetition rate of $f = 100$ MHz, pulse width $\tau = 100$ fs full-width at half-maximum and a moderately large numerical aperture of NA = 0.95. Focusing the laser on a diffraction-limited spot (a circle of $\sim 0.5\mu$ diameter) results in a photon density of 1.7×10^{31} photons cm^{-2} W^{-2} per pulse. We assume that one single FBI molecule complexed with a Ba^{2+} ion and m unchelated indicators are contained in such a diffraction-limited spot. The number of absorbed photons, n_a, per fluorophore and per

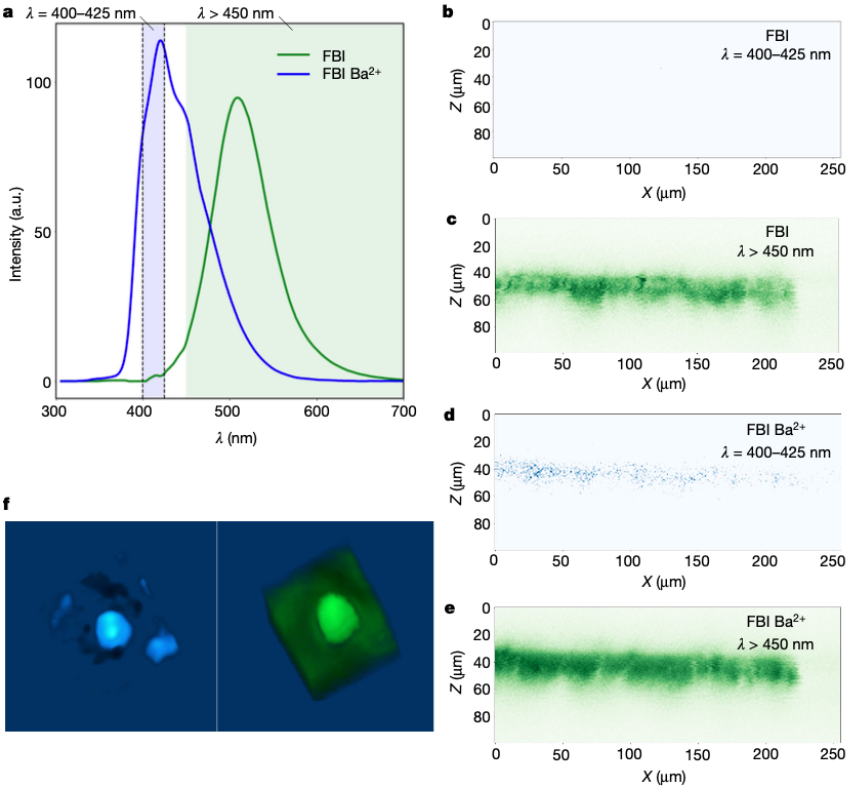

Figure 5.2. Response of the FBI. **a**, Emission spectrum of the SF (green line) and SBF (blue line) samples after silica subtraction (the SF spectrum is scaled by a factor of C_r with respect to the SBF spectrum). **b**, $Z - X$ profile of the control pellet, SFpA, showing no signal in the deep-blue region (400, 425) nm, where the contribution from unchelated molecules is negligible. **c**, $Z - X$ profile of SFpA in the green region ($\lambda > 450$ nm), showing intense green emission from the unchelated molecules. **d**, $Z - X$ profile of the sublimated pellet, SFpB, showing a clear signal in the deep-blue region (400, 425) nm due to the molecules chelated by the barium perchlorate. **e**, $Z - X$ profile of SFpB in the green region ($\lambda > 450$ nm), showing intense green emission from both chelated and unchelated molecules. **f**, 3D tomography images of SFpB, obtained with our 2PA microscopy setup, passed through the blue and the green filters. The images reveal the shape of a tiny section (a square of 75 μm^2 size), showing the same landscape for both chelated and unchelated molecules.

pulse is [96]:

$$n_a = \frac{P^2 \delta}{\tau f} \left(\frac{\mathrm{NA}^2}{2\hbar c \lambda} \right)^2, \tag{5.1}$$

where P is the laser power, δ is the brightness ($\sigma\phi_\lambda$) of the fluorophore, $\hbar$ is the reduced Planck constant and c is the speed of light in vacuum. We can compute the number of photons that the chelated indicator absorbs as a function of the laser power using equation 5.1. Given the relatively large 2PA cross-section of the FBI (also computed here), n_a = 2 for a modest power of 11 mW. By setting the laser power at this value, the emission rate of the chelated molecule will equal the laser repetition rate, $n_f = 1 \times 10^8$ photons s^{-1}.

The light emitted by the complexed FBI molecule will be blue-shifted. We assume that a band filter λ_f of (400, 425) nm is placed in front of the CCD. n is the fluorescence emitted in a given time interval by the f chelated indicator. Then, the light recorded by the CCD that is due to the chelated indicator will be $N = \varepsilon_f \varepsilon_c n_f$, where $\varepsilon_f \approx 0.29$ is the band-pass filter efficiency for the signal. The total fluorescence (green-shifted) emitted by the unchelated molecules will be mn_f/C, and the corresponding background light recorded by the CCD will be $N = \varepsilon' \varepsilon mn/C$, where $\varepsilon' \approx 0.0036$ is the band-pass filter efficiency for the background.

The total signal N_t recorded in the CCD will be $N_t = N_f + N_b$, where N_f is the fluorescent signal. The estimator of the signal observed in the spot will be $N_t - N_b$, where N_b can be computed with great precision by taking the average of a large number of spots containing only unchelated molecules. The signal-to-noise ratio (SNR) of the subtraction is:

$$\mathrm{SNR} = \frac{N_\mathrm{f}}{\sqrt{N_\mathrm{b}}} = \sqrt{\varepsilon_\mathrm{f} \varepsilon_\mathrm{c} \frac{n_\mathrm{f} F}{m}} = \sqrt{\frac{7.2 \times 10^{10}}{m}} \tag{5.2}$$

in units of $\mathrm{s}^{1/2}$. The SNR is expressed as a function of time in seconds because n_f measures the number of photons per second. The number of molecules in the diffraction spot will depend on the density of indicators, ρ, in the sensor. We assume that the target will be a dense monolayer with about one molecule per square nanometre. As shown by our DFT calculations, the 'snowballs' formed by the barium ion during transport (for example, Ba^{2+}–Xe_8, [54]) will readily

form a supra-molecular complex at distances of the order of 1 nm (for example, 8 Å in the example discussed here). Thus, $\rho = 10^6\ \mu m^{-2}$ and $m = 2 \times 10^5$. By substituting in equation 5.2, we find SNR = $6 \times 10^2\ s^{1/2}$. If we take a scanning time per spot of 1 ms, then SNR $\approx$ 20. Therefore, a chelated indicator would produce an unmistakable signal above the background of unchelated molecules in that spot. This demonstrates that fast and unambiguous identification of Ba^{2+} ions in the sensor can be attained using a dense monolayer.

5.2 FBI sublimation in vacuum

In order to characterize the ion trapping capability of the FBI molecules at molecular level, it was mandatory to deposit these FBI molecules on a surface by sublimation in UHV and characterize them structurally and chemically. Pure FBI molecules (in particular FBI-G1 in Fig. 3.3) were evaporated from homemade Knudsen cell evaporators. The molecules were used after degassing in UHV. The molecular evaporation rate was monitorized using a quartz microbalance. Afterwards, the amount of molecules on the surfaces was quantified by analyzing the relative intensity of the XPS core level peaks and the percentage of covered surface in STM. FBI evaporation was very stable and very reproducible, since the same rate for the same sublimation temperature was monitored. This reproducibility rules out fragmentation inside the evaporation cell. In the opposite case, if the molecules broke during the evaporation process, then the evaporation fragments would sublimate at different sublimation temperatures, and the evaporation would became non-reproducible. The simpler FBI derivative molecules (without crown ether) sublimate at 60-80°C while the intact FBI molecule sublimates at 140-150°C.

As substrate, we chose gold, the Au(111) face (single crystal cut to present (111) close-packed planes parallel to the surface), because it is a well known noble metal surface where very low substrate-molecule interaction was expected. We used XPS to determine their chemical composition. Since XPS sensitivity is limited to a depth of a few nanometers, molecular coverages below 1 monolayer (ML) were always used in this study. This ensures access to the substrate core levels for calibration.

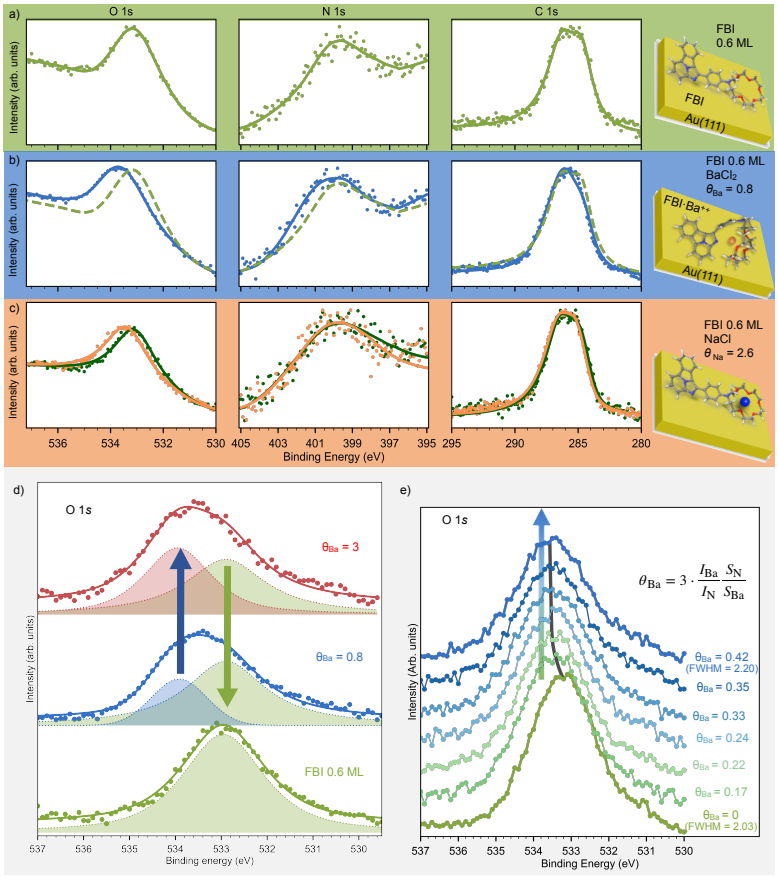

Figure 5.3. (a) O 1*s*, N 1*s* and C 1*s* core level spectra measured after sublimation of 0.6 ML of FBI deposition on Au(111); (b) FBI core level spectra measured on the previous sample after chelation with 0.80 Ba^{2+} ions per FBI molecule; (c) O 1*s*, N 1*s* and C 1*s* core level spectra measured after 0.6 ML of FBI deposited on Au(111) (green spectra) and after chelation Na^{+} (2.60 Na^{+} ions per FBI molecule) (orange line). For the three panels, dots correspond to raw values and solid lines to fitted curves. (d) Curve-component deconvolution of O 1*s* spectra in (a) and (b) as well as after chelation with $\theta_{Ba} = 3$. (e) Evolution of the O 1*s* core level as a function of the Ba^{2+} deposition on 0.9 ML of FBI on Au(111). The spectra were manually shifted in the y-axis to better show the evolution. The O 1*s* spectra in (d) and (e) are displayed after subtraction of the contribution from Au 4*p* 3/2, in order to emphasize the spectral changes.

Figure 5.3a shows the XPS spectra of the three molecular core levels of FBI, i.e. O 1*s*, N 1*s* and C 1*s*. The spectra were measured for 0.6 ML of FBI deposited on Au(111) at room temperature (RT). The evaporation thicknesses were estimated using the attenuation of the most intense substrate core levels, i.e. Au $4f$. The calculations followed the guidelines provided in ref. [97]. For this purpose, we estimated the electron Effective Attenuation Length (EAL) through the FBI layers for electrons with kinetic energies of 1402.6 eV (Au $4f$ for Al Kα radiation). The resulting EAL is 3.87 nm respectively. The thickness of the FBI samples was then estimated using the intensity of clean substrate core level as reference and the attenuated intensity after the evaporation. To correct for systematic uncertainties affecting different sets of data, the intensities of all spectra were rescaled to the Au $4f$ core level.

The C 1*s* core level can be fitted using two components, one centered at around 284.7 eV and a second and more intense one at 286.3 eV. The former component corresponds to C-C bonds whereas the component at higher binding energy (BE) includes contributions from C-O and C-N bonds, with their relative intensities in agreement with having intact molecules. In the N 1*s* region, around 400.4 eV, a faint peak is visible. The position of the maximum is compatible with the enamine-imine groups of the molecular composition. Finally, the O 1*s* core level presents a single component peak centered at around 533.0 eV, which is compatible with previous reports on closely related crown ether groups [98]. The ratios between the core levels, C/O = 6.2, C/N = 10.3, are in agreement with having molecules of $C_{31}N_3O_5H_{35}$ stoichiometry on the surface (FBI molecule stoichiometry). The core level peak areas were numerically integrated between fixed local minima. This yields an error in the stoichiometry ratios of 7%. The stoichiometry ratios were calculated following the expression $R(A/B) = (I_A/I_B \cdot S_B/S_A)$ where A and B are the different molecular elements, I_X is the integrated area under the main core level and S_X is the corresponding sensitivity factor of this core level.

In addition to the XPS analysis, we have confirmed the intact sublimation of the molecules by STM. The experiments were performed in two different UHV chambers, one for XPS experiments and the other for STM experiments. Both chambers have a base pressure of 1×10^{-10} mbar. To ensure sublimation reproducibility, each molecular evapora-

tor cell (containing the FBI) was removed from the XPS chamber and installed in the STM chamber.

Deposition of a submonolayer of FBI mostly leads in disordered islands coexisting with isolated molecules (Figure 5.4a). The lack of chemical order on the islands makes it difficult to identify specific molecules, and interpretation depends on the viewer. However, it is feasible to spot characteristics that mirror the features of such molecules (some examples are illustrated in Fig. 5.5). With this, molecular fragmentation at the surface or in the evaporation process is ruled out. STM images of single molecules (inset in Figure 5.4a) are identified by two main triangular-like lobes. Based on the molecular structure, one of them should correspond to the fluorophore and the other to the crown ether moiety bonded to the phenyl ring. The apparent height of both is different, with one of them appearing lower and flatter than the other.

In order to correlate the apparent molecular shape and the molecular structure, bond-resolved STM images were taken. For that, the STM tip was functionalized with CO molecules operating in the repulsive tip-sample interaction regime, a method extensively used for characterizing planar organic molecules [99, 100]. Application of this measurement mode to the FBI molecule results in the images displayed in Figure 5.4b. For eye guidance, the STM image has been shown twice, one with and one without the superimposed molecular model. An internal bonding structure close to the fluorophore structure is resolved on the left region of the molecule, while the aza-crown ether region is not well resolved. Due to its larger conformational flexibility and its non-planarity, tip stability is not good enough and, as a consequence, the contrast observed in the aza-crown ether part is an artefact related to excessively strong interactions with the flexible CO tip-apex. [101, 102]. To confirm the imaging signature of the fluorophore, we also sublimated two FBI derivatives specifically synthesized without the aza-crown ether component. Figures 5.4c and d show the bond-resolving images of FBI derivatives sublimated on Au(111) surface: the fluorophore (Figure 5.4c) and the fluorophore with the phenyl ring but without the aza-crown ether (Figure 5.4d). The absence of the aza-crown ether allowed the molecules on the surface to adopt a planar, rigid conformation, which clearly improves the image acquisition, with the carbon framework of the fluorophore well visualised. It is

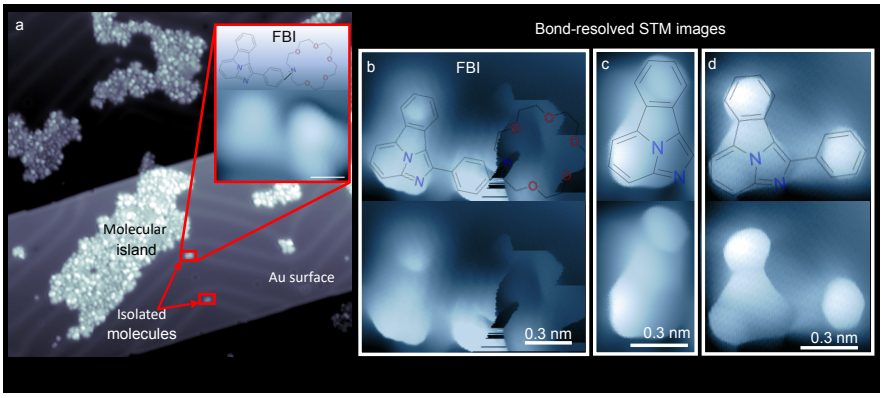

Figure 5.4. (a) Large scale STM image (50×50 nm^2) of around 0.4 ML of FBI molecules deposited on Au(111) surface and measured at 4 K. Red squares show isolated molecules. Inset: constant current zoom STM image of a FBI molecule (I = 60 pA / U = 1.4 V) deposited on Au(111). (b-d) Bond-resolved STM image measured with a CO-functionalized probe (constant height, U = 5 mV) of individual FBI molecules: (b) benzo[*a*]imidazo[5,1,2-*cd*]indolizine fluorophore with phenyl ring and aza-crown ether (exactly the same molecule shown in the inset in (a)); (c) benzo[*a*]imidazo[5,1,2-*cd*]indolizine fluorophore; (d) benzo[*a*]imidazo[5,1,2-*cd*]indolizine fluorophore with phenyl ring but without the crown ether. For clarity, the same image is shown twice, one with and one without the molecular model superimposed to guide the eyes.

remarkable that none of these FBI derivatives forms molecular islands. Instead, only dimers or molecular tetrameters are distinguished in the STM images. This supports the previous assessment, that FBI molecules remain intact (non fragmented) after sublimation.

5.3 Chemical demonstration of chelation

Once the presence of intact FBI molecule on the surface was confirmed, $BaCl_2$ was sublimated to test the molecular chelation. $BaCl_2$ powder was evaporated from a homemade Knudsen cell evaporators. To avoid cross-talking between FBI and the salt molecules and to exclude any possibility of chelation of the molecule inside the cell, the FBI and $BaCl_2$evaporators were located in two separated parts of the UHV chambers. Prior to the sublimation on the FBI, $BaCl_2$ was sublimated on clean Au(111) surface to confirm its stoichiometry. By comparing

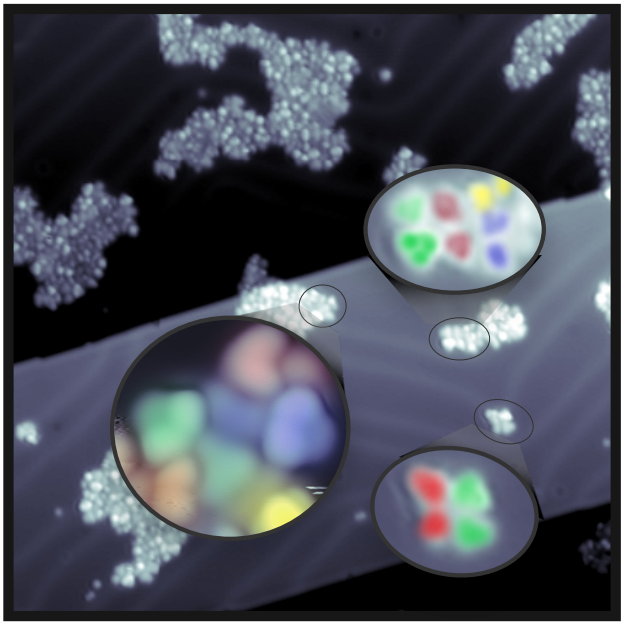

Figure 5.5. Several molecular aggregates have been highlighted in the large scale image shown in Figure 5.4. As a guess of the molecules inside the aggregates, we use fictitious colors (each molecule corresponds to a colour). This implies that no molecular fragments are evaporated in addition to the intact molecules. This is also supported by the fact that the XPS stoichiometries remained constant over the course of the several (over 10) evaporations performed for this study.

the core level intensities of Ba $3d_{5/2}$ and Cl $2p$ core levels (taking into account the corresponding sensitivity factor of each element), the ratio Ba:Cl was 1:2 as expected. Surprisingly, when $BaCl_2$ was deposited on FBI-functionalized Au(111), this ratio changes, being around 1:1.5$\pm$0.2, meaning that there is a partial desorption of chlorine atoms when $BaCl_2$ reached the sample.

From the simulations we have performed on the way that $BaCl_2$ interacts with the FBI molecule (see details of the calculations in subsection 5.4) we conclude that the chloride atoms behave as passive spectators in the chelation. When the FBI molecule is chelated with $BaCl_2$ salt, the coordination pattern ($N\cdots Ba^{2+}$, $Ph\cdots Ba^{2+}$ and crown

ether$\cdots Ba^{2+}$) is the same as the one calculated in Ref. [75] and the Cl atoms play no role (see Fig. 5.8). As a result, when the $BaCl_2$ molecules are placed on the FBI functionalizes surface, the $BaCl_2$ molecules split, releasing Cl atoms. The fluctuations in the Ba:Cl ratio are due to partial desorption of Cl atoms from the surface. In any case, the Ba 3*d* core level does not show any significant shift when comparing the sublimation of $BaCl_2$ on bare or functionalized gold surface (as shown in Fig. 5.7), suggesting that there is no change in the Barium chemical oxidation state [103]. Because of this lack of stoichiometry, we refrain from using $BaCl_2$ ML to refer to the amount of sublimated molecules and, instead, we will refer to the Ba^{2+} ions per FBI molecule. The amount of Ba^{2+}(Na^+) per FBI molecule were estimated by computing the ratio $\theta = I_{Ba}/(I_N/3) \cdot S_N/S_{Ba}$, where I_{Ba}, I_N are total areas of Ba $3d_{5/2}$ and N 1*s* core levels respectively, and $S_{Ba} = 25.84$, $S_N = 1.80$ are the corresponding atomic sensitivity factors [104]. The factor 3 responds to stoichiometric reasons, considering 3 N atoms per molecule.

After sublimation of 0.80 Ba^{2+} per FBI molecule (Figure 5.3b) the molecular core levels slightly shift. Even though the three core levels slightly shifted toward higher binding energies, the magnitude of each shift is different, being the highest for O 1*s* (upward shift of 0.5 eV). Since each shift is different in size, there must be a chemical change and not charge doping (associated to non reacted ions), which would show a rigid shift of all core levels. According to the O 1*s* core level curve fitting, the peak width grows and a new component has to be introduced at a higher BE position, as shown in figures 5.3d and 5.6. The new component, added to the non-chelated FBI component at 532.95 eV, is centered at around 533.9 eV, position consistent with O-Ba interaction (chelated crown ether)[98]. This new component remains unshifted even for θ_{Ba} above one Ba^{2+} ion per FBI molecule, as can be seen in Figure 5.3c, where the θ_{Ba} was increased up to 3 Ba^{2+} per FBI molecule.

Figure 5.3e shows the evolution of the O 1*s* for incremental amounts of Ba^{2+} ions, from 0 to almost 0.5 Ba^{2+} ions per FBI molecule, on 0.9ML of FBI on Au(111). There is a monotonous shift toward higher binding energies of the maximum of the spectra. Once $BaCl_2$ is added to the sample, the O 1*s* peak width increments by 9% FWHM and, again, a new component at around 533.9 eV is necessary to properly fit the core level spectrum. This new component remains constant in energy,

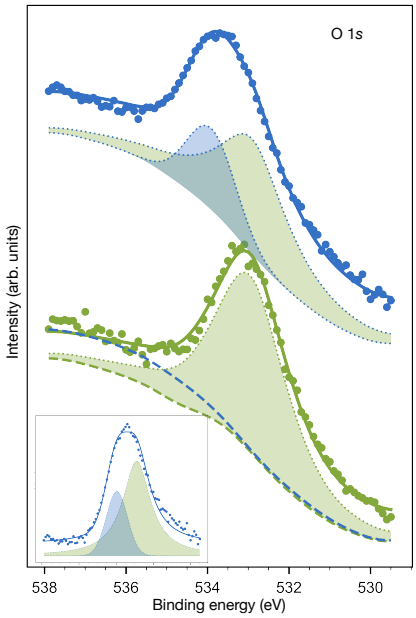

Figure 5.6. Detail of fitting components (dotted lines) for O 1*s* in FBI 0.6 ML (green) and FBI 0.6 ML + $BaCl_2$, θ = 0.8 (blue) from Figure 5.3 (a) and (b). Circles and solid lines represent raw data and best fit respectively. The green component was fitted to the unchelated FBI data (green circles) at 532.95 $\pm$ 0.05 eV, with width 2.16 $\pm$ 0.04 eV at FWHM. This component was then fixed in position and width for the chelated FBI data (blue dots). An additional component was fitted to the chelated FBI CL, shown as blue filled area, at 533.91 $\pm$ 0.05 eV, with 1.41 $\pm$ 0.05. These values were obtained from the fit as free parameters. The background of each curve is shown as dashed lines in green and blue respectively. Inset: same blue curve and components with its background subtracted.

and only its intensity changes (the fit is included in Fig. 5.7). However, quantification is complicated because of the close proximity of the right tail of the Au $4p_{3/2}$ core level (as shown in Fig. 5.7). The O 1*s* spectra shown in Figure 5.3d and e were plotted after subtracting the contribution of the Au $4p_{3/2}$ core level in order to emphasize the spectral changes.

The spectra fitting was performed using custom-made software written in Python and the lmfit library [105]. An example of fit can be

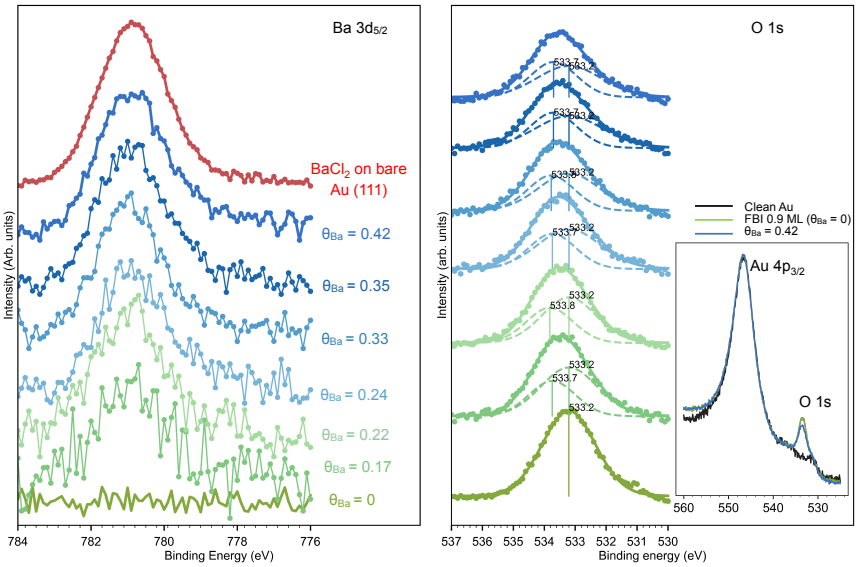

Figure 5.7. O 1*s* (right) and Ba $3d_{5/2}$ (left) core levels evolution measured for FBI on Au(111) with subsequent evaporation of $BaCl_2$ (data on Fig. 2e). The Ba $3d_{5/2}$ core level is always centered on 780.9 eV. The spectrum of $BaCl_2$ directly deposited on bare Au(111) also appears centered on 780.8 eV where the Ba is in the +2 oxidation state. Inserted is the Spectral region around the Au $4p_{3/2}$ and O 1*s* core levels. Spectra corresponds to clean Au (111), 0.9ML of FBI, FBI after chelation with 0.42 Ba^{2+} ions per molecule.

seen in Figure 5.6. The core levels were modeled as a pseudo-Voigt function (Lorentzian to Gaussian ratio of 0.6) convoluted with a Shirley type background. The error in the estimation of the position of the maxima derived from fitting is 50 meV. However we only consider as significant shifts higher than 100 meV, which is the energy step we use in the adquisition. The goodness of fit is given by a χ^2 parameter of about 0.05 counts (in A.U.) when the data are normalized to a maximum intensity of 1. Here $\chi^2 = \sum_i (y_i - Y_i)^2 / Y_i$, where y_i and Y_i are the data intensity values and the expected values from the fit respectively.

It is important to note at this point that, even when the number of Ba ions per molecule permitted it, we never observed a complete chelation of the FBI. It is challenging to determine whether this is

due to ineffective chelation or to the experimental setup, as the latter certainly limits it. To demonstrate the Ba^{2+} trapping by FBI molecule the XPS experiment needs a coverage below or close to the monolayer to avoid interference from molecular stacking (FBI molecules forming multilayer structures). Under these conditions, sublimated $BaCl_2$ can still form islands on bare gold regions (as we have seen in the STM images). This can prevent them from participating in the chelation process.

To evaluate whether the nature of the ions has any influence on the oxygen core level shift for the FBI molecules, we tested the chelation with Na^+ . We selected this ion because it was also the choice of the only prior study in which crown ether was chelated on surfaces [98]. Figure 5.3c shows the O 1*s*, N 1*s* and C 1*s* core levels measured on 0.6 ML of FBI on Au(111) before and after the sublimation of $\theta_{Na} = 2.60$ per FBI (θ_{Na} is computed analogously to θ_{Ba}). The maximum of the O 1*s* core level shifts again for Na^+ -chelated FBI molecules 0.5 eV toward higher BE, while there is no apparent shift on the N 1*s* (nor C 1*s*) core level. This results reveals that N 1*s* is not as involved in the ion trapping as before. This difference between Ba^{2+}- and Na^+ -chelation can be interpreted as a first proof that the molecular conformation of FBI and the cation-phenyl interaction varies depending on the nature of the trapped ions. This result agrees the theoretical calculations, where almost no FBI distortion is predicted upon chelation with Na^+ as it is discussed next.

5.4 DFT calculations of most stable conformation of FBI-G1 upon chelation

As discussed in Chapter 3 section 3.3.1, calculations demonstrated that the most stable configuration was that where the Ba^{2+} ions ended in the presenting coordination bonds with N, phenyl ring and O atoms. Based on them, we compute the chelation of the FBI with $BaCl_2$. As starting point we located the $BaCl_2$ on top (forming a concave complex) the crown-ether ring and we leaved the system to evolve to the most stable configuration. As it can be seen in Figure 5.8a, the final geometry resembles that calculated before, meaning that conformation is maintained regardless of the ion source (naked Ba^{2+} cation or $BaCl_2$

salt). The N$\cdots$$Ba^{2+}$, Ph$\cdots$$Ba^{2+}$ and crown ether$\cdots$$Ba^{2+}$ bonds are preserved on passing from naked Ba^{2+} cation to $BaCl_2$ salt. These geometries show a computed root-mean-square deviation value of RMSD = 2.83 Å, excluding the two chloride anions.

We have also computed another coordination pattern, forcing the Barium cation to interact with the sensor from the outside, namely through the convex face of the crown ether connected to the fluorophore. In this case, the Ba^{2+} ended interacting only with the crown ether forming a convex complex, as it is shown in Figure 5.8b. In this case, all the O$\cdots$$Ba^{2+}$ distances are very similar and lie in the 2.83 - 2.87 Å range. The only N$\cdots$$Ba^{2+}$ interaction exhibits a slightly larger distance of 3.13 Å. Therefore, this complex has a more restricted coordination pattern since both Ph$\cdots$$Ba^{2+}$ and N$\cdots$$Ba^{2+}$ are not available. Consequently, the convex complex is 7.4 kcal/mol (6.9 kcal/mol if Gibbs energies at 298 K are considered) less stable than the previously mentioned concave complex. This means that, thermodynamically, the latter should be ca. 3.0×10^5 more abundant than the latter. However, if the sensor is adsorbed on the surface and the concave face is kinetically less accessible, perhaps the formation of a minor amount of the convex complex cannot be completely ruled out, although even in this rare event the metastable convex complex should evolve towards the thermodynamically more stable concave one.

Finally, we have also computed the situation were FBI is positioned on the periphery of the crown ether rather than close to the center. However, the most stable conformation is that in which Ba^{2+} is trapped in the concave part (fully optimized geometry shown in Fig. 5.8). The ions starting in a lateral position with respect to the crown ether find a metastable conformation with all the O-Ba^{2+} equidistant. These calculations rule out two possible causes of the O 1*s* core level shift: chelation of molecules at the edges of the $BaCl_2$ islands, and interactions between $BaCl_2$ (Ba^{2+}) and the periphery of the crown ether. Therefore, in terms of XPS, it seems reasonable to interpret the O 1*s* core level shift as a chelation fingerprint.

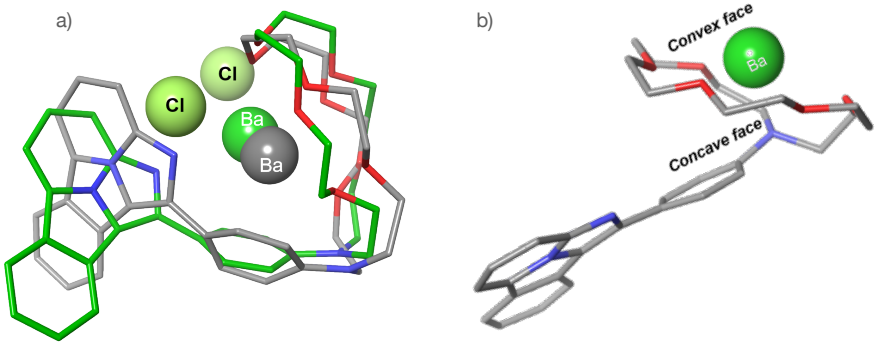

Figure 5.8. Graphical representations ofthe RMSD associated with fully optimized geometries (B3LYP-D3BJ/6-31G*&LANL2DZ level of theory) of: a) FBI molecule coordinated to a naked Ba^{2+} cation (gray) and to $BaCl_2$ (green); b) FBI molecule coordinated to a naked Ba^{2+} along the convex face of the crown ether. Hydrogen atoms are not shown.

5.5 Molecular structural rearrangement induced by chelation

In order to visualize the structural changes undergone by the FBI molecules upon chelation, STM experiments were carried out again. Figure 5.9a shows the schematic representation of the most stable conformation calculated for the molecules in gas phase before and after chelation with Na^+ and Ba^{2+} (corresponding to optimized structures in Fig. 5.10). In all cases the crown ether ring is out of the plane with respect to the fluorophore, and in the case of the Ba^{2+}-chelated molecule, this group is folded over the fluorophore. For molecules lying on a surface, we expect to have the fluorophore parallel to the substrate, and the crown ether region out of the plane, as corroborate the STM images (Figure 5.9b-d).

In the three images, the fluorophore and the aza-crown ether region are distinguished. In the case of Na^+ -chelated FBI identification is easier than for Ba^{2+}-chelated because image remains almost unchanged compared to the non-chelated FBI. FBI chelated with Ba^{2+} has a more complex shape. Interpretation of constant current mode

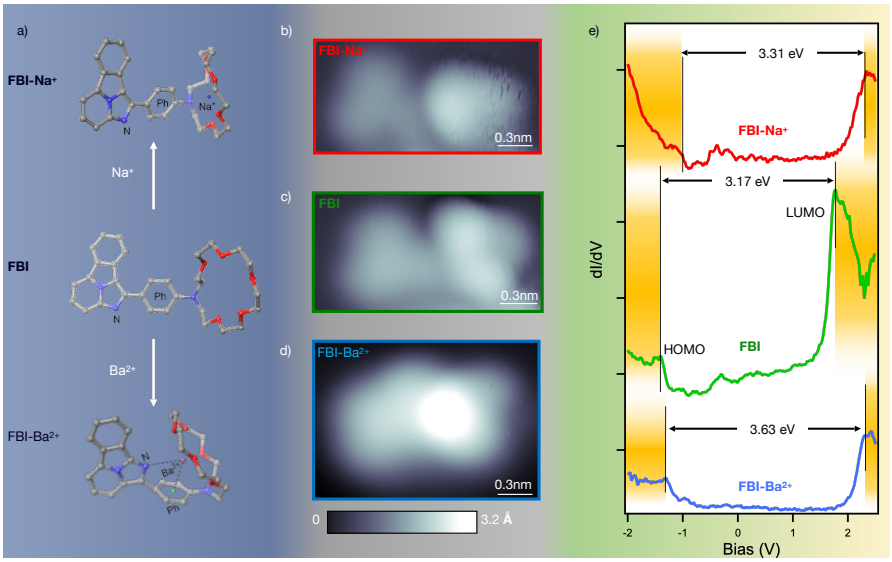

Figure 5.9. (a) Representation of the most stable conformation calculated for the molecules in gas phase. (b-d) STM images of (b) Na^+ -complexed (U = 0.9 V, I = 60 pA), (c) native (U = 1.4 V, I = 60 pA), and (d) Ba^{2+}-complexed (U = -0.5 V, I = 20 pA) FBI. (Scale bars = 0.3 nm) (e) STS spectra of native (green), Na^+ -complexed (red), and Ba^{2+}-complexed (blue)FBI.

STM images is always difficult because of the convolution of topographical and electronic contributions. To reduce as much as possible the influence of the latter, the images included in Figure 5.9b-d were measured using bias voltages inside the molecular gap. Taking into account that the three STM images are plotted with a common color code, it can be directly observed that the apparent heights of the crown ether follow the expected trend (higher for Ba^{2+}-chelated molecule). Indeed, the apparent height for each molecule, as measured on the highest point of the crown, is 2.5 $\pm$ 0.1 Å, 2.1 $\pm$ 0.1 Å, and 2.9 $\pm$ 0.1 Å, for the pristine FBI and the Na^+ - and Ba^{2+}-chelated molecules respectively. Thus, complexation of crown ethers with alkali metals like Na^+ causes the oxygen atoms to point to the center, forcing the ring to adopt a flatter conformation relative to the native molecule. Instead, the FBI molecule adopts a more three-dimensional conformation upon chelation with Ba^{2+}. It is worth mentioning that the aspect of these STM images resembles the electron density simulations associated

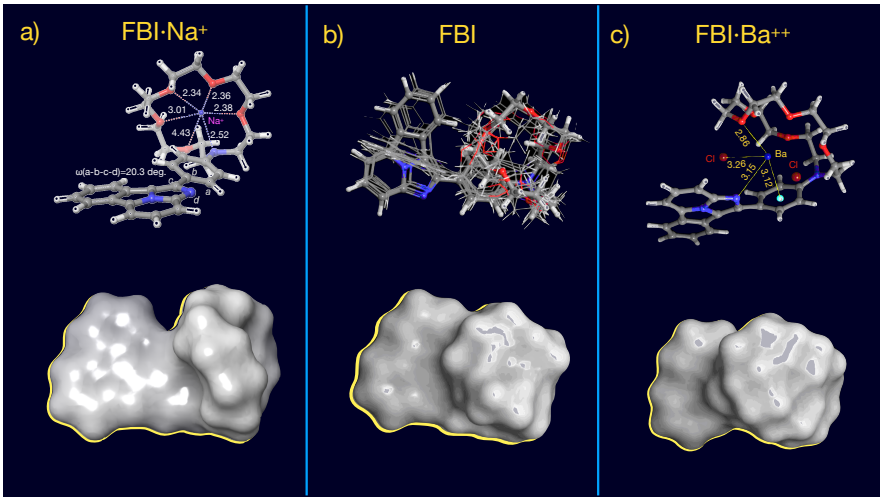

Figure 5.10. Fully optimized structure (top) and the electron density surface associated with the most stable conformer (bottom) for: a) FBI·Na^+ complex computed at the B3LYP-D3BJ/6-311++G(d,p)&LANL2DZ level of theory. The cation Na^+ interacts only with the crown-ether, which bends slightly. Since this cation is smaller than Ba^{2+}, it does not occupy all the coordination positions, i.e. it does not interact with the phenyl ring nor with the nitrogen from the fluorophore; b) MM– MC conformational analysis (OPLS3e force field) of FBI. The Ball & Stick representation corresponds to the most stable conformation. The other structures correspond to the ten most stable conformers within 0.0-4.8 kJ/mol; c) fully optimized structure of FBI·$BaCl_2$ complex computed at the B3LYP-D3BJ/6-311++G(d,p)&LANL2DZ level of theory. Bond distances are given in Å.

with the most stable conformers shown in Figure 5.9a (electron density simulations shown in Fig. 5.10). To establish a more quantitative relationship between apparent molecular structural modification and chelation, scanning tunneling spectroscopy (STS) measurements were performed.

STS permits to scan the local density of states and to visualize the orbitals around the Fermi level, i.e. the Lowest Unoccupied Molecular Orbital (LUMO) and the Highest Occupied Molecular Orbital (HOMO). Calculations done by DFT in Ref. [75] reveals that these frontier orbitals change their relative distances upon chelation (the HOMO-LUMO gap is higher for Ba^{2+}-chelated molecules than for

Species	Band gap / eV (nm)	λ^{abs}_{max} / nm	λ^{emi}_{max} /nm
FBI	3.17 (391.1)	432.5	489
FBI-Na^+	3.31 (374.6)	430	489
FBI-Ba^{2+}	3.63 (341.6)	420.5	428

Table 5.1. Band gap values measured by STS on Au(111) vs. absorption ($\tilde{}^{abs}_{max}$) and fluorescence emission ($\tilde{}^{emi}_{max}$) spectral peaks measured in solution [75].

native ones). Moreover, for both unchelated and Ba^{2+}-chelated FBI molecules, these orbitals are mainly located at the fluorophore region (the benzoimidazoindolizine group). This is an advantage because we can scan the local density of states on the fluorophore region by STS and correlate the spectral changes with the variation in the electronic structure of the whole molecule. Thus, figure 5.9e shows the associated STS measured for the three molecules of figure 5.9b-d in the fluorophore region. The FBI molecule deposited on Au(111) has a HOMO-LUMO gap of 3.17 eV. Complexation with Na^+ slightly changes this band gap, while complexation with Ba^{2+} increases it up to 3.63 eV.

The DFT calculations also show that the lowest fluorescence emission peak of the non-chelated FBI molecule mainly comes from the de-excitation of electrons from the LUMO to both HOMO and HOMO-1. For Ba^{2+}-chelated molecules, the torsion of the phenyl group decreases the effective π-conjugation and promotes the LUMO-HOMO transition over the LUMO-HOMO-1 as the lowest emission channel. By STS we observed a clear variation in the electronic gap upon chelation with Ba^{2+}: the LUMO-HOMO gap increases, which explains the blue shift fluorescence emission spectra measured in solution (Table 5.1).

For Na^+ , while there is a small variation of the electronic gap, the molecule remains planar. This planarity of the molecule after chelation does not modify the π-conjugation, which is still extended into the phenyl ring. Therefore, the LUMO-HOMO distance does not significantly change. However, this small shift seems to be in contradiction with the fluorescence measurements, where no shift was measured for Na^+ -chelated FBI molecules compared to unchelated FBI. While the magnitude of the HOMO-LUMO gap defines the maximum emission energy, the closely-spaced vibrational energy levels in the ground state

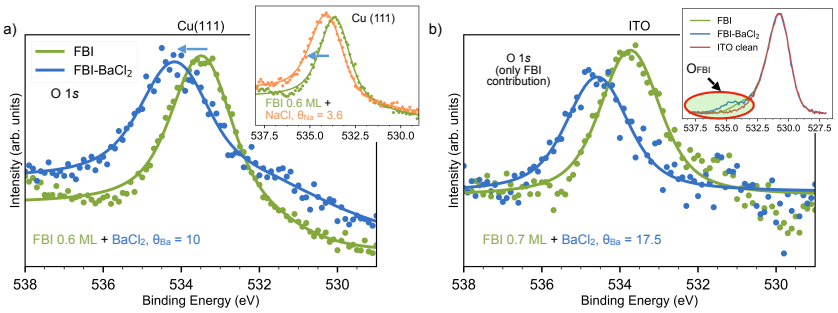

Figure 5.11. (a) chelation on Cu(111) sublimating $BaCl_2$ and NaCl (inset); (b) chelation on ITO. In this case, the substrate component (O_{ITO}) was subtracted to emphasize the O 1*s* contribution coming from FBI (O_{FBI}). The entire spectra are shown inserted in (b). Dot spectra correspond to raw values and solid lines to fitted curves.

result in a distribution of photon energies. As a result, fluorescence is normally observed as intensity over a band of wavelengths rather than a sharp line. Hence, the small gap modification we have measured by STS could produce a correspondingly small shift in the emission spectra. However, this shift would be undetectable because of the broadness of the spectra. Table 5.1 summarizes the absorption and fluorescence emission maxima λ^{emi}_{max} and λ^{abs}_{max} associated to the transition of electrons from HOMO to LUMO+n states (absorption), as well as from LUMO, to HOMO-n (fluorescence).Unfortunately, because of the metallic character of the substrate we cannot measure the fluorescence emission directly on gold (the excitation energy is dumped to the metal without further emission).

5.6 Chelation tested on different surface support

Finally, we have observed that chelation also takes place on other surfaces, in particular Cu(111) and Indium Tin Oxide (ITO). We chose Cu(111) because it is a more reactive substrate. This enabled us to study whether the molecule-substrate interaction could alter the chelation response. On the other hand, ITO was selected as a promising candidate for the potential implementation of a Barium tagging detector on a xenon-based TPC [75]. As degenerated semiconductor,

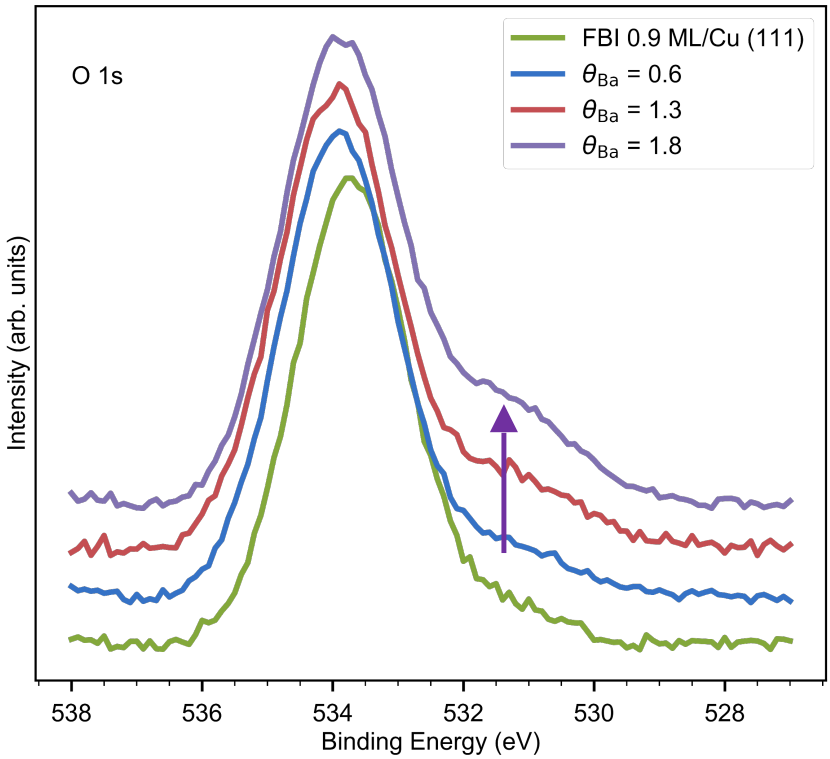

Figure 5.12. O 1*s* core level of FBI on Cu (111) (green) and FBI-$BaCl_2$ in different doses. The shift toward higher BE is still present for these concentrations of Ba^{2+} (blue arrow). The shoulder at low BE (531 eV) from Cu_2O contamination grows with the exposure to the evaporator (purple arrow). This is due to the higher concentration of oxygen in the evaporation module, which had a slightly higher pressure than the characterization module.

ITO is transparent, which would allow the direct detection of fluorescence in transmission. Furthermore, its conductivity is *high* enough to guide the Ba^{2+} ions towards the sensor surface, thus facilitating their capture by FBI. On the other hand, the conductivity of ITO may be potentially *low* enough to avoid the fluorescence quenching that is expected at conductive surfaces. Prior to molecular deposition, Cu(111) and Indium Tin Oxide (ITO) surfaces were cleaned via cycles of Ar sputtering and annealing to 500 °C and their cleanliness was checked

by XPS. The agreement between experiments performed on different substrates and subsequent preparations confirmed the reproducibility of the evaporation and chelation processes.

As previously discussed, we focus again on the O 1*s* core level to see whether the conclusions extracted before about its shift apply also on these surfaces and we can use it as a fingerprint of the chelation. Figure 5.11 shows the O 1*s* core level of FBI on Cu(111) and ITO. We used a Ba^{2+} dosing of $\theta_{Ba} = 10$ for 0.6 ML of FBI on Cu(111) and $\theta_{Ba} = 17.5$ for 0.7 ML of FBI on ITO. In both cases, we observed the chemical shift on the O 1*s* towards higher BE, indicating that chelation is happening. In the case of Cu(111), the shift is about 0.7 eV, while for ITO is around 0.9 eV. As far as ion capture is concerned, FBI chelation of Na^+ on Cu(111) was also tested with $\theta_{Na} = 3.6$. Again, O 1*s* shows an upwards shift associated with chelation (inset in Figure 5.11a). Fig. 5.12 shows O 1*s* shifts for low θ_{Ba} doses on Cu(111), with a similar shift evolution as the one observed on Au(111) for low θ_{Ba} doses (in Figure 5.3d).

Quantifying the exact values of the O 1*s* core level shift, and the chelation efficiency was not possible. Notice that in the case of Cu(111), when the FBI-functionalized surface is exposed to $BaCl_2$, the residual contamination partially oxidizes the surface. For this reason, the core level has a smaller component at lower BE, around 531 eV (see Fig. 5.12), associated to Cu_2O [92]. On the other hand, because of the presence of oxygen in the ITO structure, the analysis of the O 1*s* core level shifts required a subtraction of the core level measured on the bare ITO to highlight the FBI and Ba^{2+} chelated FBI contributions (O_{FBI}). The result of the subtraction is shown in Figure 5.11 b), and the inset gathers the original normalized spectra, including the contribution to the O 1*s* coming from the ITO (O_{ITO}).

These results ensure that chelation is independent from the choice of substrate, even though the values of the shifts are different for the three substrates. In photoemission, the absolute value of the core level shift depends on many factors such as the substrate, the molecular coverage, the presence of defects or other molecules. However, what is important here is that in the three cases the core level shifts in the same direction and with similar magnitude.

5.7 Conclusions

To summarize, by combination of highly sensitive surface science techniques, we have unraveled the chemical and conformational changes that occur upon chelation of FBI molecules. We started with Au(111), a well-known surface that served as model, and moved on toward more suitable surfaces. Furthermore, the changes are in agreement with the calculations for the behaviour of free standing molecules. Regarding the bicolor property of the sensor: fluorescence emission could not directly measured because of the metallic character of the substrates. Nonetheless, the measured variations in the molecular HOMO-LUMO gap are consistent with the observed emission shift for Ba^{2+}-chelated molecules. Moreover, they are also consistent with the absence of such shift, observed and predicted for other ions, such as Na^{+} .

The demonstration of chelation in vacuum of FBIs by Ba^{2+} ions are deposited on a surfaces in submonolayer regime is a major step towards the development of a sensor capable of single barium tagging. This sensor would have the immediate application in a new, ultra-low background xenon-based $0\nu\beta\beta$ detection experiment. Furthermore, this study has also important implications beyond the field of particle physics. Aza-crown ether groups have demonstrated to chelate alkali ions with high affinity in solution. Here we showed the capability of these molecules to trap big or small ions (Ba^{2+} or Na^{+}) on surfaces too. This could have important applications in drug carriers [106], photo-switching devices [107, 108] or different types of ion sensors.

We demonstrate that Ba^{2+} ions induce molecular conformation changes, modifying the electronic structure that would affect the fluorescence emission at suitable surfaces (see model in Figure **??**). In addition, the FBI molecules are arranged in a monolayer and submonolayer regime. This is, therefore, a crucial step toward the development of a Ba^{2+} detector.

All the indicators developed by the NEXT experiment are based on crown ethers. Because of their capability to capture a variety of guest species, including metal cations, protonated species and neutral and ionic molecules [109], crown ethers [110] have been extensively used to recognise and trap metal or molecular ions [111, 112]. However, they have been poorly studied in solid state. Few examples can be found in the literature where self-assembled monolayers of crown

ether derivatives have been grown and used on surfaces. Moreover, in all previous studies, either the growth or ion trapping or both have taken place in solution [113–115]. There are only two works, as far as we know, where crown ethers were deposited under UHV conditions [77] and their metal trapping capability was proven also under UHV [98]. Thus, in addition to the progress relevant for a future $0\nu\beta\beta$ experiment, the work presented here advances substantially the understanding of the physico-chemical properties of crown ethers immobilised on solid surfaces.

6 *Ion trapping on Au(111) by next FBI generations*

As introduced in chapter 3, by modifying the FBI molecular structure, it is possible to shift in fluorescence emission before and after chelation with Ba^{2+} ions. In this chapter I explore the response of new members of the FBI family on surfaces, in particular the FBI-G2 and FBI-G3 in Fig. 3.3. These new molecules were designed and synthesized with the objective of maximizing their Ba^{2+} chelation efficiency and the color shift thus induced. The photophysics studies in solution concluded that G2 undergoes the maximum color shift. G3 performed similarly and is therefore considered another promising alternative to G1. In this chapter we build on the results for G1 on surfaces from chapter 5 and characterize G2 and G3 chelation with Ba^{2+} on surfaces.

First, we repeat their deposition under UHV, following the procedure used for FBI-G1, and explore their chelation using a barium salt, $BaCl_2$. We observe, again, the lack of stoichiometry in the $BaCl_2$ salt when deposited on FBI functionalized surface, as it happened for FBI-G1. We ascribed this effect to partial desorption of the chlorine atoms from the surface. We examine this effect in more detail in this chapter and argue that molecules of the FBI family can be used to induce dechlorination reactions on surfaces. Moreover, we investigate the chelation of FBIs with another cation aside of Ba^{2+}: Fe^{2+} . We again confirm that both effects take place with FBI-derivatives on gold surfaces in UHV.

6.1 Evaporation of FBI-G2 and G3 in UHV

FBI-G2 and G3 were deposited on a Au(111) surface by sublimation in UHV and we used XPS to characterize their chemical composition. We compared these spectra to the ones recorded with FBI-G1 in chapter 5.

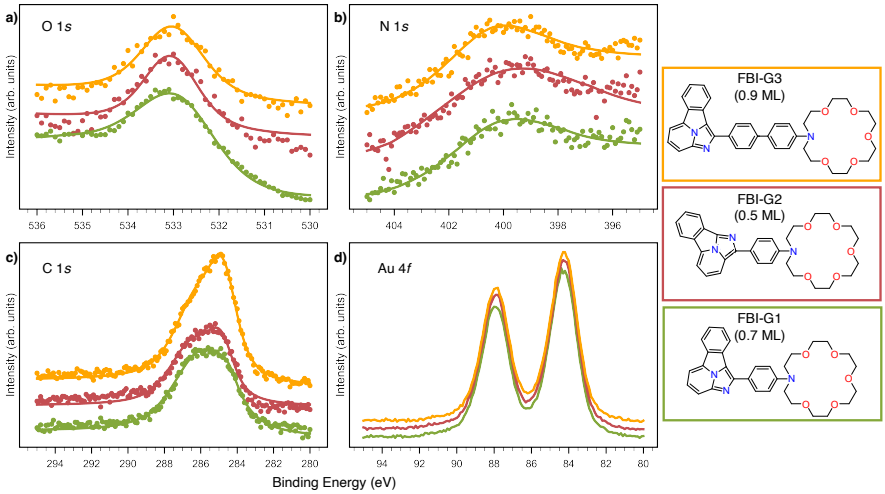

Figure 6.1. XPS spectra of FBI-G1 (0.7 ML, green), G2 (0.5 ML, red) and G3 (0.9 ML, orange) on Au(111) in the regions of O 1*s* (**a**), N 1*s* (**b**), C 1*s* (**c**) and Au 4*f* (**d**). The spectra have been normalized to the Au 4*f* intensity to compare the relative intensities of the different FBI generations. The spectra were manually shifted in the y-axis for clarity. For the panels **a)-c)** the dots correspond to raw values and the solid lines to fitted curves.

The results are collected in figure 6.1. The three molecular core levels O 1*s*, N 1*s* and C 1*s* are shown in Fig. 6.1a, 6.1b and 6.1c, respectively. All spectra were normalized to the Au 4*f* intensity shown in Fig. 6.1d (the lines have been manually shifted in the y-axis for clarity). The dots correspond to raw data and the solid lines to fitted curves. The green data corresponds to G1 (same spectra as in Fig. 5.3), the red data to G2 and the orange data to G3. The positions and relative intensities in all molecular core levels agree with that of G1, except for the intensity of the G3 spectrum in the C 1*s* region, since G3 contains 6 extra C atoms. The fits to the core levels in the C 1*s* region contain two components centered each at 284.7 and 286.0 eV, respectively. The former, more intense, corresponds to C-C bonds, whereas the latter includes contributions from C-O and C-N bonds. The relative intensities of the components agree with having intact molecules. In the case of G1 and G2, the areas of the C-C and C-O/C-N components have a ratio 1.5:1, which is compatible with having 26 C-C bonds

and 17 C-O+C-N bonds. In the case of G3, the C-C and C-O/C-N components, the area ratio is 1.9:1, since it contains 32 C-C bonds and 17 C-O+C-N bonds.

In the N 1*s* region, all molecules present a faint peak around 400.4 eV. The position of the maximum is compatible with the enamine-imine groups of the molecular composition. Finally, the O 1*s* core level presents a single component peak centered at around 533.0 eV, which is compatible with previous reports on closely related crown ether groups. The ratios between the core levels for G1 and G2 are C/O = 6.0, C/N = 10.3, which agrees with having molecules of $C_{31}N_3O_5H_{35}$ stoichiometry on the surface (FBI-G1,G2 molecule stoichiometry). In the case of G3, the ratios are C/O = 8.0, C/N = 11, in agreement with a stoichiometry of $C_{37}N_3O_5H_{39}$. In chapter 5, we further confirmed the intact sublimation of G1 molecules by STM, and the chemical characterization of G2 and G3 agrees with the expectation from G1. Therefore, we conclude that G2 and G3 sublimate intactly too.

As an additional test, we used STM to confirm that the G2 molecules sublimated intactly. We deposited a submonolayer of G2 molecules on Au(111) and imaged the sample at 4 K. These molecules tend to form dimers, as can be seen in the large scale STM image in Fig. 6.2a. The molecules in the dimers can be arranged in different orientations, but the most common is shown in the zoom image in Fig. 6.2b together with a model of the two molecules. The crown-ethers appear as a three-dimensional (i.e. non-planar) triangular-lobed structure. The crown-ethers interact with the fluorophores, which are flatter and therefore present a more less prominent shape. This interaction seems to cause the electronic structure of the fluorophore to bend around the crown ether in an approximate V-shape. This tendency of FBI-G2 to form dimers is clearly dissimilar to the trend of FBI-G1, which forms molecular islands (see Fig. 5.4a). The difference in structure formation between G1 and G2 highlights how the behaviour of molecules on surfaces can change radically even if the only difference in chemical structure is a C-N permutation. Individual molecules were also found in the sample, as shown in Fig. 6.2c. In this case the crown-ether could be attached to an Au adatom from the surface. Moreover, since the fluorophore is not interacting with any other crown-ether, its V-shape is not visible anymore and instead appears more lobular.

These STM results are still preliminary and will be covered in more

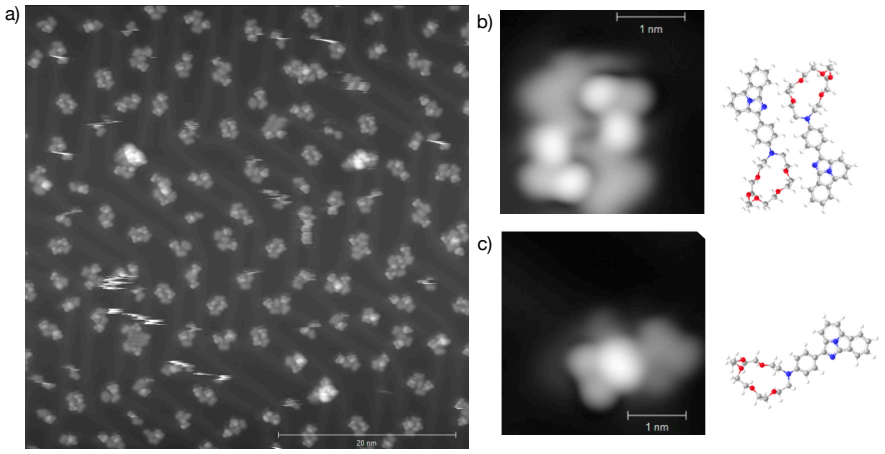

Figure 6.2. STM images FBI-G2 on Au(111) measured at 4 K. (**a**) Large scale STM image (50×50 nm^2) of FBI-G2 forming a submonolayer of dimers on Au(111). (**b**) Constant current zoom of a FBI-G2 dimer. (**c**) Constant current zoom of an individual FBI-G2 molecule attached to an Au adatom.

detail in [116]. These images were recorded thanks to the collaboration of the group of Prof. Jorge Lobo and Prof. David Serrate from the Instituto de Nanociencia y Materiales de Aragón (INMA) in Zaragoza.

6.2 Chelation of FBI-G2 and G3 with Ba^{2+} in UHV

Once the presence of intact FBI-G2 and G3 molecules on the surface was confirmed, $BaCl_2$was sublimated to test the molecular chelation. Figure 6.3 and 6.4 show the XPS spectra measured for subsequent depositions of $BaCl_2$on Au(111) covered with 0.5 ML of FBI-G2 and 1.2 ML of FBI-G3, respectively. Even though the Cl 2*p* spectra is not shown, it is worth mentioning that upon $BaCl_2$addition we detect fluctuations in the Ba:Cl ratio. This is due to partial desorption of Cl atoms from the surface, as it happened for FBI-G1. However, the Ba 3*d* core level does not show any significant shift when comparing the sublimation of $BaCl_2$on bare or functionalized gold surface, suggesting that there is no change in the Barium chemical oxidation state.

In figure 6.3 the red data represents the unchelated FBI-G2 layer

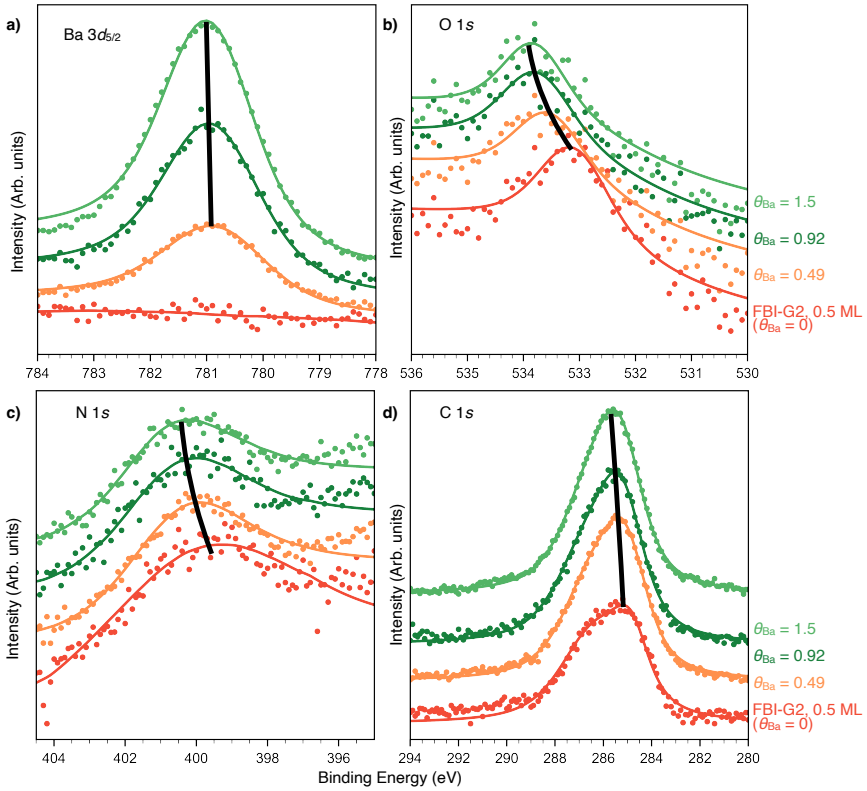

Figure 6.3. XPS spectra of FBI-G2 (0.5 ML, red), on Au(111) in the regions of Ba $3d_{5/2}$ (**a**), O 1*s* (**b**), N 1*s* (**c**) and C 1*s* (**d**) for different $BaCl_2$dosing θ_{Ba}: 0.49 (orange), 0.92 (dark green) and 1.5 (light green). The spectra have been normalized to the Au 4*f* intensity (not shown). The spectra were manually shifted in the y-axis for clarity. For all panels the dots correspond to raw values and the solid lines to fitted curves.

(θ_{Ba} = 0), with a coverage of 0.5 ML (the same as the orange lines in fig. 6.1) and the subsequent spectra corresponds to increasing doses of $Ba^{2+}$from less than 1 Ba ion per molecule to nominal 1.5 Ba^{2+}per molecule. The evolution of the core levels with progressive dosing of Ba^{2+} is highlighted by the solid black line joining the maxima of each curve. In general the core levels shows slight shifts toward higher BE, as in the case of G1. The absolute magnitude of the shift varies, being almost undetectable for C 1*s*, but not for O 1*s* and N 1*s*.

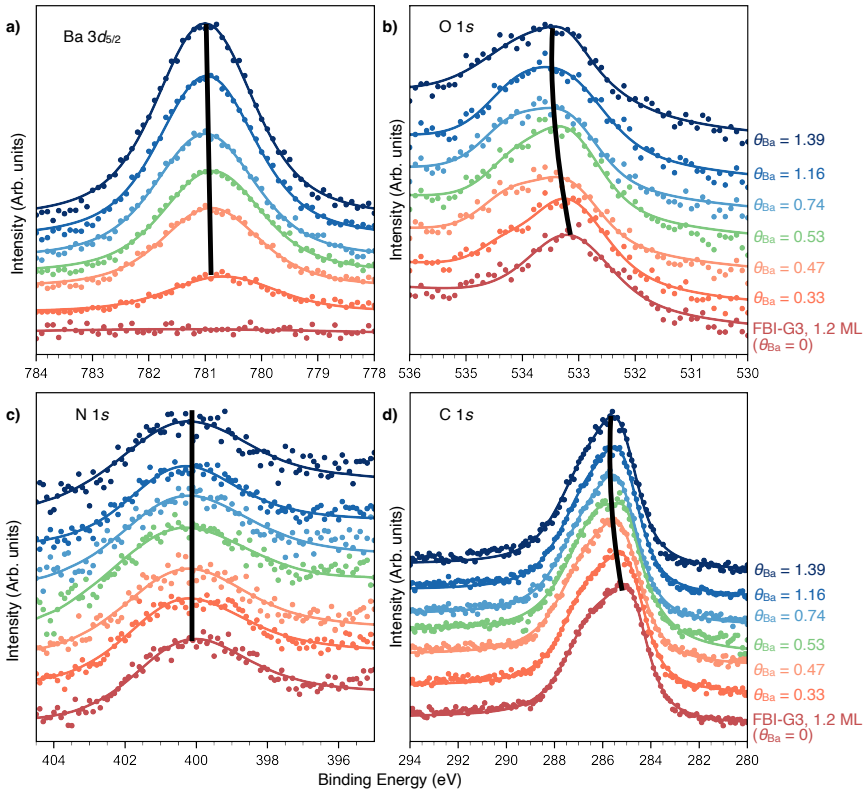

Figure 6.4. XPS spectra of FBI-G3 (1.2 ML, red), on Au(111) in the regions of Ba $3d_{5/2}$ (**a**), O 1*s* (**b**), N 1*s* (**c**) and C 1*s* (**d**) for different $BaCl_2$dosing θ_{Ba}: 0.33 (orange), 0.47 (tangerine), 0.53 (green), 0.74 (cyan), 1.16 (blue) and 1.39 (indigo). The spectra have been normalized to the Au 4*f* intensity (not shown). The spectra were manually shifted in the y-axis for clarity. For all panels the dots correspond to raw values and the solid lines to fitted curves.

The maximum shift takes place in the O 1*s* is ΔE = -0.7 eV for θ_{Ba} = 1.5 with respect to θ_{Ba} = 0. This energy shift is much larger than in the cases of G1 and G3. This suggests that the affinity for Ba^{2+} chelation of G2 is higher than that of G1 and G3. The maximum N 1*s* level shift is ΔE = -0.5 eV. Similarly to the case of G1, the N 1*s* peak notably shifts, whereas the C 1*s* peak does not, suggesting that the nitrogen in the benzoimidazoindolizine group is interacting with the Ba^{2+} ion. This agrees with DFT simulation as I will show in section 6.2.1.

Similar results are obtained for FBI-G3. The red spectra in Fig. 6.4 represent the unchelated FBI-G3 molecule and the rest are measurements upon $BaCl_2$sublimation. The evolution of the core levels with progressive dosing of Ba^{2+} is shown as a solid black line joining the maxima of each curve. In this case, the N 1*s* core level does not visibly shift, and the maximum shift for the O 1*s* level shift is ΔE = -0.3 eV for θ_{Ba} = 1.39. When Ba^{2+} is added the O 1*s* core level becomes wider and a new component has to be introduced at a higher BE position. The non-chelated G3 has a single component at 532.95 eV, while for chelated FBI-G3, the new component is centered at around 533.9 eV, position consistent with O-Ba interaction (chelated crown ether)[98].

It is worth noting that in the case of FBI-G1 chelation with Ba^{2+} the shift toward higher BE was mostly produced in the O 1*s* and N 1*s* core levels, while the C 1*s* peak barely shifted. In this case, the C 1*s* shows a clear evolution with the coverage, suggesting that in this case, the extra phenyl ring in G3 is being affected by the interaction with Ba^{2+}instead of the N 1*s*, as predicted by the DFT simulations.

6.2.1 DFT simulations for FBI-G2 and G3

The behavior of G2 and the three sub-variants of G3 upon chelation with Ba^{2+} was studied using DFT. The main results are shown in figure 6.5. All structures shown in Fig. 6.5 are optimized at the B3LYP-D3BJ/6-311++G**&LanL2DZ level of theory and the bond distances are given in Å. In all four cases, the Ba^{2+} ion interacts with the five oxygen atoms in the crown-ether, and phenyl ring via π-complex. For FBI-G3a (Fig. 6.5a), the second phenyl ring also partakes in the chelation via π-complex. In the cases of FBI-G3b and G3c (Fig. 6.5b and 6.5c, respectively), the interaction is with the nitrogen atoms in the second aza-phenyl rings. In the case of FBI-G2 (Fig. 6.5d) the nitrogen in the benzoimidazoindolizine interacts with the Ba^{2+} ion, equivalently to the case of FBI-G1.

6.3 Chelation of FBI-G2 and G3 with Fe^{2+} in UHV

In chapter 5 we saw that Na^+ could be chelated by FBI-G1, although the ion was located on the center of the crown-ether without affecting the structure of the fluorophore. In order to test the capacity of FBI-G2

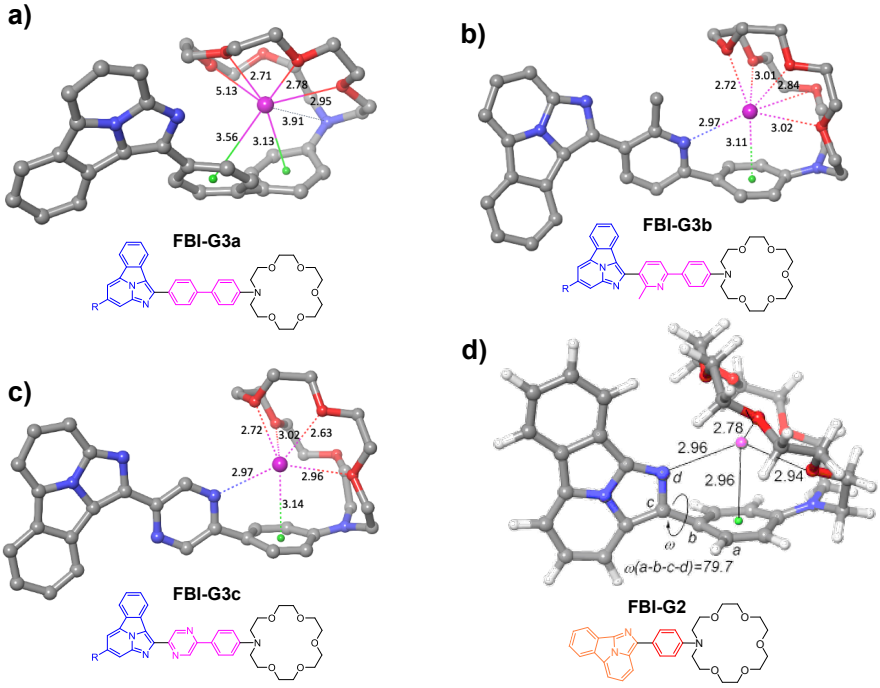

Figure 6.5. Optimized geometries (B3LYP-D3BJ/6-311++G**&LanL2DZ level of theory) of FBI-G3 and G2 coordinated with Ba^{2+}. a) FBI-G3a, X = Y = CH, Y = H in Fig. 3.3; b) FBI-G3b, X = N, Y = CH_3, Z=CH; c) FBI-G3c, X = Z = N, Y = H and d) FBI-G2. Bond distances are given in Å.

and G3 to chelate other ions, we carried out a series of experiments involving Fe^{2+} -chelation. We evaporated $FeCl_2$ salt on FBI-G2- and G3-functionalized Au(111) and performed XPS and NEXAFS. The experiments were conducted at the ALOISA beamline of the ELETTRA synchrotron. Since these experiments were performed using synchrotron radiation and grazing incidence, the resolution is much higher than for the previous results, which were obtained using a non-monochromatic Al K_α source.

The experiment we carried out is presented in schematic form in Fig. 6.6. The FBI molecules were evaporated on a Au (111), then analyzed by XPS to determine the chemical composition and by NEXAFS to study the geometrical absorption conformation. Then $FeCl_2$ salt was sublimated and again XPS and NEXAFS were used to follow the

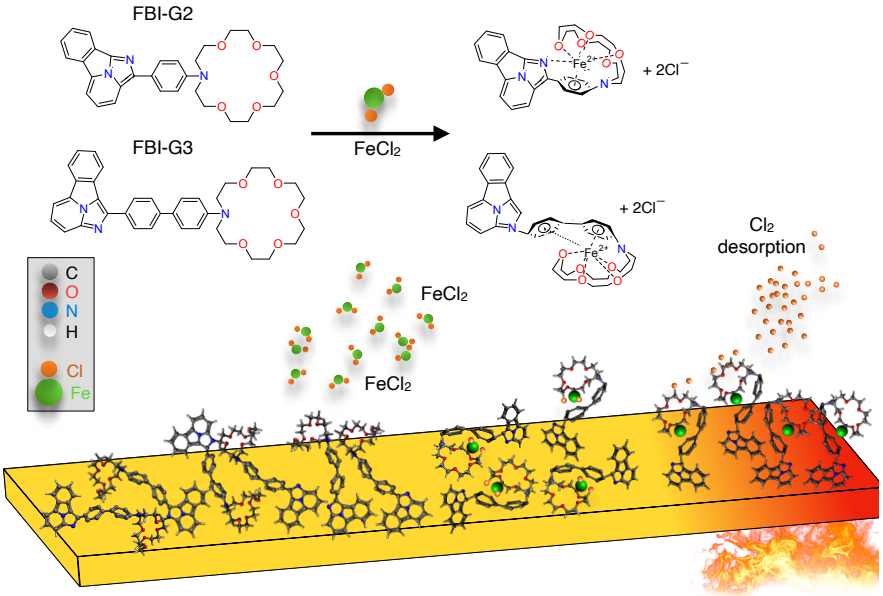

Figure 6.6. Model of FBI-G3 and FBI-G2 before and after chelation with $FeCl_2$. Schematic of the experiment we have carried out. FBI-G3 and $FeCl_2$ were deposited on Au (111), then the sample was annealed to $\sim$ 120 ºC and dechlorination was observed.

chemical and structural changes. Finally, we annealed the substrate to check the stability of chelated FBI molecules and to test whether increasing the temperature improves the chelation efficiency.

A coverage of 0.45 ML was estimated using a quartz microbalance. The layer thickness was converted into coverage by assuming a molecular radius of 1 nm.

Figure 6.7 collects the XPS spectra of FBI-G2 (6.7a-c) and G3 (6.7d-f) in the regions of O 1*s*, N 1*s* and C 1*s* core levels. The red lines correspond to free G2 molecules and the green lines correspond to a $FeCl_2$ dosing of 0.33 per G2 molecule. The dosing was estimated by comparing the $FeCl_2$ and G2 coverages (see subsection 6.3.3). The O 1*s* core level (Fig. 6.7 a) shows clear changes after this dosing. Before $FeCl_2$ addition, the peak is centered on 532.7 eV, and can be fitted with a single dominant component (red). Upon addition of $FeCl_2$, the main component of the peak appears at 533.3 eV (green line). This shift

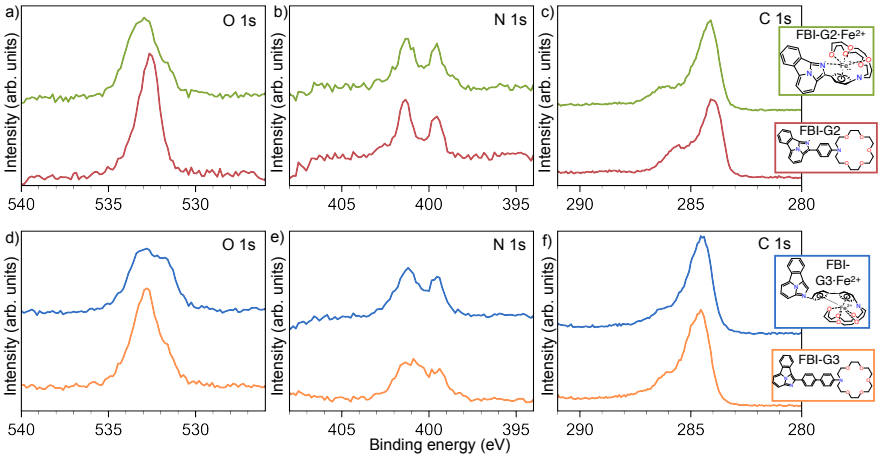

Figure 6.7. (Top) XPS of free FBI-G2 on Au(111) (red lines) and after Fe^{2+} chelation (green lines). (Bottom) XPS of free FBI-G3 (orange lines) and after Fe^{2+} chelation (blue).

toward higher BE is the same effect that takes place for FBI chelation with Ba^{2+}, both for G1 (chapter 5) G2 and G3 (section 6.2). A second component also grows at lower BE, 532.3 eV.

The N 1*s* core level presents two clearly different components: one slightly more intense at 401.2 eV, associated to the two enamine nitrogens (one in the aza-crown-ether and one in the fluorophore) and another component at 399.8 eV associated to the imine nitrogen in the fluorophore. The N 1*s* core levels does not visibly change with this dosing of $FeCl_2$.

Chelation affects the C 1*s* more tenuously. The C 1*s* peak contains two components, at 284 eV (C-C bonds) 285.2 eV (C-O and C-N), respectively. Addition of $FeCl_2$ causes the latter component to shift slightly toward higher BE (285.7 eV).

The molecular core levels of the FBI-G3 are shown in Fig. 6.7(d-f). In this case, the coverage of the sample was 0.5 ML. The core levels of the free G3 molecule (orange lines) present several features different from those of G2: the main component of the O 1*s* peak appears at higher BE (532.9 eV) and a second component at 531.8 eV. This difference reflects a difference in the chemical environment of the oxygen between the two molecules. G3 is expected to have

more flexibility and its crown can therefore be more detached from the surface. We associate the two components to oxygen atoms with different degrees of interaction with the Au substrate. The small component at low BE would correspond to oxygen atoms closer to the surface and the main component to atoms farther away from the Au.

We evaporated $FeCl_2$ reaching a ratio of θ_{Fe}= 0.32 Fe^{2+} ions per G3 molecule. Chelation of Fe^{2+} by G3 is again clearly reflected in the changes in the O 1*s* peak (Fig. 6.8d): the component centered at 531.8 eV grows significantly in the core level of the chelated G3 (blue lines). Surprisingly, this trend toward *lower BE* is the opposite of the trend observed in our previous study of Ba^{2+}-chelation with FBI-G3 (section 6.2), with FBI-G1 [117] and in Na^+ -chelation by crown-ethers [98]. The chelation with a transition metal ion (Fe^{2+}) induces a different change than with an alkaline earth ion (Ba^{2+} and Na^+). The growth of the component associated to O-Au interaction hints to the chelated molecule becoming flatter. This may not be the case for G2 under these conditions, since the stability provided by the dimerization may compete with the changes induced by chelation with the ion.

The N 1*s* peak is also affected by Fe^{2+} chelation: the two components at 401.2 and 399.8 eV, respectively, remain in their positions but become better resolved after adding $FeCl_2$. This is due to a narrowing of the component at higher BE and a relative increase in intensity of the component at lower BE.

6.3.1 *Effect of temperature*

To study the effect of temperature on the chelation, the FBI-G2 sample was annealed to 150 ºC after $FeCl_2$ deposition. The corresponding XPS spectra for the molecular core levels are shown as tangerine lines in Fig. 6.8 (a-c). The red and green lines in those plots correspond to the free and Fe^{2+} -chelated molecules at RT (the same as in Fig. 6.7). After annealing, the O 1*s* (Fig. 6.8a) component at *lower BE* (532.3 eV) becomes as intense as the one at higher BE, following the same trend as in the case of G3. The temperature may allow a reorganization of the chelated molecules which competes with the stability provided by the dimerization. Then, the same flattening upon chelation may take place as in the case of G3.

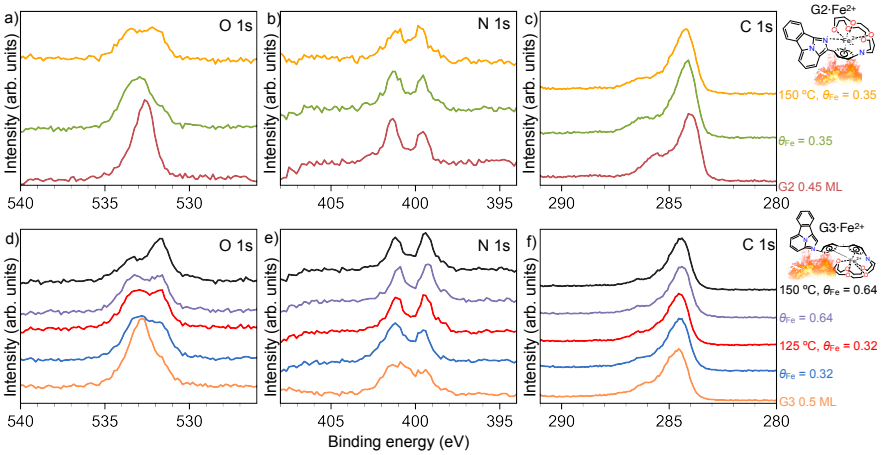

Figure 6.8. (Top) XPS spectra of FBI-G2 free (red), chelated (green) and annealed to 150 ºC (tangerine). (Bottom) XPS spectra of FBI-G3 free (orange) and with two different doses of $FeCl_2$: θ_{Fe}= 0.29 (blue) and θ_{Fe}= 0.57 (purple) The samples were annealed after each dosing of $FeCl_2$, at 125 ºC (red) and 150 ºC (black), respectively, and two additional spectra were acquired at those temperatures. (a,d) O 1*s* region, (b,e) N 1*s* region and (c,f) C 1*s* region.

The temperature also affects the N 1*s* peak (Fig. 6.8b): The component at lower BE (399.8 eV) becomes slightly more intense than the one at higher BE (401.2 eV) after annealing the sample. The lower-BE component is associated to the imine nitrogen in the fluorophore, which can interact with the chelated ion. However, in the case for Ba^{2+}(section 6.2) the shift was toward *higher BE*, as in the O 1*s*. This demonstrates that the response of the molecule to Ba^{2+} chelation is different to the response to Fe^{2+} . The C 1*s* core level (Fig. 6.8c) does not differ significantly after annealing from the previous state.

A similar temperature test was performed with FBI-G3. The molecular core levels are shown in Fig. 6.8(d-f). The chelated sample was first annealed to 125 ºC (red lines), then a second $FeCl_2$ dose of θ_{Fe}= 0.64 was added to the sample (purple lines). Finally, the sample was again annealed up to 150 ºC (black lines). The first annealing (red) causes the lower BE component in the O 1*s* core level (Fig. 6.8d) grow further. The spectrum is very similar to the one of annealed G2-Fe^{2+} (Fig. 6.8a, tangerine line). The same happens in the N 1*s* region, where the component at lower BE becomes more intense than the one at

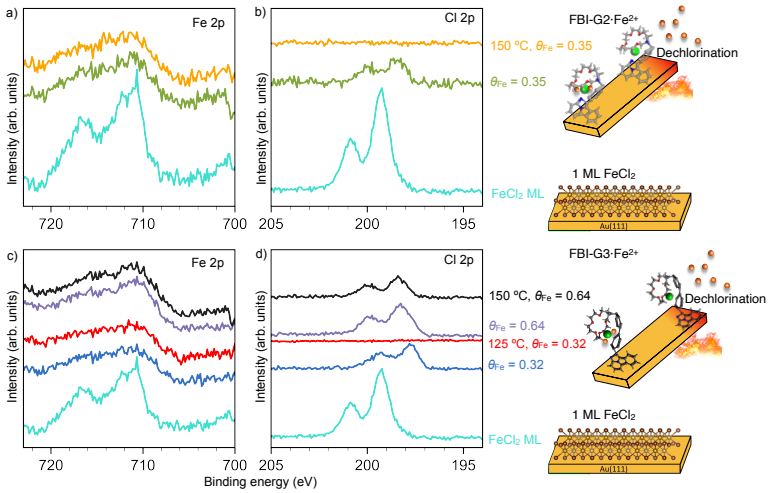

Figure 6.9. XPS in the Fe 2*p* (a,c) and Cl 2*p* (b,d) regions. (Top) 2 ML of $FeCl_2$ on prisine Au (111) (turquoise) compared to $FeCl_2$ deposited over FBI-G2 (green) and annealed to 150 ºC (tangerine). (Bottom) Comparison between $FeCl_2$ on pristine Au (111) (turquoise) and $FeCl_2$ deposited over FBI-G3 in two doses θ_{Fe} = 0.32 (blue) and θ_{Fe} = 0.64 (purple), and annealed to 150 ºC (black). In both cases, the Cl 2*p* shifts up to 1.3 eV to lower BE for the sample with FBI with respect to the one without. Moreover chlorine disappears after annealing at 150 ºC but iron remains.

higher BE.

The second $FeCl_2$dosage (purple line) does not affect significantly the spectra. However, after annealing the sample up to 150 ºC (black lines), the component at lower BE becomes the main one in the O 1*s* region. After this whole process, the position of the O 1*s* peak undergoes a net shift of around 1.5 eV. The C 1*s* core level of G3 (6.8f) remains unchanged during all these stages.

All O 1*s* peaks in figure 6.7 were fitted using a Voigt model (0.7 Gaussian, 0.3 Lorentzian) with two components. From top to bottom, the area relations between the component at higher BE with respect to to that at lower BE are 0.36:0.64 (orange), 0.51:0.49 (purple), 0.49:0.51 (red), 0.65:0.35 (green) and 0.8:0.2 (blue).

Role of the counter-ion

In order to explore the role of the counter-ion, Cl^-, we contrast the changes in the molecular core levels to those in the Fe $2p$ and Cl $2p$ regions. The latter are shown in figure 6.9. The top panel collects the spectra of chelated G2 sample and the bottom panel the spectra of chelated G3. The spectra of 2 ML of $FeCl_2$ on pristine Au (i.e. without any FBI molecule underneath) is also included in all four graphs for comparison. The position of the Fe $2p$ (Fig. 6.9a,c) is constant for all the spectra, which confirms that the iron stays as Fe^{2+} during all states of chelation and annealing. Instead, the Cl $2p$ (Fig. 6.9b,d) shifts toward lower BE for the chelated molecules with respect to the pristine $FeCl_2$ layer (turquoise). The shift is -0.7 eV for Cl in chelated G2 (top, green line) and -1.3 eV in chelated G3 (bottom, blue and purple lines). In both cases, the chlorine disappears when the sample is annealed to 150 ºC (black and tangerine lines). This confirms the hypothesis that the counter-ions do not play a significant role in the chelation of FBI molecules, as anticipated from DFT simulations. In fact, the presence of FBI-G2 or G3 causes the $FeCl_2$ salt to dissociate, as evidenced by the aforementioned shift with respect to the pristine $FeCl_2$ layer. This effect is the same as observed in dechlorinated Ullman coupling reactions [118].

We studied the dechlorination in more detail by measuring temperature-dependent XPS (TXPS) during the annealing runs on the Cl $2p$ region. Figure 6.10) collects these spectra in the format of a color map and a scheme of each process. We observed dechlorination of the sample for temperatures above $\sim$ 90 ºC for for a dosage of θ_{Fe} = 0.32 (Fig. 6.10 a). The Cl $2p$ double peak can be clearly seen at temperatures between 40-70 ºC, with the $2p_{3/2}$ component centered at 198 eV and the $2p_{1/2}$ component centered at 200 eV. The intensity of these peaks gradually decreases as the temperature raises and around 100 ºC the peak has mostly vanished. Similarly, for a higher dosage of θ_{Fe} = 0.64 (Fig. 6.10b), the chlorine persists up to around 140 ºC but fades rapidly at higher temperatures. We annealed the pristine $FeCl_2$ sample to a temperature up to 140 ºC. The result can be seen in Fig. 6.10c. In this case, no loss of Cl $2p$ intensity can be seen in the whole temperature range. Therefore, we conclude that the dechlorination observed in Fig. 6.10a is induced by FBI-G3 molecules.

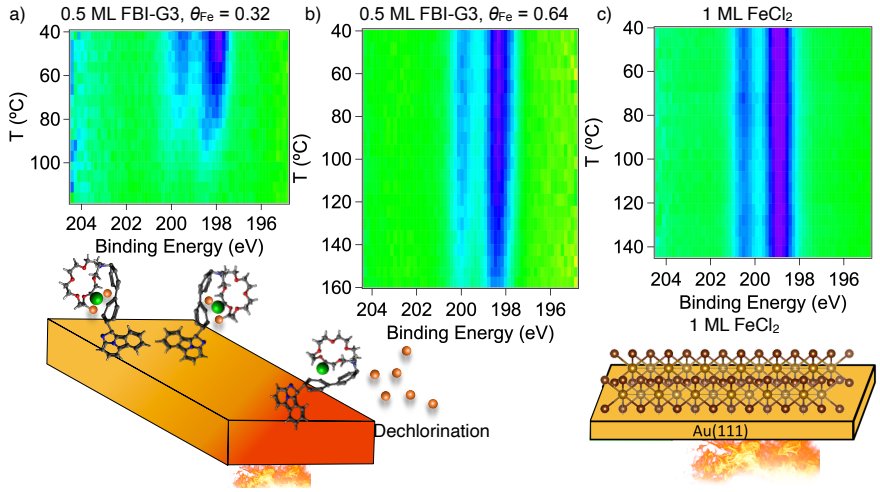

Figure 6.10. Temperature-dependent XPS of $FeCl_2$-chelated FBI-G3 a) in the Cl 2*p* region during annealing up to 125 ºC and of $FeCl_2$ deposited directly on the Au (111) surface and annealed up to 150 ºC. Dechlorination induced by the presence of FBI-G3 can be observed in a) over $\sim$ 90 ºC.

6.3.2 NEXAFS

The NEXAFS spectra corresponding to the experiments described above are presented in figure 6.11. The spectra of FBI-G3 were acquired at the regions corresponding to those of XPS (fig. 6.8). The FBI-G3 molecule presents clear dichroism in the molecular regions: C K-, N K- and O K-edge. The π^* resonance peak at 285 eV in the C K-edge spectra (Fig. 6.11a) is the largest in the normal orientation and decreases sharply for the parallel one, although it is still visible. This suggest that the fluorophore is mostly flat in all stages of chelation, with the exception of the spacer phenyl rings, which is slightly tilted and therefore contributes to the contribution in the parallel orientation too. The σ^* resonance peak of the CH_2-O groups in the crown ether appears at 289.3 eV [119].

The π^* region of the N K edge (Fig. 6.11b) shows two small peaks in the parallel orientation (solid lines) at 398.5 and 400 eV associated to the enamine group [119]. However, the main peak appears in the normal orientation centered on 401.9 eV for the unbound molecule (blue line). This peak is associated with the transition of a N 1*s* electron

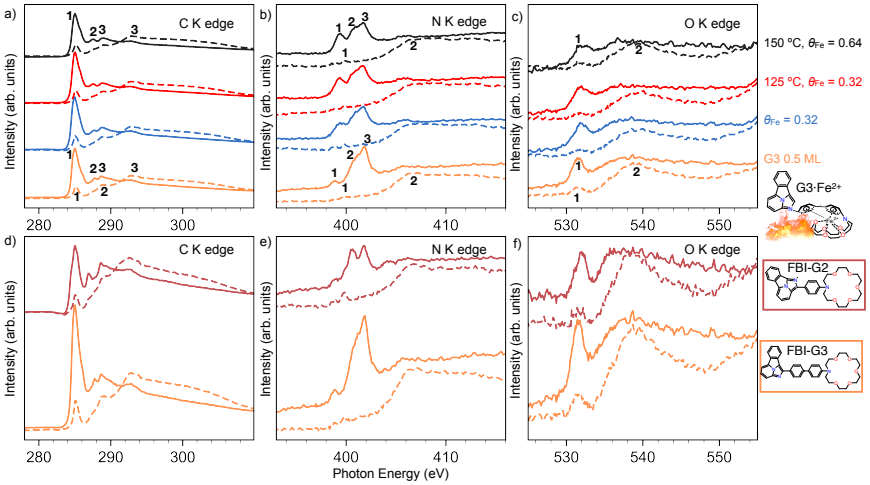

Figure 6.11. (Top) NEXAFS spectra of FBI-G3 free and with two different doses of $FeCl_2$ corresponding to the XPS spectra in figure 6.8. (Bottom) NEXAFS spectra of free FBI-G2 (red) and G3 (orange). The spectra were acquired at the regions of (a,d) C K edge, (b,e) N K edge, (c,f) O K edge and at two different orientation of the surface with respect to the photon beam polarization: normal (dashed lines) and parallel (solid lines).

from a N=C group into a LUMO+2 (π*) [120, 121]. The transition to the LUMO appears at 398.9 eV (secondary peak on the tail of the one at 401.9 eV). This secondary π* peak shifts to 399.5 eV and becomes more intense with each addition of $FeCl_2$. This is reminiscent of the electronic structure simulation presented in chapter 3, section 3.3.1 for G1, which showed that the dominant transition of the free molecule was HOMO-LUMO, while for the chelated molecule it was HOMO-1-LUMO.

The O K-edge (Fig. 6.11c) presents less dichroism than the rest of the organic levels (C and N), which is consistent with the crown-ether moiety being slightly lifted from the surface. The dichroism is largest in this region for the unbound molecule (blue line), and it decreases with each addition of $FeCl_2$. This is also consistent with the crown-ether being flatter for the unbound molecule and progressively bending over the scaffold as it captures the Fe^{2+} ion. The four spectra present a sharp peak at around 531.5 eV.

In [122], NEXAFS of DME and methanol (molecules containing

only C-O bonds) are presented. They attribute peaks resonances in the O K-edge at 534.1 (methanol) and 535.5 eV (DME) to O 1*s* $\rightarrow$ 3*s* transitions. In our case, the O K-edge peak instead appears at 531.5 eV, i.e. at ΔPE = -2.6 eV with respect to the case of methanol and ΔPE = -4 eV with respect to DME. Such a shift is too large to be attributed to the tilt of the crown ether with respect to the surface.

Peaks in the O K-edge around 532 eV are usually associated to 1*s* $\rightarrow$ π* in ketones (C=O) groups [123]. However, in [124] they argue that an O 1*s* electron could be directly excited into the π* orbital of the phenyl ring due to its proximity in polyphenyl ethers. Since only ether-like bonds (C-O-C) are present in the free unchelated molecule, the presence of a π resonance in the O K-edge must be due to this sort of bonds. It can either due to the proximity effect mentioned above or to solid-state effects [125]. In the case of Fe^{2+} -chelated molecules, transitions could occur from O 1*s* to the 3*d* orbital levels of iron [126]. In this case, the associated peak would appear at 532.7 eV. Indeed, the peak at 531.8 eV gets wider for the chelated-molecule spectra, meaning that a new component grows at the high photon energy (PE) shoulder. After annealing at 150ºC (orange line) a second peak is clearly visible at 532.7 eV.

The NEXAFS of free G2 and G3 are compared in the bottom panel of figure 6.11. The C K edge (Fig. 6.11d) of G2 presents similar features as that of G3. The π* resonance from phenyl rings at 285 eV is less intense than that of G3, since G2 contains just one ring. The same is true for the π* resonance of the O K edge (532 eV), which is slightly more intense for G3. This supports the hypothesis that the peak corresponds to O 1*s* $\rightarrow$ π* from the neighbor phenyl rings. The peak at 288.7 eV associated to CH_2-O bonds from the crown ether [119, 122, 127] appears in both normal and parallel orientations. This lack of dichroism again reflects the fact that the crown ether is slightly tilted over the surface. Another peak in the normal orientation appears in G2 at 286.7 eV, associated to C-N bonds [119], which are mainly flat. This implies a shift of 1 eV with respect to its homologous in G3 at 287.7 eV.

The N K edge of G2 (Fig. 6.11e) presents the same peak at 401.9 eV in normal orientation as G3. However, the another component around 400.7 eV appears with similar intensity. In the case of G3, this component was subdominant and contributed to the width of the

main peak with its maximum at 401.9 eV.

The O K edge spectrum of G2 (Fig. 6.11f) is very similar to that of G3, as the aza-crown ether moiety is identical in both molecules. The π* resonance at 532 eV is slightly shifted with respect to the peak of G3 (531.8 eV), and it also presents clear dichroism.

6.3.3 *Calculation of θ_{Fe} dosing*

The dosing θ_{Fe} was calculated by comparing the coverages of G3 and $FeCl_2$ and normalizing by the relative cell sizes:

$$\theta_{Fe} = \frac{t_{FeCl_2}}{t_{G3}} \cdot \frac{A_{FeCl_2}}{A_{G3}} = \frac{t_{FeCl_2}}{t_{G3}} \cdot \frac{3\sqrt{3}a^2/4}{L^2} = \frac{t_{FeCl_2}}{t_{G3}} \cdot 0.04, \qquad (6.1)$$

where t_X is the layer thickness of material X and A_X is the cell size of material X. The factor corresponds to geometrical considerations: $FeCl_2$ grows as a hexagonal crystal lattice with dimensions $a = b =$ 3.51 Å, $c = 6.18$ Å and γ= 120°. Each cell contains two Fe atoms. We model the cell size of G3 as square of size L = 2 nm containing a dimer, i.e. two G3 molecules.

Sublimating $FeCl_2$ for 3 min resulted in a coverage of 1 ML.

6.4 Conclusions

FBI-G2 and G3 molecules sublimate intactly and are able to chelate Ba^{2+} on metalic surfaces in UHV. This is evidenced by the shift in the O 1*s* core level toward higher BE, similarly to the effect of Ba^{2+} chelation by FBI-G1. STM images show that G2 tend to form dimers on the surface.

The effect of Fe^{2+} chelation by G2 and G3 is complex. The same shift in the O 1*s* core level toward higher BE happens for G2 as for Ba^{2+} chelation. By contrast, Fe^{2+} chelation of G3 causes the O 1*s* peak to shift toward *lower BE*. Furthermore, this shift is exacerbated when the sample is annealed. Under those conditions, the shift for G2 is also toward lower BE. We associated this trend to a flattening of the molecules produced by chelation. In the case of G2, extra energy must be added in the form of heat to overcome the stability provided by dimerization.

FBI-G2 and G3 molecules induce dechlorination of $FeCl_2$ salt on Au (111) surfaces. This effect takes place at room temperature, as evidenced by the shift between the Cl $2p$ for $FeCl_2$ over FBIs with respect to the pristine $FeCl_2$ layer. Annealing the sample causes the chlorine to desorb at around 100 ºC. This proves that the counter-ion does not play any role in the chelation with FBI molecules.

7 Development of a Fluorescence Microscope

The previous chapters in this thesis focused on the development and characterization of the monolayer of chemosensors using mainly surface science techniques. However, in the final scheme, detection of barium presence will be achieved through Single Molecule Fluorescence Imaging, so a set of fluorescence microscopy techniques must be developed in parallel. In this chapter, I will introduce the principles of the techniques and the advances carried out during this thesis to develop a single molecule microscope. This setup must be adapted to exploit the optical properties of the molecules chosen to capture Ba^{2+}.Although for simplicity, the experimental results will be presented mainly for FBI-G2, the principle of Ba^{2+} detection with all generations of FBIs is the same: distinguishing chelated from unchelated molecules by the different fluorescence emission color of each species. Therefore, the detection is achieved through *emission spectroscopy*.

In addition, another kind of bicolour chemosensor is studied in this chapter: Phosphorescence Bicolour Indicators (PBI). These molecules, introduced in Chapter 3, also emit in two different colours depending on whether they have captured Ba^{2+}. However, the origin of the shift is different. While in the FBI family the shift is associated to the variations in the π conjugation, the PBI's shifts present different emission relaxation times: short-lived (fluorescence) for the unchelated molecules and long-lived (phosphorescence) in the chelated molecules. The microscopy setup we developed includes a branch dedicated to detection of these phosphorescence indicators and will be discussed in this chapter too. The technique used in this case is *Time-Resolved Fluorescence detection*.

7.1 Requirements for the microscopy setup

Since the final device must be operated inside the NEXT TPC, the design of the microscopy setup must fulfill some requirements:

1. The optical properties of the sample must be preserved in a dry atmosphere. The molecules must be anchored on a surface with no solvent or degassing polymer matrices to support them.

2. The scheme must be such that the equipment used for detection is compatible with the conditions of a vacuum chamber filled with gas Xe. Some parts of the setup, such as the detector and the laser source, may be coupled to the gas chamber through optical windows and remain outside the chamber. Microscope objectives vulnerable to extreme pressures or containing degassing grease cannot be operated inside the chamber.

Although these are the final requirement, during the time of this thesis it was not possible to have an operative microscope operating under these conditions: The microscope described in this chapter has only operated in air. The next immediate step will be to develop a microscope coupled to a vacuum chamber, so that both the Ba^{2+} chelation and the fluorescence detection happen *in-situ*.

7.1.1 Choice of excitation wavelength

A crucial parameter for the design of a fluorescence microscope is the wavelength of the excitation source. Tunable sources are available commercially, both coherent and incoherent. Indeed, an incoherent tunable source (a xenon lamp with a monochromator) was used to characterize the absorption and emission of FBIs and PBIs in solution. However, as starting point, we chose to use fixed-wavelength lasers. Laser microscopy allows for diffraction-limited spatial resolution, and high optical powers can be achieved.

The optimal excitation wavelength is the maximum in the absorption spectrum of the fluorophore. The absorption spectra of chelated and unchelated FBI-G1 and FBI-G2SL are shown in figure 7.1. For FBI-G1, the maximum is around 250 nm. However, lasers of 250 nm are hard to build; at this wavelength range, incoherent light sources

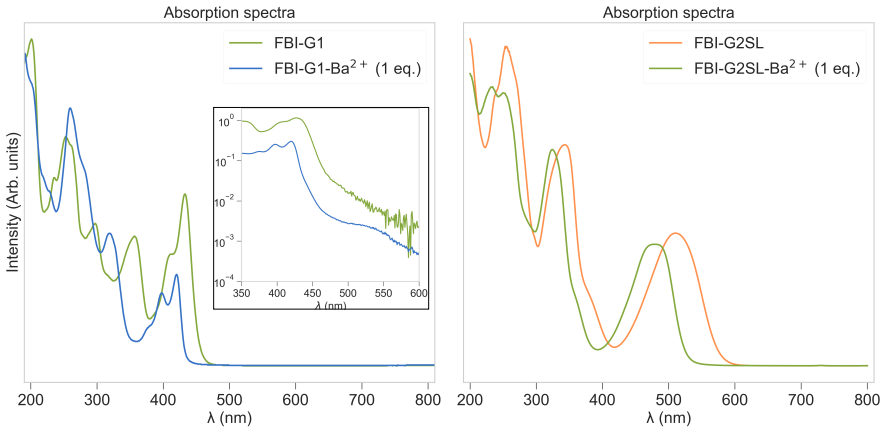

Figure 7.1. Absorption spectra. (Left) FBI-G1 (green) and FBI-G1-Ba^{2+} (1 eq. blue) in solution. Inset: zoom on the range (350, 600) nm with logarithmic scale on the y-axis. (Right) FBI-G2SL (orange) and FBI-G2SL-Ba^{2+} (1 eq. green) in solution.

are more commonly used. Excitation by Two-Photon Absorption (2PA) was initially considered in order to circumvent this limitation: a 522 nm laser could be used with 2PA to have the equivalent absorption of a 261-nm photon. However, the single-photon absorption spectra for both free and chelated FBI-G1 extended into the range of 500-550 nm, so the second order effect (2PA) would be completely disfavored at these wavelengths. The tail of the spectra in this region is close to zero but still nonzero, so this is better visualized in a logarithmic scale as shown in the inset of Fig. 7.1. A laser at a wavelength of around 800 nm, such as the one we used for the detection of chelation on the experiments with the silica pellets presented in sections 4.4 and 5.1, was assured to be far enough from the tails, so that the single-photon absorption did not suppress 2PA.

A 375 nm pulsed laser was chosen instead for simplicity (Edimburgh EPL 375). This wavelength assured single-photon absorption for both G1 and G2SL, even if the absorption was close to a minimum. The laser pulse period can be tuned in a range between 50 ns and 5 μs to match the window required for a time-resolved measurement. The maximum power reached with the laser EPL 375 nm (for the shortest pulse period) is $\sim$ 140 μW. For a brief period, a 405 nm laser was used

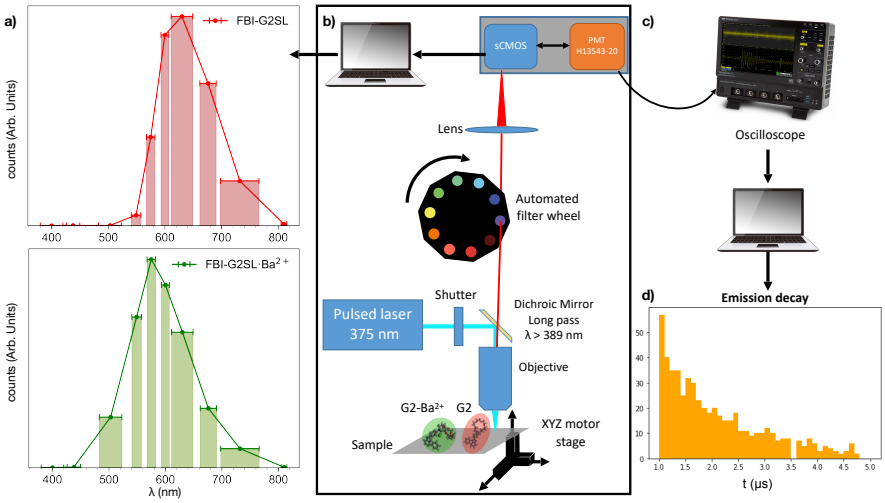

Figure 7.2. **a**) Discretized fluorescence spectra of G2 and G2-Ba^{2+}. **b**) Optical microscopy setup, with labels of the main components. **c**) Oscilloscope and computer, complementary components of the setup for time-resolved measurements. **d**) Example of an emission time-resolved measurement.

(Nichia NVSU233C), but the spot profile did not meet the requirements for shape regularity so it was replaced by the 375 nm laser. In addition, another pulsed laser with λ = 485 nm (EPL 485) was used for the first measurements of Time-Resolved Fluorescence detection. A 325 nm laser would favour absorption, as this wavelength is close to a local maximum in all four species, so this replacement is planned as an upgrade of the setup. However, all the results presented in this chapter were acquired with the 375 nm laser.

7.2 Description of the Microscope

An illustration of the microscopy setup is shown in figure 7.2b. The setup was installed in the Quantum Nanophotonics Laboratory at CFM, in close collaboration with the team Prof. Gabriel Molina-Terriza. For the first stages of the microscope development, the setup was installed on an optical table. The laser beam exits the source collimated and is guided by a long-pass dichroic mirror (Semrock FF389-Di01) to the backport of the microscope objective (MO) (Thorlabs LMM-40X-

UVV). The beam is focused by the MO onto the surface of the sample containing the fluorescent molecules. This configuration allows to reach a diffraction-limited lateral resolution of

$$d = \frac{\lambda}{2\mathrm{NA}} = 375 \text{ nm}, \tag{7.1}$$

where λ is the laser wavelength (375 nm) and NA = 0.5 is the numerical aperture of the MO. The fluorescence light is collected by the MO and filtered from the laser and ambient light by the long-pass dichroic mirror, with cut at 389 nm. Then a set of bandpass filters select specific ranges of emission. Since the objective is infinite-corrected, a lens is needed to form the image on the detector. A lens of focal length f = 150 mm allows to achieve a magnification of 40X. The fluorescence light is detected by a sCMOS (Hamamatsu ORCA Flash4.0 V3, C13440-20CU) with extremely low readout noise and high quantum efficiency. Each pixel is 6.5 μm by length and collects the light from an area of length 6.5 μm / 40 = 162.5 nm. However, because of diffraction, the lateral resolution is λ = 375 nm. The axis resolution in turn is

$$d = \frac{2\lambda}{\mathrm{NA}^2} = 3\ \mu\text{m}. \tag{7.2}$$

This configuration allows to obtain narrow field images. However, the most relevant information obtained is not the shape of the image per se, but the total intensity detected for each filter: A discrete emission spectrum of the sample can be measured by comparing the light detected through the different bandpass filters. The center and the bandwidth of the filter determine the position and the width of the bar, respectively and the detected intensity its height. An enveloping curve is drawn through the center of each bar. Two examples of discrete spectra of FBI-G2 on ITO surfaces are shown in figure 7.2a: sublimated FBI-G2-silatrane (green, top) and FBI-G2-silatrane chelated with Ba^{2+} from solution and deposited by spin-coating (red, bottom). Thus, the microscope is used as a spectrometer.

Moreover, the time dependence of the fluorescence emission can be measured with this setup (Fig. 7.2c). For this, a Photomultiplier tubes (PMT) (Hamamatsu H13543-20) is used as a detector instead of the sCMOS, since it can achieve the necessary time resolution in the range of nanoseconds. The signal is read by an oscilloscope (Teledyne Lecroy

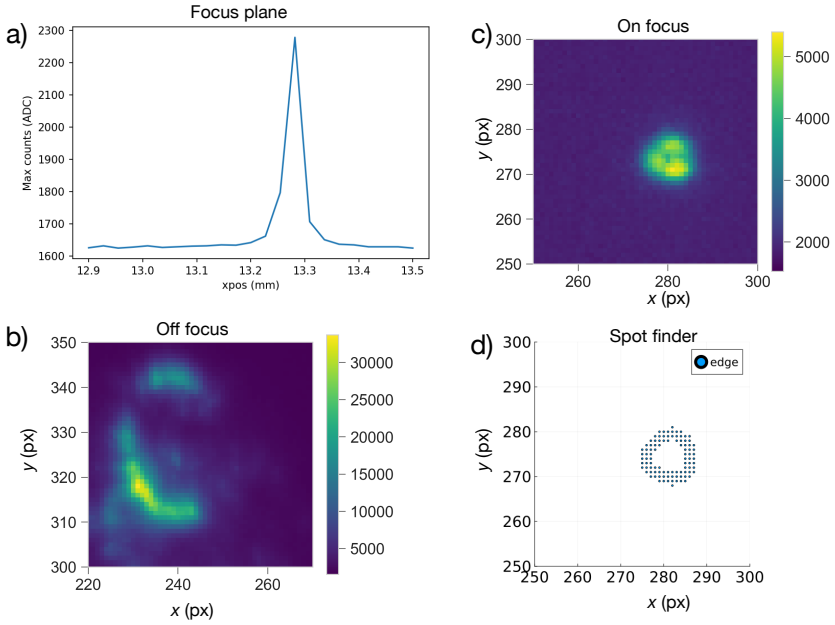

Figure 7.3. a) Autofocus: intensity variation with sample plane. The maximum corresponds to the location of the monolayer plane of emitters on the surface. b) Sample image of a slightly off-focus spot. c) Sample image of a focused fluorescence spot. d) Detected spot in the analysis software.

WaveSurfer 4000HD) after each pulse from the laser, which sends a trigger signal to the oscilloscope. To reduce electronic background, the peaks are selected, filtered and sorted by their delay time with respect to the corresponding trigger timestamp. The result is the decay graph shown in Fig. 7.2d. In particular the time dependence curve shown corresponds to a sample containing the phosphorescent compound tris(bipyridine)ruthenium(II). The time dependance of PBI emission can be measured in this manner.

7.2.1 Emission spectroscopy

The measurement protocol for emission spectroscopy was the following:

1. Characterization of the dark noise of the camera. For every

measurement, a set of images without illumination was acquired to subtract the base signal of the camera.

2. Selection of X-Y locations of the sample. Typically, around 9 points along the X-Y plane were chosen for each sample to survey the homogeneity of its emission.

3. Focus on the surface of interest. Since the samples were prepared on the monolayer regime, a fine control of the focal plane location of the emitters was necessary (Z axis). An autofocus algorithm was designed to locate this plane systematically. Briefly, the intensity detected by the camera was recorded as the sample plane was moved, and the maximum of this array of intensities coincided with the focus location. An example of this array is shown in figure 7.3a.

4. Acquisition of images of the emitters in narrow-field configuration. For each emission filter, an image was recorded. Unfiltered images were acquired as well to normalize of the spectra.

5. Offline analysis of the images. The fluorescence in narrow field imaged in a few tens of pixels, so they must be differentiated from all other pixels in the image. This assured reduction of systematic uncertainties like the appearance of hot pixels off-focus. A sample image of emission in focus is shown in figure 7.3b and the fluorescence spot detected by the analysis software in figure 7.3c. An example of emission slightly off-focus is shown in figure 7.3d. The intensities for each filter were then summed, normalized by the filter bandwidth and arranged in the discretized spectra as shown in Fig. 7.2a.

7.2.2 *Time-resolved fluorescence detection*

Time-resolved measurements were carried out with a PMT and an oscilloscope, as shown in fig. 7.2b. The emission spectrum can also be recorded by comparing the detection rate of the PMT (for a fixed trigger value) for each emission filter. An example of waveform in the oscilloscope for time-resolved measurements can be seen in figure 7.4a. The waveforms were passed through a Butterworth filter and

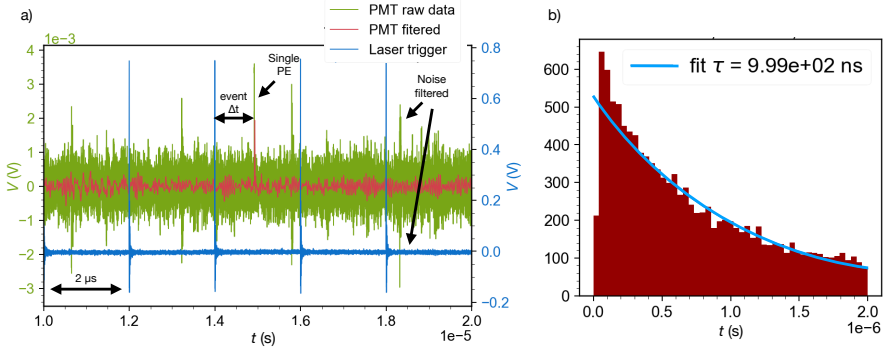

Figure 7.4. a) Sample waveform in the oscilloscope; the data from the laser trigger (blue) sets the duration and start point of each pulse, the raw PMT reading (green) is passed through some filters (red) to remove noise. Then the Δt from each single PE event is arranged into an histogram. b) Sample histogram from a phosphorescence measurement with fit to a negative exponential. The value of the exponential argument parameter (τ) is given as a reference.

a lowpass frequency filter in order to remove most of the electronic noise. The peaks with reflections (positive and negative values at very close times) indicated in Fig. 7.4a are some examples of such noise which is not present in the filtered PMT data (red line). The remaining, positive-only peaks correspond to single photoelectrons (PE) from fluorescence/phosphorescence emission. The time delay Δt between the laser pulse signal (blue line) and the appearance of each single PE was stored and graphed as an histogram (Fig. 7.4b). These time delays correspond to the decay process of phosphorescence photons. These decays have a lifetime in the scale of 100-1000 ns. The fit shown in Fig. 7.4b corresponds to a simple negative exponential. The laser pulse duration can be chosen from 7 fixed values in the range between 50 ns to 5 μs. Therefore, lifetimes up to 5 μs can be measured with this setup. The rise time of the PMT is 1.6 ns, so lifetimes in the scale of a few tens of ns can be measured (fluorescence).

7.3 Narrow-field Fluorescence on FBI-G2SL Monolayer

After optimization of the new setup, here I summarize the emission spectroscopy results obtained for the FBI-G2SL molecule. We de-

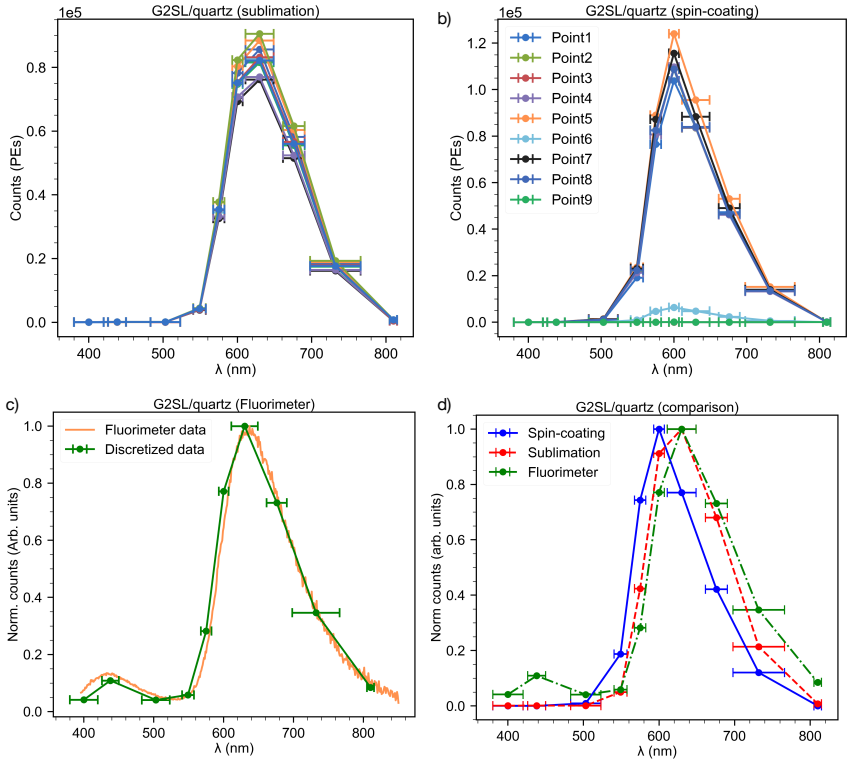

Figure 7.5. a-b) Discrete fluorescence spectra of FBI-G2SL along 9 points on quartz substrate, deposited by a) sublimation and b) spin-coating. c) Discretization of the continuous FBI-G2SL fluorescence reference spectrum for comparison with data from the microscope. d) Comparison of discrete FBI-G2SL spectrum obtained by the fluorimeter (green, dot-dashed line) and averages along the 9 points of a) and b). The spectra in c) and d) have been normalized to their respective maximum. Points 3 and 9 in b) were removed for the averaging (background).

posited G2SL on two substrates (quartz and ITO) by two different methods: molecular sublimation and spin-coating. Spin-coating consists in depositing a controlled amount of molecules from solution (usually a few drops from a syringe) on a substrate located on a spinning platform so that the coating material is spread by centrifugal force. All these samples were analyzed with XPS to assure that the formed layers are in the monolayer regime.

Figure 7.5a and b shows the emission spectra for the sublimation sample and the spin-coated sample, respectively. Fluorescence spectra were measured in 9 different points (3x3 matrix) to evaluate the homogeneity of the monolayer. The separation between the points was 1.5 mm in the X axis and 2 mm in the Y axis. For the sublimated sample (7.5a) the reproducibility of the spectra along the different points indicates highly homogenous coverages. For the sample prepared by spin-coating (7.5b), points 3 and 9 present almost no counts, which is compatible with having background counts only. This is also the case of point 6, which shows a very tenuous fluorescence signal (about 10 times less intense than the rest) but the shape was the same as the other points. These spectra suggest that sublimation yields slightly better results in terms of homogeneity.

Figure 7.5c shows the spectra of FBI-G2SL deposited on quartz measured using the spectro-fluorimeter for comparison. This fluorimeter is briefly described in A2.2. Since the microscope produces discrete spectra, the continuous spectrum from the fluorimeter is discretized according to the range of the filters used in the microscope. The comparison of the three spectra is shown in figure 7.5d. The emission spectra of the sublimated sample (red dashed line) is totally comparable with that measured for FBI-G2SL on the fluorimeter (green dot-dashed line). The relatively small discrepancies can be explained as follows: The emission at 438 nm (second data point from the left) of the fluorimeter data corresponds to background emission from the quartz substrate. The whole bulk of the quartz substrate contributes to this background, because the excitation source is not focused. The points of short wavelength ($\lambda < 630$ nm) are slightly more intense for the microscope data than for the fluorimeter, whereas for long wavelengths ($\lambda \geq 630$ nm) the opposite is true. We attribute this discrepancy to a higher contribution of background in the fluorimeter measurement. The emission from the spin-coated sample (blue solid line) is hard-shifted by around 32 nm toward shorter λ. Thus, the measurements reveal different photochemical properties for the spin coated sample compared to the sublimated and the reference sample. This work is still in progress so we currently do not have a conclusive answer to explain this result. However, we are considering two hypothesis. The first cause of the discrepancy could be the presence of residual solvent in the spin coated sample at the substrate-FBI inter-

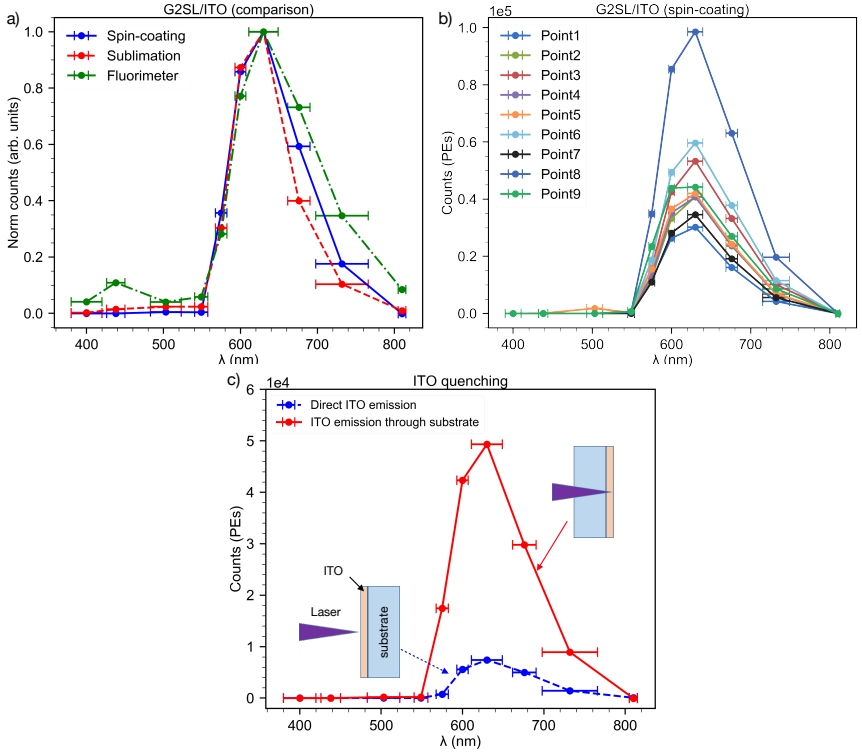

Figure 7.6. a) Fluorescence spectra of FBI-G2SL deposited by spin-coating on ITO along 9 points b) Comparison of G2SL spectra on ITO for a spin-coated sample (blue solid line), a sublimation sample (dashed red line) and reference fluorimeter spectrum (green, dot-dashed line). c) Effect of ITO quenching: when the fluorescence is measured directly from the surface containing the emitters (blue), the intensity is a factor 5 lower than for a transmission measurement (red). Inset: scheme of each measuring configuration.

face. The solvent may cause a Stokes shift toward shorter wavelenght. Alternatively, the sample prepared by sublimation may be more ordered on the surface at the nanoscale than the spin-coated one. Then, the latter would present more clusters and the electronic structures would be different. In any case, these intriguing results have been revealed by optimizing the microscope to work in the monolayer limit, thereby minimizing contributions from the substrate.

Moreover, further measurements reveal that the shift between the

sublimation and spin-coated samples is substrate-dependent. The two preparation methods yield much more similar average spectra on ITO surfaces, as shown in figure 7.6b. This may indicate a higher anchoring efficiency for ITO than for quartz. Figure 7.6b shows the spectra along the 9 points on the spin-coated ITO surface. Only one point emits more intensely than the rest by a factor 2. Therefore, the coverage homogeneity achieved by spin-coating along the ITO surface is higher than for quartz. It is well stablished in literature that the silatrane group works very efficiently in anchoring with the OH groups on the ITO surface [78, 79]. This seems not to affect sublimation samples, so the anchoring and distribution of the molecules on the surface becomes more homogeneous.

Another interesting effect found only for ITO samples is shown in figure 7.6c. When the fluorescence is measured in transmission through the quartz bulk (red line), the overall intensity is a factor 5 higher than when the same sample is measured directly from the ITO surface containing the molecules (blue line). These two measuring modes are sketched in the inset of the figure. Indeed, when the sample is measured in direct mode, the focus becomes very hard to find and many points on the plane show no fluorescence emission. This is attributed to quenching from the ITO surface. Quenching of fluorescence by conductors can be understood as an interaction between an electric dipole representing the emitter and a conducting surface. The surface induces a preferential emission toward the conducting surface and not away from it [128]. Therefore, when the fluorescence is measured from the side closer to the ITO surface, more photons are detected along this preferred direction of emission than from the opposite direction.

7.4 Chelation detection by Narrow-field Fluorescence

The objective of the microscope development presented in this chapter is to be able to distinguish between emission of chelated and unchelated FBI molecules. Figure 7.7a shows the emission spectra measured on two samples prepared by spin-coating on quartz, one containing FBI-G2SL (red, dashed) and the other containing FBI-G2SL chelated with $BaCl_2$ in solution (green, dot-dashed). The latter agrees with the emission in solution measured by the fluorimeter (blue solid).

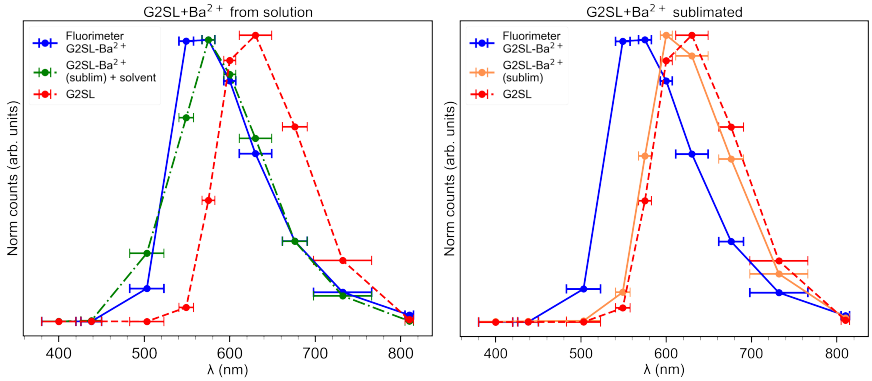

Figure 7.7. Chelation of FBI-G2SL on quartz. Comparison of the sublimated unchelated molecule (red, dashed) and chelated by two methods: (a) spin-coating from solution (green, dot-dashed) and (b) with sublimated $BaCl_2$ (yellow, solid). A discretized spectrum of the chelated molecule in solution measured by the fluorimeter is also included for reference in both panels (blue, solid).

The chelated molecule undergoes a color shift of $\Delta\lambda = -51$ nm as expected.

However, the situation becomes complicated when chelation takes place in a dry environment. This is the case illustrated in figure 7.7b. When the FBI-G2SL is exposed to sublimated $BaCl_2$ (orange line), the colour shift vanishes. This is a crucial result from the point of view of the development of the Ba-tagging sensor. Several hypothesis are being considered to explain it. One possibility is that having the molecules chemically anchored and standing upright conflicts with the trapping of the Ba^{2+} ion. However, XPS analysis on Cu of G2SL-Ba^{2+} show a similar shift in the O 1*s* core level as the ones mentioned for G1, G2 and G3. We therefore conclude that the ion is being trapped [129]. Still, the colour shift depends on the *folding* of the molecule upon chelation, not only on the trapping of the ion by the crown-ether. It is possible that the chelated molecule does not fold over itself in the upright formation (G2SL) as it does when the molecule lays flat on the surface (G2, see Fig. 6.2.1). Alternatively, stacking effects between several neighbouring molecules can compete with the folding process. For instance, one Ba^{2+} ion may be interacting with two molecules

simultaneously, with none of them folding. To overcome this stacking effects, the molecules can be arranged more sparsely by inserting a buffer molecule (for example, the anchoring group aminopropyl-silatrane, see Fig. 3.6) between them. This sort of sparse monolayer is being developed at the time of writing.

The absence of shift of chelated G2SL in dry conditions poses a difficulty for the advance of the barium sensor development. Nevertheless, revealing this result was possible only by developing the fluorescence microscope and optimizing it for detecting the signal of a molecular monolayer. Continuing this work with the microscope will permit assessing the performance of new molecules and sensor designs.

7.5 Lifetimes of phosphorescent compounds

Molecules on surfaces may not behave as they do in solution. In particular, the results in section 7.4 hint that a colour shift from the folding of chelated G2SL may not be straight-forward to detect. Therefore, another handle to distinguish chelated from unchelated molecules can be necessary. Another property which can reveal the presence of Ba^{2+} is the lifetime of the molecular indicators. This is the case of Phosphorescent Bicolour Indicators (PBI), which were introduced in chapter section 3.2. The emission of these molecules in solution is via fluorescence when they are unchelated and via phosphorescence when they are chelated. This means that the emission of unchelated molecules decay in a few nanoseconds, while the chelated ones decay in several hundreds nanoseconds. These change in the decay lifetime can be detected by Time-Resolved microscopy (section 7.2.2).

We carried out initial tests of time-resolved measurements with two phosphorescent inorganic molecules which are shown in figure 7.8a and b: Tris(2,2′-bipyridine)ruthenium(II) and (2,2-Bipyridine)bis[2-(2,4-difluorophenyl)pyridine]iridium(III). Both molecules are decorated with two anchoring 1-(3-aminopropyl)-silatrane (APS) groups and neutralized by hexafluorophosphate (PF_6). For convenience, they are referred to as RuSL and IrSL, respectively. Using these molecules as proxy for PBIs has several advantages. First, the fluorophores are commercially available so the synthesis consists only on adding

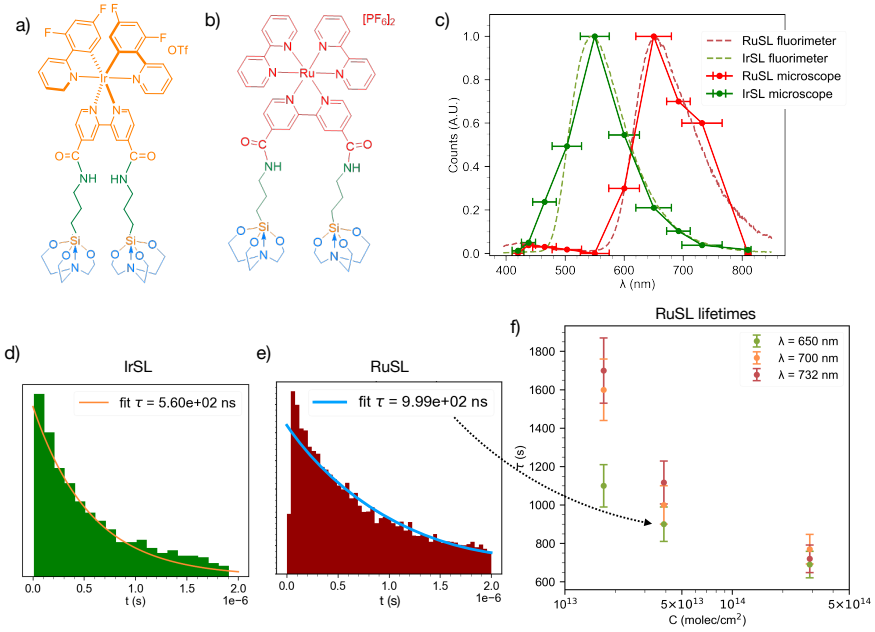

Figure 7.8. a-b) Structure of IrSL (a) and RuSL (b) molecules. c) Emission spectra of IrSL (green) and RuSL (red) as measured with the fluorimeter (dashed lines) and from the PMT rate (dots and solid line). d-e) Phosphorescence decay of IrSL (d) and RuSL (e) on quartz. f) Dependence of RuSL phosphorescence lifetime with the concentration for the wavelength ranges in the three central filters.

the APS groups. Second, their decay lifetimes are similar to that of chelated PBI. Third, their emission colors mimick that of chelated and unchelated PBIs; their emission spectra measured by the fluorimeter and the microscope is shown in figure 7.8c. Fourth, the fluorophore of PBI is based on IrSL, so studying the latter can provide valuable insight on the photophysics of the former.

The emission spectra were measured by comparing the PMT rate for the different filters (at the time of performing these experiments, the set of filters was different to the one presented in the previous section; some filters had wider bands and two overlapped). The comparison of the spectra measured with the PMT and with the fluorimeter is shown in Fig. 7.8b. Two examples of time-decay histogram for these samples

are shown in Fig. 7.8d and e.

We prepared three RuSL samples by immersion in solutions with different concentrations and compared their lifetimes at three different wavelength ranges to investigate possible dependence with these parameter. For this we plotted the lifetimes obtained from the fits with respect to the surface concentration. The results are gathered in Fig. 7.8f. The inverse dependence of the lifetime with the concentration of the mother solution is evident. The most concentrated sample displays the shortest lifetime. This suggests that aggregation effects are relevant for this type of molecules. Stacking of molecules may cause overlapping of molecular orbitals, which facilitates the intercrossing of the excited electron to the triplet state.

This experiment demonstrated the capability of our microscope to perform time-resolved fluorescence measurements with compounds in the monolayer regime. With the development of PBIs this could mean an extraordinary advantage for distinguishing chelated and unchelated molecules based on the duration of the relaxation decay. Since the fluorescence emission of free PBIs would disappear in a few tens of ns, this would imply that detection of long-lived chelated PBIs could be background free.

7.6 Conclusions

A fluorescence microscope is being developed to detect the signal of molecular indicators (e.g. FBI or PBIs) in a monolayer. The microscope works in the diffractive limit and is mainly used as a spectrometer by using emission band filters. We measured spectra of FBI-G2SL deposited on quartz and ITO substrates by sublimation and spin-coating. For the latter method, the homogeneity on ITO is higher than on quartz, whereas sublimation yields similar results in both substrates. The emission of G2SL chelated with Ba^{2+} in solution was measured with the characteristic blue shift of 50 nm. However, when the chelation takes place in a dry atmosphere, the shift disappeared. This result requires further investigation but it was found thanks to this dedicated setup. Detection of the fluorescence signal in the final sensor in NEXT will be carried out with a microscope based on the one described in this chapter.

Additionally, time-resolved measurements can be carried out to characterize phosphorescent emission. The emission spectra and phosphorescent decay lifetimes of two inorganic molecules were measured this way: IrSL and RuSL. The lifetime was found to depend on the surface concentration of RuSL. These molecules work as proxies for Phosphorescent Bicolour Indicators, which could be used to detect the presence of Ba^{2+} without contribution from unchelated molecules.

8 Outlook and Conclusions

The future of understanding the origin of the material universe relies on fundamental research in particle physics, particularly in the area of neutrino research. The detection of neutrinoless double beta decay is a crucial step in determining the nature of neutrinos as either Majorana or Dirac particles. Background-free detectors, such as the barium tagging sensor proposed in this thesis, are essential in achieving the necessary sensitivity to detect $0\nu\beta\beta$ events with high precision and confidence. This type of research represents a significant challenge and requires the development of novel technologies and techniques. However, the potential impact of such discoveries on our understanding of the fundamental nature of matter is immense and may have profound implications for our understanding of the universe. As such, continued research in this field is critical to advancing our knowledge of the universe's origins and properties.

Throughout this thesis it has been demonstrated that a multidisciplinary approach combining knowledge from different fields, including chemistry, surface science, and optics, is essential for developing the proposed sensor. The complex nature of the sensing mechanism and the requirements of the experiment requires this broad range of skills. Thus, through our research, we have shown that specifically designed fluorescence molecules can chelate efficiently the desired Ba^{2+} ions in the absence of any solvent when immobilized on a surface. Different molecules of the family of the fluorescence bicolor indicator family have been tested. By combination of surface science techniques, their chemical and structural changes upon chelation in ultra-high vacuum conditions have been proven. This critical finding satisfies the first requirement for the proposed sensor, namely, the ability to immobilize and trap individual Ba^{2+} ions with high precision and

sensitivity. Overall, this research represents a significant step forward in the development of a reliable and effective barium tagging sensor, with implications for a wide range of applications in the field of neutrino research and beyond.

In addition to the promising results obtained with the chelating molecules, this thesis also represents the initial steps in the development of a specific microscope designed to detect single molecules via fluorescence imaging. The microscope developed in this thesis, although still in its early stages of development, has already shown significant potential in detecting the emission spectrum of molecules on a surface at the monolayer boundary. Our work has also allowed us to estimate the homogeneity of the coatings, and to detect small shifts in the emission spectra. These initial findings represent a significant step forward in the development of a robust and reliable sensing mechanism based on Single-Molecule Fluorescence Imaging. The microscope developed in this study showcases the potential of this technique to enable the high-precision detection and characterization of individual Ba^{2+} ions, as required by the proposed sensing mechanism. Moreover, the potential of this approach to enable the high-precision detection and characterization of individual Ba^{2+} ions holds great promise for advancing our understanding of the fundamental properties of matter, and for developing novel technologies with important practical applications.

In addition to the development of the sensing mechanism based on Single-Molecule Fluorescence Imaging, our research has also led to the development of novel and powerful tools with important implications for fundamental research in other fields. One such tool is the ALI system, which allows for the injection of liquid solutions into a vacuum environment without breaking the vacuum conditions. This innovation has important implications for a wide range of fields, including surface science, magnetism, and other areas of physics and chemistry where vacuum conditions are essential for accurate and reliable measurements. By enabling researchers to introduce liquid samples into vacuum environments without compromising the integrity of the experimental conditions, the ALI system opens up new avenues for research and discovery across a broad range of scientific disciplines. These findings demonstrate the potential for interdisciplinary collaborations and the development of new tools and techniques to

drive innovation and advance our understanding of the fundamental properties of matter.

Overall, while the primary focus of this thesis has been the initial progress in the development of a barium tagging sensor for NEXT, the findings and implications of this research extend beyond this specific field. This study provides a starting point for future investigations, highlighting a range of open questions that offer opportunities for further exploration across multiple domains. As an outlook summary, it is worth highlighting some of the key findings and areas of future research that have emerged from this thesis.

Surface science

This thesis focused on the research on FBI chelation with Ba^{2+}. However, the work carried out toward this goal also advanced the understanding of chelation of crown-ether derivatives on surfaces with other ions like Na^{+} and Fe^{2+}. Research on crown ethers is extensive in solution but not as much on ultra-high vacuum conditions. Crown ethers find other applications beyond barium-tagging and ion sensors, like drug carriers and photo-switching devices.

Moreover, the study of fluorescence from emitters deposited on surfaces is of interest for the field of surface science by itself. Developing expertise with these molecules could be useful for certain on-surface synthesis processes and photo-activated reactions. An example of on-surface synthesis is briefly discussed in this thesis for dehydrogenation of starphenes, deposited with ALI.

The XPS analysis presented in this thesis was performed entirely with a custom-made software written in Python. This software permits processing and analysis batches of several regions of the spectra, as well as several samples or experiments in a serialized, systematic way (scripting). The software is available for free at https://github.com/proscrite/xps_sw.

A deep understanding of the photochemistry of FBIs anchored on surfaces will be needed for the optimization of the final sensor. Some parameters like the packing or the distance between molecules on the surfaces or between the molecule and the substrate can determine for the overall efficiency of the sensor. The chelation efficiency and the capacity for the molecules to twist upon chelation and shift colour is

expected to depend on these parameters. Therefore, one crucial step is to understand how the molecules arrange themselves on surfaces and how the anchoring mechanism can affect their properties. STM measurements of FBIs can provide invaluable information in this regard, both for molecules laying flat on the substrate or standing still when bonded covalently through the anchoring group. However, STM is often performed on conductors like Au or Cu, which are not suitable for fluorescence microscopy. STM can be used on ITO [130], although with difficulty given the relative rugosity of this substrate. Atomic Force Microscopy (AFM) may be a more suitable technique, as it does not require the substrate to be conducting and can achieve resolution of close to 1 nm.

Another way to anticipate certain effects and understand others is through computer simulations. We have seen how simulations of the electronic structure of FBI-G1 explain the colour shift and the widening of the HOMO-LUMO gap (section 3.3.1), and how the chlorine atoms act as spectators in the chelation of $BaCl_2$. Dedicated simulations containing both the molecules and the substrate can also be carried out. These calculations account for interactions between the atoms of the surface and the molecule, so they can reveal information that simulations in vacuum cannot. To this end, we collaborated with Fernando Aguilar-Galindo from the Universidad Autónoma de Madrid, as an expert in molecular simulations in solid state. As a first approach he simulated the anchoring of aminopropyl-silatrane (APS) on quartz and ITO substrates. Since including the whole FBI molecule would complicate and delay the calculations, a proxy of it in the form of a phenyl ring coupled to APS was considered instead. The two groups were bonded by an amine bond, like in the case of G2SL. A sample of this system on ITO can be seen in figure 8.1. The DFT simulations were carried out with Vienna Ab initio Simulation Package (VASP) [131] software.

Different configurations of this system were simulated, with one, two and three covalent bonds between the silatrane legs and the surrounding OH groups and only physisorbtion on the surface. For two and three covalent bonds several possibilities exist and were considered independently. The relaxation energies of the system were calculated for each configuration and compared. The preliminary results point to forming two covalent bonds as the most stable config-

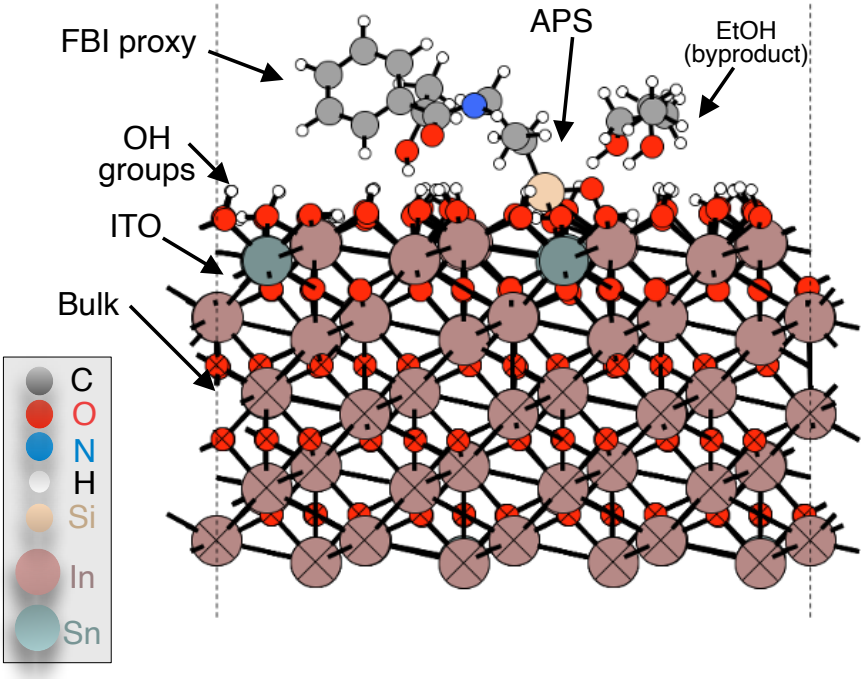

Figure 8.1. Visualization of the unit cell simulated in VASP. The FBI-proxy (a phenyl ring linked to APS) is covalently bonded to the OH groups on the ITO surface. Forming this bond causes ethanol (EtOH) to be detached from the silatrane and stays in the environment.

uration, and three bonds as the least stable. The implications of this results will be discussed as well as how to extend the calculations to account for the full molecule and in different scenarios of interest for the experiment.

Microscopy

Focusing the laser beam into a diffraction-limited spot enables detection of fluorescence emitted from an area of $\sim 1\ \mu m^2$. However, for identification of a single chelated molecule in a sensor spanning several millimeters, wide-field microscopy can help scanning larger areas at once. Wide-Field (WF) microscopy has been used to detect fluorescence of single-molecules chelated with Ba^{2+} using Total Internal

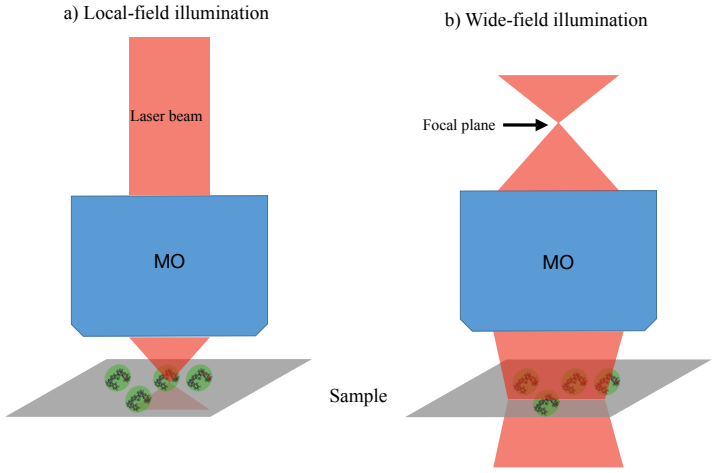

Figure 8.2. Scheme of local-field illumination (**a**) and wide-field illumination (**b**).

Reflection Fluorescence [132]. Switching from a local-field configuration in our setup (Fig. 8.2a) to a WF configuration is relatively straight-forward: instead of introducing the collimated laser beam through the back port of the MO, we can use a lens to focus it on the focal plane of the back port (Fig. 8.2b). We are developing a WF illumination setup parallel to the local-field one, with the set of band-pass filters to map the fluorescence spectrum in larger areas. The final version of the microscopy setup may require integrating both local- and wide-field illumination configurations, which poses a challenge but has been achieved already [133].

Advances in molecular design and synthesis may lead to different optimal excitation wavelengths. A super-continuum laser [134] may help decoupling this changing requirement. The excellent signal-to-noise ratio demanded by the requirement of single-molecule detection may require excitation by Two-photon absorption (2PA). Impurities in quartz can produce background fluorescence at short wavelengths [135]. This background could be mitigated by exciting the system with a laser capable of inducing 2PA: the extremely low cross-section for 2PA processes causes the effective emitting volume to be much smaller than for single-photon absorption (SPA). Most of the background from

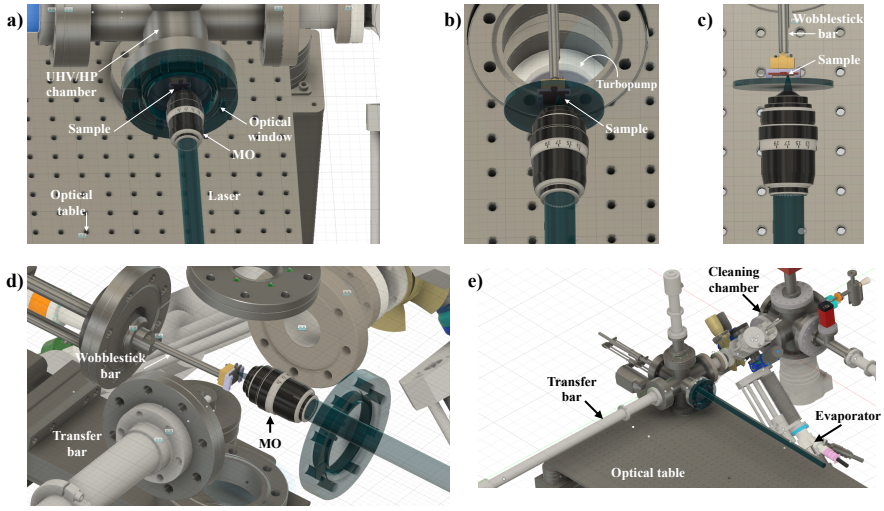

Figure 8.3. Possible implementations of a high-pressure microscope. **a)-c)** MO outside the chamber, view with all components (**a**), front view (**b**) and bird's-eye view (**c**) with the walls of the chamber and the body of the optical window hidden. **d**) MO inside the chamber, with MO holder hidden. **b**) Full view of a simple barium evaporation and HP-microscopy setup.

quartz is expected to come from the few layers immediately below the surface containing FBIs. Since 2PA reduces this thickness, the background would be drastically reduced while it would be essentially unaffected for FBIs.

A crucial next step in the development of a barium-tagging device is the assembly of a high-pressure microscope. This would assure experiment conditions very similar to the final implementation in NEXT. The basic requirement then is to keep the molecular sample inside a high-pressure (HP) vessel. Initially, two designs are possible: keeping the Microscope Objective (MO) inside or outside the HP chamber. Two simple implementations of a HP microscope following these schemes is shown in figure 8.3. If the MO is mounted outside the chamber, it needs to be able to focus the beam onto the surface sample (see Fig. 8.3c). This in turn requires the MO to have a long working distance, as the glass of the optical window must fit in this distance. The thickness of CF viewports is usually 5-7 mm. Microscope objectives for use in air with high enough numerical aperture (NA) and working distances in

the order of 10 mm are available in the market. It is worth considering some buffer millimeters to accommodate the sample holder. This distance would have to be corrected for the refraction on the two surfaces of the window. Taking all this into account, this scheme is feasible.

Mounting the MO inside the pressure chamber (Fig. 8.3d) would require the use of a pressure-compatible piece. Ordinary MOs can burst when the chamber is evacuated to UHV conditions, so they must be adapted mechanically for use in high or low pressures. This usually involves drilling holes through the objective housing to facilitate the evacuation of air between the lenses. Degassing from the cement holding the lenses inside the MO must be avoided too.

Figure 8.3 features a simple wobble-stick working as sample holder. However, accurate focusing of the beam on the sample surface requires fine manipulation in the beam axis. A vacuum stage system with sub-micrometer precision is mandatory for focusing and scanning. Alternatively, the MO could be displaced along the beam axis for focusing, although this would introduce extra mechanical requirements, especially if is placed inside the chamber. Scanning could also be achieved without moving the sample, through the use scanning galvo mirrors and scan lenses. The HP microscope can be a module of a larger setup in which the sample can be prepared in-situ, as illustrated in Fig. 8.3e. A molecular evaporator, a barium evaporator are mounted in a module adjacent to the microscope chamber. A cleaning module for preparation of the substrate is located in the far end of the setup. The evaporation and cleaning techniques require ultra-high vacuum (UHV), whereas the microscope is intended to work under high pressure. A full design would then require differential pumping to transfer the sample from the UHV modules to the HP ones.

A design based on the one presented is a mandatory step forward in the development of BOLD. The NEXT collaboration is working toward developing a HP microscope and a finely-controlled source of Ba^{2+}. This apparatus will be sketched in section 8.

Barium sources

The next step will be to establish a proof of chelation with single Ba ions. A Ba^{2+} beam is being developed for this purpose by Prof. Lior Arazi's group of Ben-Gurion University, who is also part of NEXT.

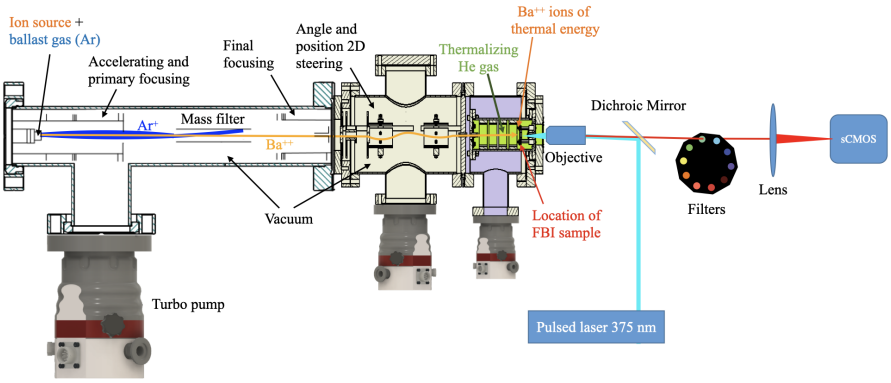

Figure 8.4. Scheme of RITA. From left to right: Barium beam chamber, composed of ion source, mass filter, focusing, 2D steering components and thermalizing gas chamber. The Ba^{2+} ions reach the right side of the chamber with thermal energy. FBIs are located on this end and are imaged by the optics system through the substrate. The fluorescence is collected by the objective, filtered chromatically and detected by the sCMOS.

In addition, a HP microscope will be coupled to this barium beam chamber. Prof. Itay Shomroni is spearheading the design of the microscope as an expert in optics and metrology. This apparatus will emulate closely the conditions of the final experiment in NEXT, as it will feature single Ba^{2+} ions reaching the sensor in high pressure and the fluorescence will be detected in-situ through an optical window. The general scheme of this setup is shown in Figure 8.4 . The Ba^{2+} ions will be filtered by its mass-to-charge ratio, cooled to thermal energies by differential pumping and driven toward a target containing a monolayer of FBIs. This will allow testing the chelation at different pressures and different energies.

In parallel, a single Ra^{2+} beam is being developed too. Ra is an ideal surrogate of Ba, as they are both heavy alkaline earth metals, so it can be used to calibrate the sensor. Individual Ra^{2+} ions from radioactive decay of ^{228}Th can be tagged by detecting the backward-emitted alpha particle. The target sample will then be measured by an alpha spectrometer to determine its ^{224}Ra activity. Radium Ion TAgging (RITA) could have further applications: identifying trace amounts of Ra or single ions could potentially improve current sensitivities of radiation detection methods like germanium detectors. Furthermore,

including a Ra source in NEXT could be used to calibrate the Ba-sensor.

The machines in the RITA program will allow to characterize chelation efficiency and assess the system overall efficiency to detect single-barium ions. The outcome of RITA will be the first demonstration of single Ba^{2+} chelation, and would be a major milestone in NEXT, and in neutrino physics in general. Once the development of the sensor and the detection techniques are sufficiently mature, a first prototype called BOLD-0 will be deployed. BOLD-0 will be a small-scale version of the full NEXT-BOLD design presented in section 2.5.

A1 *In-situ characterization: Surface Science Techniques*

In this chapter we introduce the experimental techniques used throughout this thesis concerning surface science. In the first two sections I will introduce two techniques used for deposition of molecules on surfaces in ultra-high vacuum: Molecular Beam Epitaxy (MBE) and Atomic Layer Injection (ALI). The three next sections are a summary of the main surface science techniques used for characterisation of these system. They aim to study the chemical and structural properties of molecules in surfaces. The first technique is X-ray Photoelectron Spectroscopy (XPS), and it provides information of the core levels of each element and its chemical environment. The second technique is Scanning Tunneling Microscopy (STM), which provides structural information on molecules and supramolecular systems on surfaces in the form of a 2D map of electronic equipotential surfaces. The third technique is Near Edge X-ray Absorption Fine Structure (NEXAFS), and it yields information about the spatial distribution of molecules on the surface.

All these techniques are used in the ultra-high vacuum (UHV) regime, in a pressure range between $10^{-7} - 10^{-11}$ mbar. In this range, particles in a volume move in molecular flow, without any mutual hindrance. Furthermore, the monolayer (ML) time in the UHV regime is in the order of minutes or hours. This is the time scale necessary for a single molecular or atomic layer to be absorbed on a gas-free surface. For pressures above the UHV regime, this time is in the range of a fraction of a second. Therefore, in the UHV regime the purity of the surfaces during the characterisation time is sufficiently preserved. In addition, the scattering of photoelectrons due to air molecules is minimised, which is optimum for the measurement of the photoelectron current.

The final detection of the fluorescence signal will be carried out by optical microscopy, so these techniques requires its own dedicated setup. The development of a fluorescence microscope and the results obtained with it throughout this thesis will be presented in chapter 7.

A1.1 Molecular Beam Epitaxy

Molecular beam epitaxy (MBE) is the technique used to grow thin films of various materials layer by layer. It is consider the cleanest technique for material growth. A typical MBE experimental setup is shown in Figure A1.1. The material to be deposited is contained in ultra pure solid form (i.e. 99.99% pure compounds) in a Knudsen effusion cell. These cells are placed on a UHV chamber facing a sample holder with the target substrate. The cells are heated to the appropriate temperatures at which the material sublimates and the vapor from the cell diffuses toward the substrate. The deposition time may be controlled by opening and closing a mechanical shutter and the rate can be adjusted by varying the temperature of the cell. Deposition of materials on a surface may be aided by heating or cooling the substrate. Coevaporation of two or more materials is possible by using two or more effusion cells. Several factors determine the final composition of the film: the flux of the individual molecular beams, the temperature and atomic structure of the substrate and the chemical and physical interaction between the material and the substrate.

The uniformity of the layers can be improved by rotating the substrate slowly (1 rpm). Quartz microbalances are often used to measure the growth rate in situ. In addition, Reflection High-Energy Electron Diffraction (RHEED) is usually used to characterise the sample structure and thickness. The typical MBE growth rate is in the ML/s range, although it can be much slower for species with poor sticking coefficients in a specific substrate.

A1.2 X-ray Photoemission Spectroscopy

X-ray Photoemission Spectroscopy (XPS) or Electron Spectroscopy for Chemical Analysis (ESCA, both acronyms are used interchangeably) is a widely used technique for chemical analysis in surfaces. This section

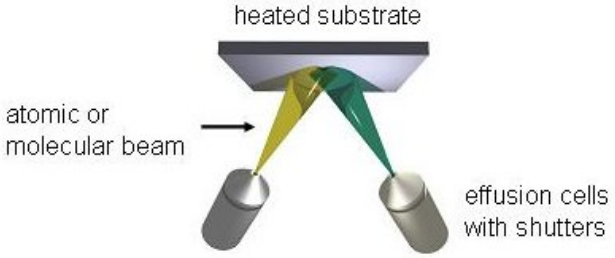

Figure A1.1. Basic principle of molecular beam epitaxy: two beams of molecules or atoms are coevaporated from different sources (effusion cells) and deposited onto a heated substrate.

is a short overview of the principle, instrumentation and information yielded by the technique. For further reading about the topic, we refer to the following reviews [136–138].

XPS was developed for chemical analysis during the 1950s and 1960s by Kai Siegbahn, who received the Nobel Prize in Physics in 1981 for this contribution. The technique is based on the photoelectric effect, as illustrated on figure A1.2a. An X-ray photon transfers its energy $h\nu$ to an atomic electron in the core level 1s and ejects it from the atomic shell. The Einstein equation describes the kinetic energy of this electron E_K as a function of the photon energy:

$$E_B = h\nu - E_K, \tag{A1.1}$$

where E_B is the binding energy of the electron in the atom. The binding energy depends on the type of atom and its chemical environment. Therefore, measuring the kinetic energy of the electrons yields valuable information about the composition and chemical environment of a given sample. The binding energy of a gas identical to its first ionisation potential. In solids, the surface acts as an additional barrier that the electron has to overcome to reach the free electron level. This energy is referred to as work function, as indicated in figure A1.2. Conducting materials in electric contact with a spectrometer have the Fermi level at the same energy level. The spectrometers have a well-known work function $\Phi_{sp} \sim 5$ eV. Thus, for conducting materials, eq. A1.1 can be written as

$$E_B^F = h\nu - E_K + \Phi_{sp}, \tag{A1.2}$$

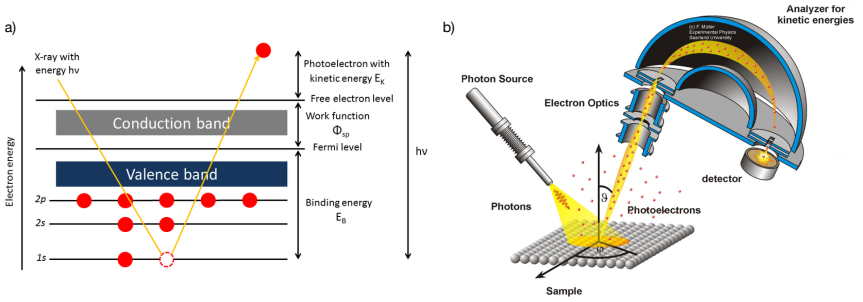

Figure A1.2. a) Schematic basic principle of X-ray photoemission. b) XPS setup is composed of a X-ray photon source, a vacuum manipulator to hold and move the sample, an analyzer and an electron detector. See text for more details. Figure adapted from [139]

where E_B^F is the binding energy referred to the Fermi level. For insulators, the binding energy is usually referred to an internal reference. For example, the hydrocarbon (C-C / C-H) component of the C 1s peak is typically set to 285.0 eV.

A typical schematic drawing of a XPS instrument is shown in figure A1.2b. The main components are the X-ray photon source, the analyzer and the detector. The X-rays are irradiated on the sample, causing photoelectrons to be emitted and collected by electron optics. An electron lens then guides the photoelectron into the analyzer, in which electrons with a specific kinetic energy are selected and finally detected. The XPS spectrum is obtained by varying the selected kinetic energy and measuring the photoelectron current detected for each energy value. The whole experiment usually takes place in UHV for three reasons: first, the photoelectrons can travel without colliding with gas particles; second, the X-ray sources require vacuum condition to operate and third, the composition of the sample takes longer to degrade in UHV.

The XPS measurements in this thesis were carried out using a Phoibos-100 electron analyzer (SPECS GmbH), using a non monochromatic Al Kα photon source of 1486.6 eV. The spectra were calibrated to the substrates main core level (for example Au $4f$ for Au(111)).

X-rays sources usually consist on an anode made of a target material like Mg or Al which is irradiated by a high-energy (10 keV) electron beam. The atoms of the target anode then produce fluores-

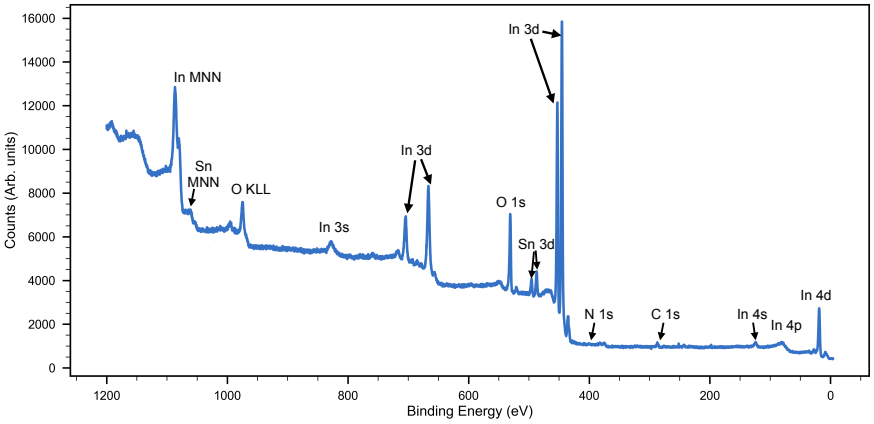

Figure A1.3. XPS spectrum of Indium Tin Oxide (ITO) with labels of the main core level transitions. The photon energy is 1486.6 keV (Al K$\alpha_{1,2}$).

cence X-rays and electrons. Synchrotron radiation can also be used as a highly collimated and polarized source for XPS. Using a monochromator, a broad range of X-ray energies (from infrared to hard X-rays) can be used for photoemission experiments. Synchrotron light can produce sample degradation due to its high intensity. The most widely used type of analyzer in XPS experiments is the hemispherical electron energy analyzer. It consists of two concentric hemispherical electrodes held with a voltage across them. The voltage of the analyzer is held fixed, while the electron lenses are swept to scan at different energies. The detection can be parallelized by using several discrete electron detectors (channeltrons) or microchannel plates.

Photoelectrons from elastic scattering do not lose any energy in the transport through the solid and yield sharp, nearly symmetric peaks in the energy spectrum. These peaks correspond to the core levels of the different elements: C 1s, Cl 2p, Ba 3d, etc. An example of XPS energy spectrum is shown in figure A1.3. An asymmetric background appears in this spectrum as a step on the high binding energy tail. This background corresponds to inelastic scattering and a continuous Bremsstrahlung contribution.

The peaks in the spectrum appear as singlets (s orbitals) or doublets (p, d and f orbitals). The latter are degenerated, as several states have the same energy. The double peak structure is due to spin-

orbit coupling or $j-j$ coupling (after the total quantum momentum $j = l + s$): the spin interacts magnetically with the angular momentum, splitting the energy levels. This splitting can be of several electron volts and depends on the specific element and orbital. The anti-parallel spin configuration is more stable, so the peak corresponding to lower j always has higher binding energy. The degeneracy $2j + 1$ determines the intensity of the components. For example, for a p orbital, the degeneracy of $d_{5/2}$ and $d_{3/2}$ levels is 3 and 2, respectively, so the ratio between the areas of these components is 3 : 2.

The binding energy depends on the type of target atom and the presence of other atoms bonded to it, as these bonds affect its electronic structure. Therefore, shifts of the binding energy are directly related to information about covalent, ionic and coordinated bonds.

A1.2.1 Surface sensitivity

X-rays with around 1 keV can penetrate around 1 μm through the bulk of solids, but photoelectrons with the same energy can travel only around 10 nm. This means that only electrons from the few top layers contribute to the photoemission peaks in XPS as illustrated in figure A1.4. Electron attenuation by an overlayer is described by the Beer-Lamber law:

$$I_z = I_0 \exp\left(\frac{-z}{\lambda \sin\theta}\right) \tag{A1.3}$$

where I_z is the intensity of electrons emitted from the atoms in a depth z, I_0 is the electron intensity emitted from the surface, θ is the take-off angle of the electrons from the surface and λ is the elastic attenuation length (EAL). The EAL is a parameter obtained in base to the inelastic mean free path (IMFP) [97]. The IMFP is the average distance an electron can travel between inelastic scatterings. The thickness z of a layer A deposited on a substrate B may be estimated by comparing the peak area of a core level from the clean substrate with the same (attenuated) peak after depositing the layer A.

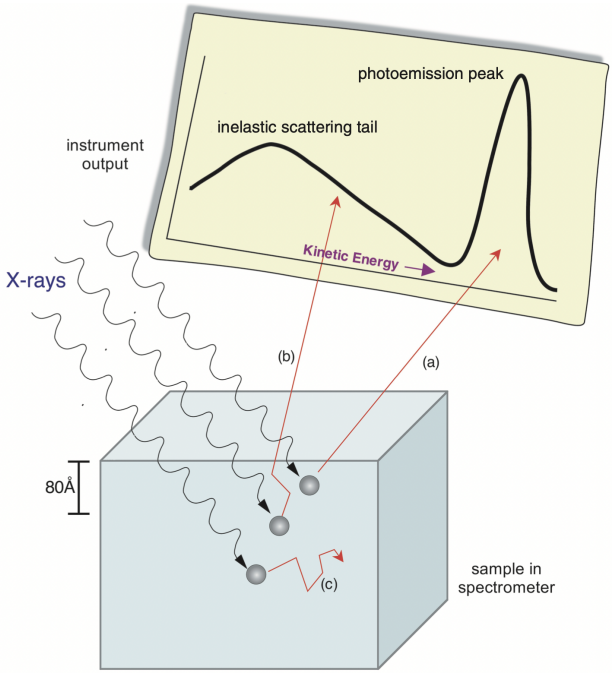

Figure A1.4. Surface sensitivity of XPS: only electrons from the outermost layers (a) can escape from the solid, whereas electrons at intermediate depth scatter inelastically (b) and contribute to the background or do not escape from the bulk (c). Taken from [138].

A1.2.2 Quantification

The abundance of each element in the outermost layers of a sample can be estimated by analysing the corresponding XPS peaks. Assuming that the concentration of the elements are homogeneous within the sampling depth, the photoemission intensity of the orbital X of element A is

$$I_A(X) = n_A F \sigma_{A,X} \lambda_A y T \theta = n_A S, \tag{A1.4}$$

where n_A is the number of atoms of element A per volume unit, F is the X-ray flux, $\sigma_{A,X}$ is the photoelectric cross section for the orbital X of that element, λ is the mean free path of photoelectrons in the sample, y is the efficiency of in the photoelectric effect, T is the detection efficiency and θ is an angular efficiency factor. The atomic sensitivity

factor S encompasses all these factors and is available in the literature [104, 140, 141].

Quantification in XPS analysis is usually performed by comparing the concentration of different elements in the samples:

$$\frac{n_1}{n_2} = \frac{I_1/S_1}{I_2/S_2}, \tag{A1.5}$$

as the ratio S_1/S_2 is matrix-independent for all materials.

A1.3 Scanning Tunelling Microscopy

Scanning Tunnelling Microscopy (STM) is a technique used to image surfaces at the atomic level. This technique allows for a lateral resolution of 10 pm and a vertical resolution as low as 1 pm, so features smaller than 100 pm can be distinguished. STM is based on the quantum tunnelling effect: a very sharp metallic tip is brought to a distance of ∼5-10 Å from a conducting surface and a bias voltage is applied between the two so that the electrons *tunnel through* the vacuum separating them. A tunnelling current travels through the vacuum gap and can be used to control the distance between the surface and the tip with high precision. Changes of 1 Åin the gap distance typically cause the tunnelling current to decrease by an order of magnitude.

The physical process of quantum tunnelling can be best understood in the one-dimensional case, as shown in figure A1.5. The wave function of a free electron in the sample is damped exponentially by crossing to the STM tip through the potential barrier of width s and height Φ, corresponding to the effective local work function, i.e. the energy to bring the electron from the sample electrode to the vacuum level. E_F are the Fermi levels of the metal electrodes.

A scheme of an STM setup is shown in fig. A1.6a. The main components are the tip and the feedback control, which regulates the distance to the sample based on the changes of the tunnelling current. Movements in the $x-$, $y-$ and $z-$directions are controlled by piezoelectric crystals, which contract or expand in a well defined manner when a potential is applied on them. Either the tip or the sample may be mounted on this crystals.

An STM can be operated in two imaging modes: constant current and constant voltage. In the constant voltage mode, the bias voltage

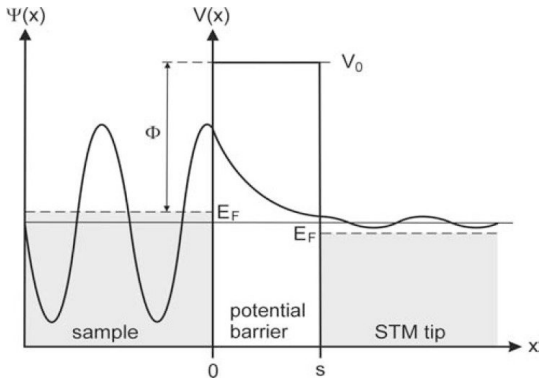

Figure A1.5. Illustration of the quantum tunnelling effect. The wave function of a free electron in the sample is damped exponentially by crossing to the STM tip through the potential barrier of height Φ. This height is the effective local work function, i.e. the energy to bring the electron from the sample electrode to the vacuum level. E_F are the Fermi levels of the metal electrodes and s is the barrier width. Taken from [142].

between the tip and the sample is held at a constant value as the tip scans over the surface. Along this scan, the variation of the measured tunnelling current with the position can be translated into an image. The most common mode of operation is constant current mode. In this mode, the tunnelling current is measured at each point and the bias voltage is adjusted via a feedback loop so that the current is held at a constant value. Then, the variations of the z-voltage with the x, y coordinates yield the STM image. These variations of the z-voltage are translated into changes of the height, and the contour map in x, y approximates the topography of the surface. An example of STM image with intramolecular resolution can be seen in figure A1.6b, corresponding to the model of a hexafluorene (Fig. A1.6c).

STM experiments shown in this thesis were performed with a commercial Scienta-Omicron ultra-high vacuum LT-STM at 4.3 K. A W-tip was used. Topography images were measured using constant current mode, while for bond resolution images constant height mode was used. During the STM experiments, the tip was functionalized with CO for bond resolution STM by exposing the sample to low pressure (approximately 1×10^{-8} mbar) of CO whilst the sample was held below 7 K. CO molecules were trapped by the tip from their

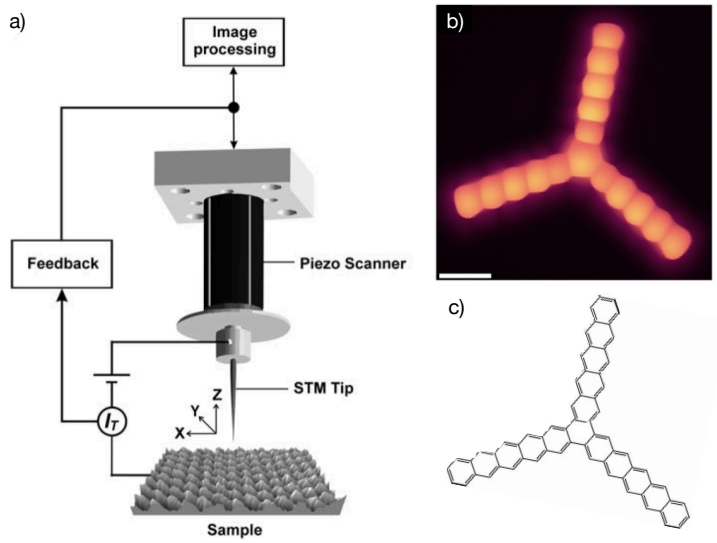

Figure A1.6. a) Scheme of an STM setup. The tip scans in the $x - y$ plane and the feedback keeps the tunneling current constant by regulating the distance to the sample. The movements in all three axis are controlled by piezo drives. Taken from [142]. b) Example of an STM image of a starphene molecule with bond resolution, the white bar on the lower left corner indicates a scale of 1 nm. Taken from [93]. c) Model of starphene molecule.

adsorption sites via scanning over them or by applying ~ 2 V bias voltage pulses.

A1.3.1 Scanning Tunnelling Spectroscopy

STM images depend on the bias potential applied, so this technique can be used to obtain spectroscopic measurements of materials with atomic resolution. A positive bias is defined as a negative potential of the tip with respect to the sample. In this case, electrons tunnel from occupied states of the tip to unoccupied states of the sample. In other words, the tip "injects" electrons into the sample. In the opposite case, a positive tip potential with respect to the sample causes electrons to tunnel from occupied states of the samples to unoccupied states of the tip. Thus, the tip "extracts" electrons from the sample.

Scanning tunnelling spectroscopy (STS) is performed by varying the bias voltage at which the STM images are recorded. Different

reconstruction structures can be imaged with negative potential biases with respect to those imaged at positive biases. Tunnelling spectra are obtained by measuring locally the variation of the tunnelling current I with respect to the variation of the bias voltage V. With a fixed tip position and separation, I-V curves are obtained. The tunneling conductance $\mathrm{d}I/\mathrm{d}V$ is directly proportional to the sample Local Density of States (LDOS) ρ_S:

$$\frac{\mathrm{d}I}{\mathrm{d}V} \propto \rho_S\,(E_F - eV). \tag{A1.6}$$

Local conductance of the sample can be inferred from STS. Figure A1.7 shows the typical $\mathrm{d}I/\mathrm{d}V$ profiles for metals, semi-metals, semiconductors and insulators. Metals and semi-metals do not have a gap between occupied and unoccupied states, so the I-V curves are mostly linear. For semi-metals, there is a gap in the momentum space (the waves are out of phase) so the conductance around the Fermi level decreases, and bends the density of states at low voltages. The conductance around the Fermi level of semiconductors and insulators is zero. For semiconductors, the band gap, $E_g = |V_{+\mathrm{bias}}| + |V_{-\mathrm{bias}}|$, is relatively small, so the LDOS is highly bent. The LDOS is flat as for insulators and energy gap E_g cannot be bridged.

A1.4 X-ray Adsorption Spectroscopy

Several methods of X-ray adsorption spectroscopy (XAS) are used in surface science to obtain chemical and structural information of molecules on surfaces. X-ray adsorption involves electron transitions into unoccupied states, which can be probed with these techniques. Measuring spectra of X-ray absorption requires varying the photon energy, so the technique is performed in synchrotron radiation facilities.

The X-ray absorption spectrum is usually divided in two regions: the range up to around 50 eV above the absorption edge is known as Near Edge X-ray Absorption Fine Structure (NEXAFS) —or, equivalently, X-ray Absorption Near Edge Structure (XANES); and the range above 50 eV until several hundred eV is known as Extended X-ray Absorption Fine Structure (EXAFS). The latter yields information about local coordination distances and is due to interference effects in the wave function of the excited electron. We focus on NEXAFS as it pro-

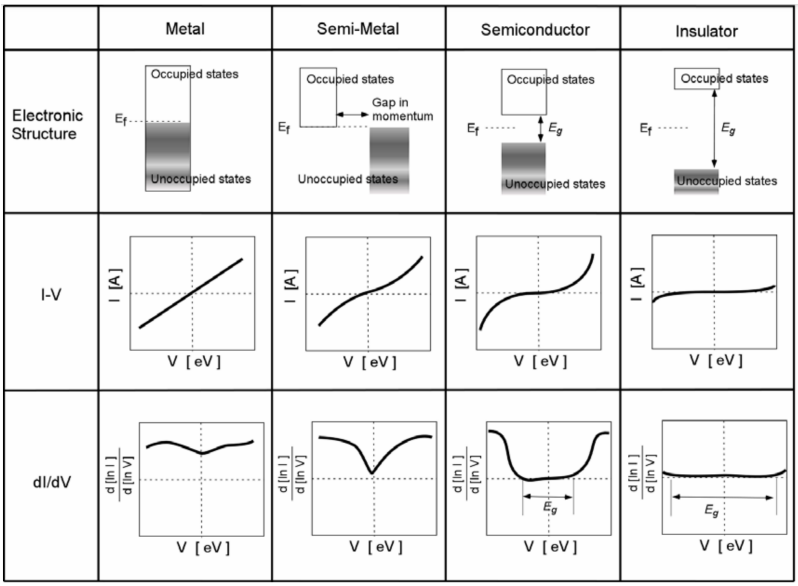

Figure A1.7. Electronic structures and corresponding I-V curves and $\mathrm{d}I/\mathrm{d}V$ curves of tunnelling spectroscopy. Taken from [143]

vides information on the chemical environment of single elements and their coordination geometry.

A scheme of the typical NEXAFS spectrum can be seen in figure A1.8 (left, top). The structure of this spectrum can be best understood by studying a model of the occupied and unoccupied states of a diatomic molecule as in fig. A1.8 (left, bottom). σ- and π- molecular orbitals are filled states, whereas σ^*- and π^*- are unfilled states. If the incoming photon energy matches exactly the difference between an initial state and an unoccupied molecular state the transition takes place, producing the peak in the absorption spectrum.

NEXAFS can be used to investigate the nature of the molecular bonds and their oxidation states. The latter determines the position of resonance peaks, in the same way as in XPS. Figure A1.8 (right) shows three NEXAFS spectra at the C K-edge region of acetone adsorbed on CeO_2(111)/Ru(0001) in different conditions: (A) multilayer acetone (60 L) deposited at 95 K, (B) 5 L acetone at 95 K then annealed to 175 K and (C) 8 L acetone on reduced $CeO_{1.75}$(111) annealed to 300 K. The two main peaks at 286.2 eV and 289 eV in all three cases correspond

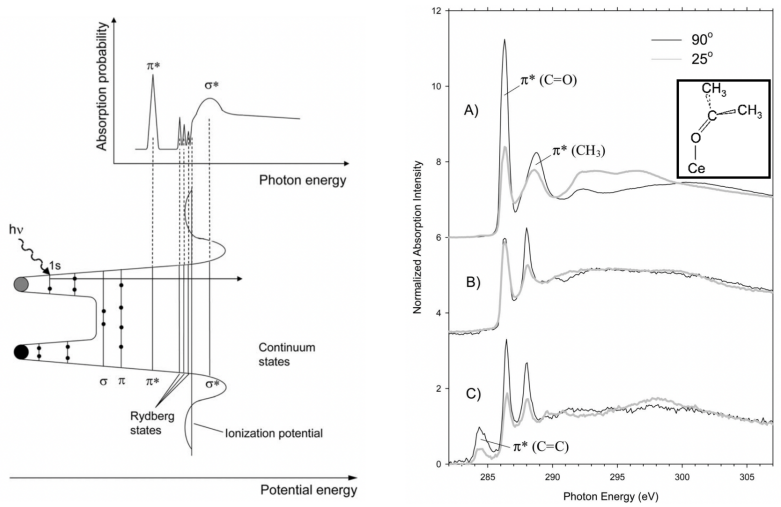

Figure A1.8. (Left): Schematic potential (bottom) of the K-edge states of a diatomic molecule and the resulting structure in the NEXAFS spectrum (top). Taken from [144]. (Right): NEXAFS on the C K-edge of acetone adsorbed on CeO_2(111) (Inset) showing different π* peaks components (C=O, CH_3 and C=C), at different preparation and annealing temperatures. Taken from [145].

to the C=O and CH_3 environments, respectively. In (C) an additional π^* resonance appears at 284.5 eV, corresponding to C=C bonds, from interaction between the acetone and the reduced ceria surface. All spectra were recorded at normal (black line) and grazing incidence (gray line).

The X-ray absorption depends on the polarization of the incoming photon, which can be used to study the orientation of molecules on surfaces. This dependence is evident on fig. A1.8 (right), in particular in the spectrum (B). The (C=O) resonance is the same at normal and grazing angles, whereas this is not the case for the CH_3 resonance. This indicates that the molecular plane is tilted away from the surface normal, as shown in the inset of the figure.

The variation of the NEXAFS structure with the light polarization can be studied by rotating the sample to change the angle between the electric vector and the surface. The molecular orbitals in the sample present high directionality, as shown in figure A1.9, so different resonances appear when the electric vector is parallel to the molecular

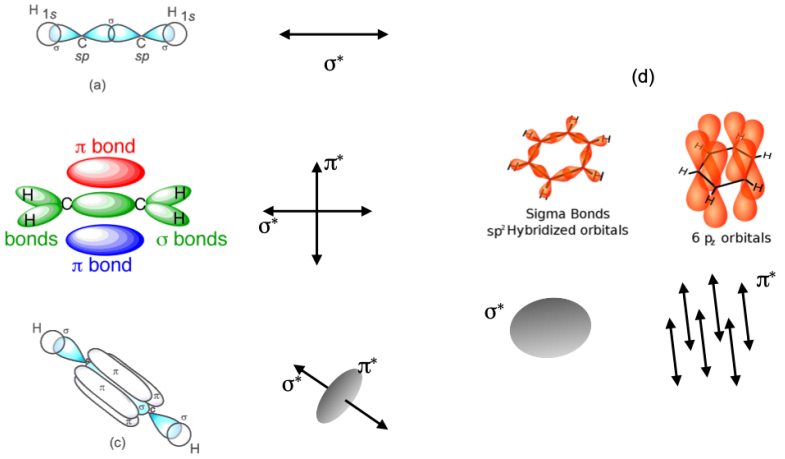

Figure A1.9. Geometric models of molecular orbitals: (a) single σ bond (H-C-C-H) between hybridized sp orbitals, (b) double π bond between hybridized sp^2 orbitals, (c) triple $\sigma - \pi$ bond from hybridized sp^3 orbitals, (d) σ- and π-bonds from sp^2 and p_z orbitals, respectively, in an aromatic ring.

orbital vectors and planes.

XAS experiments require high-brilliance, polarized X-ray sources and the capacity to vary the photon energy. Therefore, these experiments are carried out in synchrotron radiation facilities. Synchrotron radiation is produced by charged particles traveling at relativistic speeds in curved paths. Dedicated facilities operate storage rings where electrons (or positrons) circulate at constant energy to produce this radiation. The X-rays are emitted tangentially to the electron orbit with an opening angle in the order of ~ 1 mrad and extracted into a beamline for use in different X-ray experiments. A scheme of a typical beamline is shown in figure A1.10. The X-rays extracted from the storage ring interfere coherently in an undulator and the particular wavelength of interest is selected by a monochromator. The X-ray spectrum ranges from the far infrared to the hard X-ray region, so the monochromator is used to tune across a defined range for each particular technique.

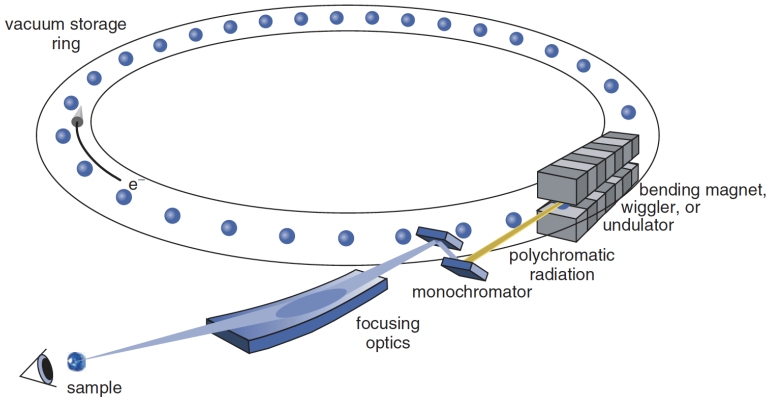

Figure A1.10. Schematic of a typical X-ray beamline at a synchrotron radiation facility. Radiation from an insertion device (bending magnet, wiggler or undulator) is extracted into the beamline and filtered by wavelength by a monochromator. The beam is then focused into the sample to perform X-ray experiments. Taken from [146].

A2 *Ex-situ characterization: Fluorescence measurements*

A2.1 Two-Photon Adsorption Microscope

The Two-Photon Adsorption Microscopy experiments conducted in this thesis were carried out in collaboration with the group of Prof. Pablo Artal and Prof. Juan Manuel Bueno from the Laboratorio de Óptica (LOUM) & Centro de Investigación en Óptica y Nanofísica (CiOyN), University of Murcia (UM). We took advantage of the fact that the emission spectra of the FBI and FBI Ba^{2+} for an excitation light of 250 nm and of 400 nm are very similar and used a mode-locked Ti:sapphire infrared laser (800 nm) as the illumination source, inducing the absorption of two photons of 400 nm each. This laser system provided pulses of infrared light with a repetition rate of 76 MHz. The pulse duration was 400 fs on the sample plane.

The beam was reflected on a dichroic mirror, passed a non-immersion objective (20×, NA = 0.5) and reached the sample, illuminating a spot limited by diffraction to a volume of about 1 μm^3. A d.c. motor coupled to the objective allowed optical sectioning across the sample along the Z direction. This image modality is known as $Z - X$ tomographic imaging and we call these tomographic images 'profiles'. In addition, we obtained 3D tomography images, which were assembled from 40 $X - Y$ scans of 75 μm × 75 μm. Each scan corresponded to a different depth Z, in steps of 10 μm. The resulting images were then combined in a 3D image. The emitted light was collected through the same objective and passed the dichroic mirror. Finally, before reaching the photomultiplier tube used as the detection unit, the TPA signal passed through either a high-pass, green filter with $\lambda > 450$ nm, or a band-pass deep-blue filter of (400, 425) nm.

We performed tomography using two filters: a high-pass 'green' fil-

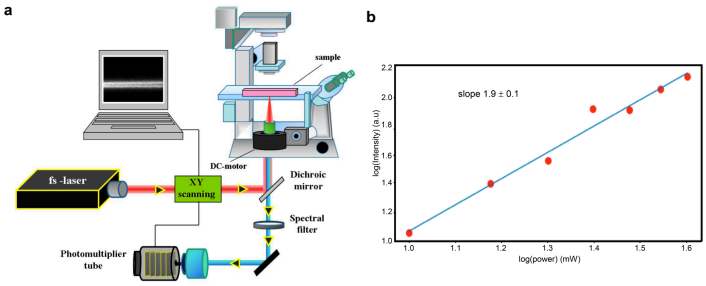

Figure A2.1. Two-Photon Absorption (2PA) Microscopy setup. **a**, Illustration of our setup. An infrared (800 nm) laser passes through a dichroic mirror and fills the back plane of the objective (20×, NA = 0.5) of an inverted microscope. The laser is focused in the sample, with a spot limited by diffraction (for example, a volume of about 1 μm^3). The emitted fluorescence passes through a selection filter before being recorded by a PMT. **b**, Log-log plot showing the quadratic dependence of the intensity on the power, which is characteristic of TPA.

ter with $\lambda > 450$ nm and a band-pass 'deep blue' filter with wavelength (400, 425) nm. The $Z - X$ scans were performed with infrared light (800 nm) at a nominal laser power of 100 mW. In addition, we obtained three-dimensional (3D) tomography images, which were assembled from 40 $X - Y$ scans of 75 μm $\times$ 75 μm. Each scan corresponded to a different depth Z, in steps of 10 μm. The resulting images were then combined in a 3D image using custom software [147].

A2.2 Fluorescence Spectroscopy

The continuous emission spectra of solutions and solid samples were acquired on an Edinburgh FLS-1000 Fluorescence Spectrophotometer. This light source used for excitation is a xenon arc lamp, which emits continuous (incoherent) radiation from 230 nm to 1500 nm. A μs Flashlamp producing pulses up to 100 Hz in the same spectral range is also available but was not used. The excitation wavelength is filtered by a Czerny-Turner monochromator with a resolution lower than 0.1 nm. The excitation light is focused on the sample by a lens. Since the light is non-coherent, the axial resolution of the focused spot is limited to the range of mm. The sample is oriented in a 90º angle geometry

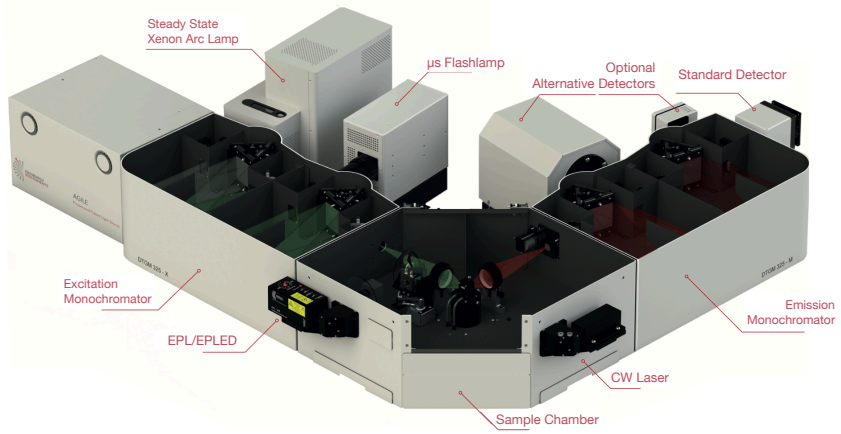

Figure A2.2. Scheme of the fluorescence spectrophotometer used to acquire emission spectra. The main subelements are labelled. EPL/EPLED: Edimburgh Pulsed Laser/LED. CW Laser: Continuous Wave Laser. Taken from [148].

to avoid detecting reflections from the excitation light. The fluorescence emission is then collected by a lens, filtered by the emission monochromator and detected by a PMT with a wavelength coverage of 185-900 nm. For the measurements presented in this theses, the monochromator bandwidth of excitation and emission was fixed at 5 nm.

Using a PMT as detector also allows to perform Time-Correlated Single Photon Counting (TCSPC) or Time-resolved fluorescence measurements. A pulsed laser or LED (EPL/EPLED) is used for these measurements to reach a lifetime resolution of the order of picoseconds.

Bibliography

[1] C. McDonagh, C. S. Burke, B. D. MacCraith, *Chemical Reviews* **2008**, *108*, Publisher: American Chemical Society, 400–422.

[2] O. S. Wolfbeis, *Journal of Materials Chemistry* **2005**, *15*, Publisher: The Royal Society of Chemistry, 2657–2669.

[3] E. Majorana, *Il Nuovo Cimento (1924-1942)* **2008**, *14*, 171.

[4] E. Majorana, *Nuovo Cim.* **1937**, *14*, 171–184.

[5] A. D. Sakharov, *Pisma Zh.Eksp.Teor.Fiz. 5 32-35* **1967**.

[6] M. Fukugita, T. Yanagida, *Phys. Lett.* **1986**, *B174*, 45–47.

[7] M. Gell-Mann, P. Ramond, R. Slansky, *Conf. Proc.* **1979**, *C790927*, 315–321.

[8] T. Yanagida, *Conf. Proc.* **1979**, *C7902131*, 95–99.

[9] R. N. Mohapatra, G. Senjanovic, *Phys. Rev. Lett.* **1980**, *44*, 912.

[10] D. R. Nygren, *Journal of Physics: Conference Series* **2015**, *650*, 012002.

[11] B. J. P. Jones, A. D. McDonald, D. R. Nygren, *JINST* **2016**, *11*, P12011.

[12] A. D. McDonald et al., *Phys. Rev. Lett.* **2018**, *120*, 132504.

[13] P. Thapa et al., *Scientific Reports* **2019**, *9*, Number: 1 Publisher: Nature Publishing Group, 15097.

[14] P. Thapa et al., *ACS Sensors* **2021**, *6*, Publisher: American Chemical Society, 192–202.

[15] B. J. P. Jones, A. D. McDonald, D. R. Nygren, *Journal of Instrumentation* **2016**, *11*, Publisher: IOP Publishing, P12011–P12011.

[16] NEXT Collaboration et al., *Physical Review Letters* **2018**, *120*, Publisher: American Physical Society, 132504.

[17] S. Davidson, E. Nardi, Y. Nir, *Physics Reports* **2008**, *466*, 105–177.

[18] K. A. Olive, *Chinese Physics C* **2014**, *38*, Publisher: IOP Publishing, 090001.

[19] Super-Kamiokande Collaboration et al., *Physical Review Letters* **1998**, *81*, Publisher: American Physical Society, 1562–1567.

[20] B. T. Cleveland et al., *The Astrophysical Journal* **1998**, *496*, Publisher: IOP Publishing, 505.

[21] SNO Collaboration et al., *Physical Review Letters* **2002**, *89*, Publisher: American Physical Society, 011301.

[22] KamLAND-Zen Collaboration et al., *Physical Review Letters* **2019**, *122*, Publisher: American Physical Society, 192501.

[23] M. H. Ahn et al., *Physical Review Letters* **2003**, *90*, Publisher: American Physical Society, 041801.

[24] MINOS Collaboration et al., *Physical Review Letters* **2006**, *97*, Publisher: American Physical Society, 191801.

[25] L. Gastaldo et al., *The European Physical Journal Special Topics* **2017**, *226*, 1623–1694.

[26] A. Nucciotti et al., *Journal of Low Temperature Physics* **2018**, *193*, 1137–1145.

[27] M. P. Croce et al., *Journal of Low Temperature Physics* **2016**, *184*, 958–968.

[28] J. Lesgourgues, S. Pastor, *Physics Reports* **2006**, *429*, 307–379.

[29] N. Aghanim et al., *Astronomy & Astrophysics* **2020**, *641*, Publisher: EDP Sciences, A6.

[30] P. Hernandez, Neutrino physics, arXiv:1010.4131 [hep-ph], **2010**.

[31] M. C. Gonzalez-Garcia, M. Maltoni, *Physics Reports* **2008**, *460*, 1–129.

[32] R. N. Mohapatra, G. Senjanović, *Physical Review Letters* **1980**, *44*, Publisher: American Physical Society, 912–915.

[33] R. N. Mohapatra, G. Senjanović, *Physical Review D* **1981**, *23*, Publisher: American Physical Society, 165–180.

[34] J. Schechter, J. W. F. Valle, *Physical Review D* **1980**, *22*, Publisher: American Physical Society, 2227–2235.

[35] M. Goeppert-Mayer, *Physical Review* **1935**, *48*, Publisher: American Physical Society, 512–516.

[36] M. G. Inghram, J. H. Reynolds, *Physical Review* **1950**, *78*, Publisher: American Physical Society, 822–823.

[37] S. R. Elliott, A. A. Hahn, M. K. Moe, *Physical Review Letters* **1987**, *59*, Publisher: American Physical Society, 2020–2023.

[38] A. S. Barabash, *Physics of Atomic Nuclei* **2011**, *74*, 603–613.

[39] J. J. Gomez-Cadenas et al., *La Rivista del Nuovo Cimento* **2012**, *35*, 29–98.

[40] M. J. Dolinski, A. W. Poon, W. Rodejohann, *Annual Review of Nuclear and Particle Science* **2019**, *69*, _eprint: https://doi.org/10.1146/annurev-nucl-101918-023407, 219–251.

[41] W. H. Furry, *Physical Review* **1939**, *56*, Publisher: American Physical Society, 1184–1193.

[42] M. Doi, T. Kotani, E. Takasugi, *Progress of Theoretical Physics Supplement* **1985**, *83*, 1–175.

[43] A. Bettini, *The European Physical Journal Plus* **2012**, *127*, 112.

[44] EXO Collaboration et al., *Physical Review C* **2014**, *89*, Publisher: American Physical Society, 015502.

[45] KamLAND-Zen Collaboration et al., *Physical Review C* **2012**, *85*, Publisher: American Physical Society, 045504.

[46] D. Nygren, *Nuclear Instruments and Methods in Physics Research Section A: Accelerators Spectrometers Detectors and Associated Equipment* **2009**, *603*, 337–348.

[47] NEXT Collaboration et al., *Physical Review C* **2022**, *105*, Publisher: American Physical Society, 055501.

[48] V. Álvarez et al., *Journal of Instrumentation* **2013**, *8*, Publisher: IOP Publishing, T01002–T01002.

[49] S. Cebrián et al., *Journal of Instrumentation* **2015**, *10*, Publisher: IOP Publishing, P05006–P05006.

[50] S. Cebrián et al., *Journal of Instrumentation* **2017**, *12*, Publisher: IOP Publishing, T08003–T08003.

[51] J. Muñoz Vidal, Accepted: 2018-06-11T07:28:49Z, PhD thesis, **2018**.

[52] D. R. Nygren, *Journal of Physics: Conference Series* **2015**, *650*, Publisher: IOP Publishing, 012002.

[53] K. Woodruff et al., *Journal of Instrumentation* **2020**, *15*, Publisher: IOP Publishing, P04022–P04022.

[54] E. Bainglass et al., *Physical Review A* **2018**, *97*, Publisher: American Physical Society, 062509.

[55] A. H. Snell, F. Pleasonton, *Physical Review* **1957**, *107*, Publisher: American Physical Society, 740–745.

[56] EXO-200 Collaboration et al., *Physical Review C* **2015**, *92*, Publisher: American Physical Society, 045504.

[57] M. K. Moe, *Physical Review C* **1991**, *44*, Publisher: American Physical Society, R931–R934.

[58] M. Danilov et al., *Physics Letters B* **2000**, *480*, 12–18.

[59] P. Novella et al., *Journal of High Energy Physics* **2018**, *2018*, 112.

[60] D. Sinclair et al., *Journal of Physics: Conference Series* **2011**, *309*, Publisher: IOP Publishing, 012005.

[61] B. Mong et al., *Physical Review A* **2015**, *91*, arXiv:1410.2624 [hep-ex, physics:nucl-ex, physics:physics], 022505.

[62] K. Twelker et al., *Review of Scientific Instruments* **2014**, *85*, Publisher: American Institute of Physics, 095114.

[63] C. Chambers et al., Imaging individual barium atoms in solid xenon for barium tagging in nEXO, arXiv:1806.10694 [nucl-ex, physics:physics], **2018**.

[64] S. L. Reck-Peterson, N. D. Derr, N. Stuurman, *Cold Spring Harbor Protocols* **2010**, *2010*, pdb.top73.

[65] A. Mcdonald, Accepted: 2022-01-20T18:09:24Z, Thesis, **2020**.

[66] M. E. Huston, K. W. Haider, A. W. Czarnik, *Journal of the American Chemical Society* **1988**, *110*, Publisher: American Chemical Society, 4460–4462.

[67] B. Valeur, N. Nuno Berberan-Santos, *Molecular Fluorescence: Principles and Applications*, Section: 14 _eprint: https://onlinelibrary.wiley.com/do John Wiley & Sons, Ltd, **2012**.

[68] A. I. Aranburu Leiva, PhD thesis, **2023**.

[69] B. Aparicio Gil, *University of the Basque Country* **2022**, DOI 10/58621.

[70] M. Aginagalde et al., *The Journal of Organic Chemistry* **2010**, *75*, 2776–2784.

[71] Y. Zhang et al., *Chemical Communications* **2018**, *54*, Publisher: The Royal Society of Chemistry, 8799–8809.

[72] C.-C. Ko, V. W.-W. Yam, *Accounts of Chemical Research* **2018**, *51*, Publisher: American Chemical Society, 149–159.

[73] R. Maitra et al., *European Journal of Organic Chemistry* **2017**, *2017*, _eprint: https://onlinelibrary.wiley.com/doi/pdf/10.1002/ejoc.201701109, 5975–5985.

[74] D. A. Dougherty, *Accounts of Chemical Research* **2013**, *46*, Publisher: American Chemical Society, 885–893.

[75] I. Rivilla et al., *Nature* **2020**, *583*, Number: 7814 Publisher: Nature Publishing Group, 48–54.

[76] S. S. Batsanov, *Inorganic Materials* **2001**, *37*, 871–885.

[77] Z. Feng et al., *Nanoscale* **2018**, *10*, Publisher: The Royal Society of Chemistry, 2067–2072.

[78] L. S. Shlyakhtenko, A. A. Gall, Y. L. Lyubchenko in *Cell Imaging Techniques: Methods and Protocols*, (Eds.: D. J. Taatjes, J. Roth), Methods in Molecular Biology, Humana Press, Totowa, NJ, **2013**, pp. 295–312.

[79] M. Hijazi et al., *Journal of Materials Science* **2018**, *53*, 727–738.

[80] J. Enderlein, *Biophysical Journal* **2000**, *78*, 2151–2158.

[81] R. J. Moerland, J. P. Hoogenboom, *Optica* **2016**, *3*, Publisher: Optical Society of America, 112–117.

[82] P. Vacca et al., *The Journal of Physical Chemistry C* **2007**, *111*, Publisher: American Chemical Society, 17404–17408.

[83] M. G. Mason et al., *Journal of Applied Physics* **1999**, *86*, Publisher: American Institute of Physics, 1688–1692.

[84] S. Habuchi et al., *Proceedings of the National Academy of Sciences* **2005**, *102*, Publisher: Proceedings of the National Academy of Sciences, 9511–9516.

[85] D. Thomas et al., *Cell Calcium* **2000**, *28*, 213–223.

[86] H. Lüth, *Solid Surfaces, Interfaces and Thin Films*, Springer International Publishing, Cham, **2015**.

[87] J. M. Sobrado, J. A. Martín-Gago, *Journal of Applied Physics* **2016**, *120*, Publisher: American Institute of Physics, 145307.

[88] B. Crystal, Bihur-Crystal-ALI-System-Datasheet-v2.3.pdf.

[89] J. M. Sobrado Vallecillo, Accepted: 2014-11-05T14:20:40Z, doctoralThesis, **2014**.

[90] P. Hannifin, Ideal Vacuum | Replacement Main Load Spring for High-Speed Pulsed Solenoid Valves, Pack of 5.

[91] V. A. Versteeg, C. T. Avedisian, R. Raj, *Journal of the American Ceramic Society* **1995**, *78*, _eprint: https://onlinelibrary.wiley.com/doi/pdf/10.11 2916.1995.tb08052.x, 2763–2768.

[92] C. Zhu, A. Osherov, M. J. Panzer, *Electrochimica Acta* **2013**, *111*, 771–778.

[93] J. Holec et al., *Angewandte Chemie International Edition* **2021**, *60*, 7752–7758.

[94] F. J. Ávila et al., *Scientific Reports* **2019**, *9*, Number: 1 Publisher: Nature Publishing Group, 10121.

[95] J. P. Zinter, M. J. Levene, *Optics Express* **2011**, *19*, Publisher: Optica Publishing Group, 15348–15362.

[96] W. Denk, J. H. Strickler, W. W. Webb, *Science* **1990**, *248*, Publisher: American Association for the Advancement of Science, 73–76.

[97] C. J. Powell, *Journal of Vacuum Science & Technology A: Vacuum Surfaces and Films* **2020**, *38*, Publisher: American Vacuum SocietyAVS, 023209.

[98] M. Stredansky et al., *Nanoscale Advances* **2019**, *1*, Publisher: RSC, 1721–1725.

[99] L. Gross, *Nature Chemistry* **2011**, *3*, 273–278.

[100] L. Gross et al., *Angewandte Chemie International Edition* **2018**, *57*, 3888–3908.

[101] N. Moll et al., *New Journal of Physics* **2010**, *12*, Publisher: IOP Publishing, 125020.

[102] P. Hapala et al., *Physical Review B* **2014**, *90*, Publisher: American Physical Society, 085421.

[103] Barium Spectra – BaF2, en-US, **2022**.

[104] J. H. Scofield, *Journal of Electron Spectroscopy and Related Phenomena* **1976**, *8*, 129–137.

[105] Non-Linear Least-Squares Minimization and Curve-Fitting for Python — Non-Linear Least-Squares Minimization and Curve-Fitting for Python.

[106] I. F. Uchegbu, S. P. Vyas, *International Journal of Pharmaceutics* **1998**, *172*, 33–70.

[107] J.-P. Malval et al., *Journal of the American Chemical Society* **2002**, *124*, Publisher: American Chemical Society, 904–905.

[108] R. M. Uda et al., *Journal of inclusion phenomena and macrocyclic chemistry* **2005**, *51*, 111–117.

[109] M. Dobler, *Ionophores and Their Structures*, John Wiley, **1981**.

[110] G. W. Gokel, *Crown Ethers and Cryptands*, **1991**.

[111] M. B. More, D. Ray, P. B. Armentrout, *Journal of the American Chemical Society* **1999**, *121*, Publisher: American Chemical Society, 417–423.

[112] S. Maleknia, J. Brodbelt, Cavity-size-dependent dissociation of crown ether/ammonium ion complexes in the gas phase, EN, Archive Location: world Publisher: American Chemical Society, **2002**.

[113] S. Yoshimoto et al., *Chemical Communications* **2003**, Publisher: The Royal Society of Chemistry, 2174–2175.

[114] S. Flink, F. C. J. M. van Veggel, D. N. Reinhoudt, *The Journal of Physical Chemistry B* **1999**, *103*, Publisher: American Chemical Society, 6515–6520.

[115] Y. Inokuchi et al., *New Journal of Chemistry* **2015**, *39*, Publisher: The Royal Society of Chemistry, 8673–8680.

[116] A. Yubero Navarro, PhD thesis, **2023**.

[117] P. Herrero-Gómez et al., *Nature Communications* **2022**, *13*, Number: 1 Publisher: Nature Publishing Group, 7741.

[118] J. Dai et al., *ChemPhysChem* **2019**, *20*, _eprint: https://onlinelibrary.wiley.com/c 2367–2375.

[119] T. Heinrich et al., *RSC Advances* **2014**, *4*, Publisher: The Royal Society of Chemistry, 17694–17702.

[120] Y. Zubavichus et al., *The Journal of Physical Chemistry B* **2008**, *112*, Publisher: American Chemical Society, 13711–13716.

[121] D. N. Kelly et al., *The Journal of Chemical Physics* **2010**, *133*, Publisher: American Institute of Physics, 101103.

[122] K. C. Prince et al., *The Journal of Physical Chemistry A* **2003**, *107*, Publisher: American Chemical Society, 1955–1963.

[123] M. Keil et al., *Applied Surface Science* **1998**, *125*, 273–286.

[124] P. Fortmeier et al., *Liquid Crystals* **1999**, *26*, Publisher: Taylor & Francis _eprint: https://doi.org/10.1080/02678292.1999.11509455, 1713–1716.

[125] M. Pedio et al., *Physical Review B* **2002**, *66*, Publisher: American Physical Society, 144109.

[126] J. Holburg et al., *Analytical Chemistry* **2022**, *94*, Publisher: American Chemical Society, 3510–3516.

[127] D. J. Menzies et al., *Langmuir* **2010**, *26*, Publisher: American Chemical Society, 13987–13994.

[128] L. Novotny, B. Hecht, *Principles of Nano-Optics*, 2nd ed., Cambridge University Press, Cambridge, **2012**.

[129] A. Perez Romera, PhD thesis, **2023**.

[130] M. Fikry et al., *Optical and Quantum Electronics* **2021**, *53*, 122.

[131] VASP - Vienna Ab initio Simulation Package.

[132] A. D. McDonald et al., *Physical Review Letters* **2018**, *120*, arXiv: 1711.04782, 132504.

[133] S.-H. Lee, *Optics Express* **2018**, *26*, Publisher: Optica Publishing Group, 8049–8058.

[134] N. Granzow in Photonics and Education in Measurement Science 2019, *Vol. 11144*, SPIE, **2019**, pp. 34–38.

[135] X. Zhou et al., *Advances in Condensed Matter Physics* **2014**, *2014*, Publisher: Hindawi, e853764.

[136] A. G. Shard, *Journal of Vacuum Science & Technology A* **2020**, *38*, Publisher: American Vacuum Society, 041201.

[137] N. H. Turner, J. A. Schreifels, Surface Analysis: X-ray Photoelectron Spectroscopy and Auger Electron Spectroscopy, EN, research-article, Archive Location: world Publisher: American Chemical Society, **2002**.

[138] B. D. Ratner, D. G. Castner in *Surface Analysis – The Principal Techniques*, Section: 3 _eprint: https://onlinelibrary.wiley.com/doi/pdf/10.1002/9 John Wiley & Sons, Ltd, **2009**, pp. 47–112.

[139] F. Muller, AG Jacobs, Available online at: https://jacobs.physik.uni-saarland.de/home/index.php?page=steinbeiss/home_cms_steinbeissdet3-0&navi=service, last accessed on 2022-10-08 15:43:34.

[140] H. Shinotsuka et al., *Surface and Interface Analysis* **2015**, *47*, _eprint: https://onlinelibrary.wiley.com/doi/pdf/10.1002/sia.5789, 871–888.

[141] C. D. Wagner et al., *Surface and Interface Analysis* **1981**, *3*, _eprint: https://onlinelibrary.wiley.com/doi/pdf/10.1002/sia.740030506, 211–225.

[142] F. Trixler, *Current Organic Chemistry*, *17*, 1758–1770.

[143] Nanoscience on the tip - a one week hands-on SPM workshop, Available online at: https://depts.washington.edu/nanolab/NUE_UNIQUE/Ba last accessed on 2022-10-12 18:40:29.

[144] G. Hähner, *Chemical Society Reviews* **2006**, *35*, Publisher: The Royal Society of Chemistry, 1244–1255.

[145] S. D. Senanayake et al., *The Journal of Physical Chemistry C* **2009**, *113*, Publisher: American Chemical Society, 6208–6214.

[146] P. Willmott in *An Introduction to Synchrotron Radiation*, John Wiley & Sons, Ltd, **2011**, p. 5.

[147] J. M. Bueno et al., *Investigative Ophthalmology & Visual Science* **2011**, *52*, 5325–5331.

[148] Edinburgh Instruments, Photoluminescence Spectrometer FLS 1000 | Spectroscopy Instruments, en-GB.

List of Publications

During this thesis the following articles were published related to the content of the research: .

[1] P. Herrero-Gómez et al., *Nature Communications* **2022**, *13*, Number: 1 Publisher: Nature Publishing Group, 7741.

[2] I. Rivilla et al., *Nature* **2020**, *583*, Number: 7814 Publisher: Nature Publishing Group, 48–54.

[3] J. Holec et al., *Angewandte Chemie International Edition* **2021**, *60*, _eprint: https://onlinelibrary.wiley.com/doi/pdf/10.1002/anie.202016163, 7752–7758.

The following articles based on results presented in this thesis are in preparation:

[1] P. Herrero-Gómez, C. Rogero, L. Schio, **2023**, Paper in preparation.

[2] P. Herrero-Gómez, C. Rogero, **2023**, Paper in preparation.

This article was based on my MSc research and was also published during my PhD Thesis.

[1] S. Bruenner et al., *The European Physical Journal C* **2021**, *81*, 343.

Lastly, as a member of the NEXT collaboration, the following works were published:

[1] NEXT Collaboration et al., *Physical Review C* **2022**, *105*, Publisher: American Physical Society, 055501.

[2] A. Simón et al., *Journal of High Energy Physics* **2021**, *2021*, 146.

[3] G. Martínez-Lema et al., *Journal of High Energy Physics* **2021**, *2021*, 203.

[4] M. Kekic et al., *Journal of High Energy Physics* **2021**, *2021*, 189.

[5] C. Adams et al., *Journal of High Energy Physics* **2021**, *2021*, 164.

[6] L. Rogers et al., *Journal of Physics G: Nuclear and Particle Physics* **2020**, *47*, Publisher: IOP Publishing, 075001.

[7] A. F. M. Fernandes et al., *Journal of High Energy Physics* **2020**, *2020*, 34.

[8] P. Ferrario et al., *Journal of High Energy Physics* **2019**, *2019*, 52.

[9] J. Renner et al., *Journal of High Energy Physics* **2019**, *2019*, 230.

[10] P. Novella et al., *Journal of High Energy Physics* **2019**, *2019*, 51.

[11] A. D. McDonald et al., *Journal of Instrumentation* **2019**, *14*, Publisher: IOP Publishing, P08009–P08009.

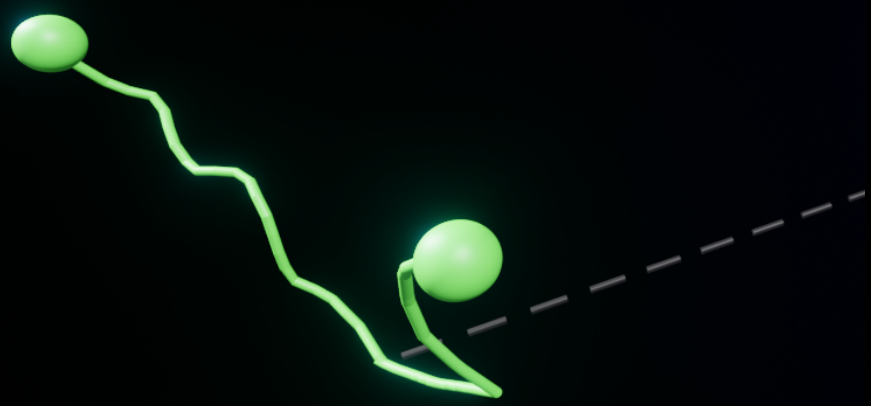

European Research Council
Established by the European Commission